THIRD-ORDER NONLINEAR OPTICAL PROPERTIES OF POLYMETHINE-BASED MATERIALS: A THEORETICAL INVESTIGATION

A Dissertation
Presented to
The Academic Faculty

by

Rebecca Lynn Gieseking

In Partial Fulfillment
of the Requirements for the Degree
Doctor of Philosophy in the
School of Chemistry and Biochemistry

Georgia Institute of Technology
May 2015

THIRD-ORDER NONLINEAR OPTICAL PROPERTIES OF POLYMETHINE-BASED MATERIALS: A THEORETICAL INVESTIGATION

Approved by:

Professor C. David Sherrill, Advisor
School of Chemistry and Biochemistry
Georgia Institute of Technology

Professor Joseph W. Perry
School of Chemistry and Biochemistry
Georgia Institute of Technology

Professor Jean-Luc Brédas
School of Chemistry and Biochemistry
Georgia Institute of Technology

Professor Bernard Kippelen
School of Electrical and Computer Engineering
Georgia Institute of Technology

Professor Seth R. Marder
School of Chemistry and Biochemistry
Georgia Institute of Technology

Date Approved: April 6, 2015

ACKNOWLEDGEMENTS

First and foremost, I would like to express my gratitude to my advisor, Professor Jean-Luc Brédas, for providing me with the opportunity to study in his group. I am grateful for his guidance and scientific insight in my research and the flexibility to explore the aspects of my research that I found most interesting, which helped me learn a great deal of independence and made my research more enjoyable. I appreciate his constructive criticism and focus on clear communication, which have also aided in my scientific development.

I would also like to thank my committee members. I am particularly grateful to Professor Seth Marder for many insightful discussions and for his encouragement to achieve my full potential. I would also like to express my gratitude to Professor Joseph Perry for his helpful guidance, advice, and expertise. In addition, I would like to thank Professors C. David Sherrill and Bernard Kippelen for their support and guidance. I am also greatly indebted to many experimental collaborators: Dr. Steve Barlow, Dr. Tim Parker, Dr. Yulia Getmanenko, Dr. Iryna Davydenko, Dr. Joel Hales, Anselmo Kim, Professor Eric Van Stryland, Professor David Hagan, and Trenton Ensley.

My sincere gratitude also goes to the many members of the Brédas group, the Brédators, who have provided assistance and support during the past five years and fostered a productive work environment. In particular, I would like to thank Dr. Chad Risko for many insightful discussions and much helpful feedback on my writing, Dr. Sukrit

Mukhopadhyay for much assistance and numerous fruitful conversations about research, and Dr. Veaceslav Coropceanu for sharing his knowledge with me. I am also grateful to Stephen Shiring and Dr. Mahesh Kumar for their openness to exploring new ideas and for asking thoughtful questions that probed my scientific understanding.

Finally, I would like to thank my family, particularly my parents, for their love and encouragement and for instilling in me a love of science and learning at a very young age that started me on a path toward research. I would also like to thank my friends, who have encouraged me and helped me maintain motivation throughout graduate school.

TABLE OF CONTENTS

LIST OF TABLES

LIST OF FIGURES

LIST OF ABBREVIATIONS

ACN	Acetonitrile
AOS	All-optical switch(ing)
BLA	Bond length alternation
BOA	Bond order alternation
CC	Coupled cluster
CC2	Second-order approximate coupled-cluster
CI	Configuration interaction
DCM	Dichloromethane
DFT	Density Functional Theory
DMSO	Dimethyl sulfoxide
FOM	Figure-of-merit
GGA	Generalized gradient approach
HF	Hartree-Fock
HOMO	Highest occupied molecular orbital
Im	Imaginary
IR	Infrared
INDO	Intermediate Neglect of Differential Overlap
LDA	Local density approximation
LUMO	Lowest unoccupied molecular orbital
LRC	Long-range corrected
MD	Molecular dynamics
MM	Molecular mechanics

MO	Molecular orbital
MRDCI	Multi-reference determinant configuration interaction
NBO	Natural bond order
NLO	Nonlinear optics/optical
OPA	One-photon absorption
Re	Real
SCF	Self-consistent field
SCI	Singles configuration interaction
SDCI	Singles and doubles configuration interaction
SIE	Self-interaction error
SOS	Sum-over-states
TPA	Two-photon absorption
ZDO	Zero Differential Overlap

SUMMARY

Organic π-conjugated molecules and materials with large real parts and small imaginary parts of the third-order polarizability are of great interest for all-optical switching applications. In this dissertation, we use quantum-chemical and molecular-dynamics approaches to investigate the structure-property relationships that influence the nonlinear optical properties of π-conjugated molecules and materials. We begin with an overview of nonlinear optics, focusing in particular on the electronic properties of linear π-conjugated systems and some of the important problems that have limited device applications of these molecules to date. This is followed by a brief review of the computational methods employed in these studies.

We then turn to the main results of the dissertation. Chapter 3 describes the structural dependence of the transition dipole moment between the first two polymethine and polyene excited states. Chapter 4 discusses the relationship between BLA, which depends on the polymethine geometric structure, and BOA, which probes the polymethine electronic structure. Chapter 5 describes the benchmarking of computational methods to describe the symmetry-breaking of long polymethines and preliminary evidence regarding the role of vibrational modes in symmetry-breaking. Chapter 6 explains the negative third-order polarizability of tetraphenylphosphate and analogous systems. Chapter 7 focuses on molecular-dynamics studies of polymethine bulk aggregation, particularly the relationships between chemical structure and the geometric and electronic structures of the resulting aggregates. Finally, Chapter 8 provides a synopsis of the work and discussion of further directions.

CHAPTER 1

INTRODUCTION

The demand for long-distance data transmission, used in tele- and video-communications, music and video streaming, and internet usage on an ever-increasing variety of devices, is growing dramatically. The amount of data transmitted through the Internet is currently increasing by more than 20% each year, and total annual data transmission is expected to surpass one zetabyte (1×10^{21} bytes) in 2016.[1] Currently, most data transmission occurs via silica fibers, which enable optical signals at wavelengths around 1300 and 1550 nm (0.95 and 0.80 eV) to propagate with minimal attenuation and dispersion.[2,3] To meet the increasing demand, data processing at rates larger than 1 terabit/s will be required,[4] an order-of-magnitude faster than current opto-electrical switching rates.[5] To achieve such large switching rates, it is necessary to perform the switching through an all-optical switching (AOS) process, in which one optical beam is used to modulate a second optical beam without the use of an electrical signal.[6-8]

In a simple AOS device (Figure 1.1) based on a Mach-Zehnder interferometer, an incoming optical signal is divided equally between the two arms of the device; in each arm, the light interacts with a nonlinear optical (NLO) material over identical path lengths. In the absence of an external perturbing (control) pulse, the two beams pass through the NLO material and recombine at the end of the device with constructive interference, which yields an output signal similar to the incoming signal. However, when one arm is subjected to a high-intensity control pulse, the refractive index of the

NLO material is modified, which alters the speed at which the signal propagates in that arm. If the difference in speed and other device parameters are tuned to produce a phase difference of π between the two arms, the two beams will interact destructively and the output signal will be close to zero.

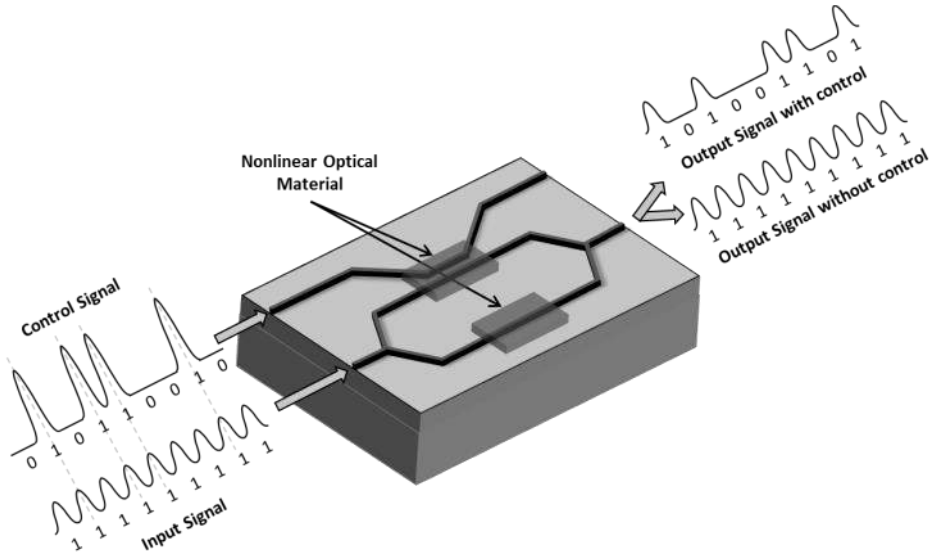

Figure 1.1. Illustration of all-optical switching (AOS) using a Mach-Zehnder configuration and a nonlinear (NLO) optical material.[9,10]

To achieve the necessary phase shift in devices, the magnitude of the change in the refractive index must be as large as possible; this requires a very large real component of the material third-order electric susceptibility ($\mathrm{Re}(\chi^{(3)})$). At the same frequency of light, losses due to one-photon absorption (OPA) and two-photon absorption (TPA) must be very small; minimizing TPA requires a very small imaginary component of the third-order electric susceptibility ($\mathrm{Im}(\chi^{(3)})$).[11-13] For a device to be functional, the figure-of-merit (FOM), defined as $|\mathrm{Re}(\chi^{(3)})/\mathrm{Im}(\chi^{(3)})|$, must be $>> 4\pi$.[14-16]

Organic π-conjugated molecules and polymers often have very large third-order polarizabilities, but most have very small FOMs due to large TPA cross-sections at energies close to that of the first excited state.[15,17] As will be detailed below, polymethine-based materials are uniquely suited to achieve the necessary large $\mathrm{Re}(\chi^{(3)})$ and FOM for AOS applications. Although rigorously speaking, polymethines are molecules that have a backbone consisting of several methine (*i.e.*, sp^2-hybridized CH) groups, we use the term 'polymethine dye' to refer more specifically to molecules such as cyanines that have an odd number of methine groups and are positively or negatively charged (a feature that preserves a closed-shell electronic structure).

Here, we begin by defining the derivative relationships between molecular polarizability and energy. This is followed by a description of simplified sum-over-states (SOS) expressions for the molecular polarizabilities that provide a link among the primary electronic states involved in NLO response. We then show how simple electronic-structure approaches in combination with the SOS expressions can be used to make the connection between molecular architecture and these electronic states. We end this chapter with an overview of this thesis.

1.1. Energy and Molecular Polarizability

The NLO properties that are critical for AOS applications can be understood in terms of the interaction of the material with the electric field of light. An external electric field $\vec{F}(\omega)$ applied to a medium induces a polarization $\vec{P}^{ind}(\omega)$, such that the total material polarization $\vec{P}$ can be written (using the electric-dipole approximation) as

$$\vec{P} = \vec{P}_0 + \vec{P}^{ind}(\omega) \tag{1.1}$$

where $\vec{P}_0$ is the permanent medium polarization in the absence of an electric field and ω is the frequency of the electric field. $\vec{P}^{ind}(\omega)$ can be written using a Taylor expansion as

$$\vec{P}_{\mathrm{I}}^{ind}(\omega) = \frac{1}{1!}\chi_{\mathrm{IJ}}^{(1)}(\omega)\cdot\vec{F}_{\mathrm{J}}(\omega) + \frac{1}{2!}\chi_{\mathrm{IJK}}^{(2)}(\omega)\cdot\vec{F}_{\mathrm{J}}(\omega)\cdot\vec{F}_{\mathrm{K}}(\omega) \tag{1.2}$$

$$+\frac{1}{3!}\chi_{\mathrm{IJKL}}^{(3)}(\omega)\vec{F}_{\mathrm{J}}(\omega)\cdot\vec{F}_{\mathrm{K}}(\omega)\cdot\vec{F}_{\mathrm{L}}(\omega) + \cdots$$

where the subscripts I, J, K, L denote the laboratory fixed axes (X, Y, or Z); $\chi^{(n)}$ represents the n^{th}-order electrical susceptibilities of the material; and $\vec{F}_{\mathrm{J}}(\omega)$ is the J^{th} component of the electric field. We note that $\chi^{(n)}$ is a tensor of rank (n+1): e.g., the third-order electrical susceptibility $\chi^{(3)}$ is a fourth-rank tensor with 81 components.

Designing molecular materials with large polarizabilities requires understanding polarization not only on the macroscopic scale but also on the molecular scale. Since we are focused on the response on time scales on the order of visible or near-IR frequencies (10^{14} – 10^{15} s^{-1}), only the electronic response of the molecules is in general sufficiently fast to contribute significantly to the material polarizability. Analogously to the bulk polarization, the molecular dipole moment can be modified by an external electric field. The total dipole moment for a molecule interacting with an electric field $\vec{F}(\omega)$ is expressed as

$$\vec{\mu} = \vec{\mu}_0 + \vec{\mu}^{ind}(\omega) \tag{1.3}$$

where $\vec{\mu}_0$ denotes the permanent molecular dipole moment (defined here as the ground-state dipole moment $\vec{\mu}_{\mathrm{g}}$) and the induced dipole moment $\vec{\mu}^{ind}$ is expressed using a Taylor series expansion as

$$\vec{\mu}_{\mathrm{i}}^{ind}(\omega) = \frac{1}{1!}\alpha_{\mathrm{ij}}(\omega)\cdot\vec{F}_{\mathrm{j}}(\omega) + \frac{1}{2!}\beta_{\mathrm{ijk}}\cdot\vec{F}_{\mathrm{j}}(\omega)\cdot\vec{F}_{\mathrm{k}}(\omega) \qquad 1.4$$

$$+\frac{1}{3!}\gamma_{\mathrm{ijkl}}\cdot\vec{F}_{\mathrm{j}}(\omega)\cdot\vec{F}_{\mathrm{k}}(\omega)\cdot\vec{F}_{\mathrm{l}}(\omega)+\cdots$$

where the (lower-case) subscripts i, j, k, and l denote the molecular fixed axes (x, y, or z); α_{ij}, β_{ijk}, and γ_{ijkl} are the first-order (linear), second-order, and third-order polarizabilities, respectively; and $\vec{F}_{\mathrm{j}}(\omega)$ is the j^{th} component of the electric field.

When the molecule interacts with an external electric field, the total energy of the system evolves according to the Stark effect, with the resulting Stark energy E_{s} defined as

$$E_{\mathrm{s}} = E_{\mathrm{s}}^{0} - \vec{\mu}\cdot\vec{F}(\omega) \qquad 1.5$$

where $\vec{\mu}$ can be expanded using the expressions in Equations 1.3 and 1.4 as

$$E_{\mathrm{s}} = E_{\mathrm{s}}^{0} - \vec{\mu}_{0}\cdot\vec{F}_{\mathrm{i}}(\omega) - \frac{1}{2!}\alpha_{\mathrm{ij}}(\omega)\cdot\vec{F}_{\mathrm{i}}(\omega)\cdot\vec{F}_{\mathrm{j}}(\omega) \qquad 1.6$$

$$-\frac{1}{3!}\beta_{\mathrm{ijk}}\cdot\vec{F}_{\mathrm{i}}(\omega)\cdot\vec{F}_{\mathrm{j}}(\omega)\cdot\vec{F}_{\mathrm{k}}(\omega)$$

$$-\frac{1}{4!}\gamma_{\mathrm{ijkl}}\cdot\vec{F}_{\mathrm{i}}(\omega)\cdot\vec{F}_{\mathrm{j}}(\omega)\cdot\vec{F}_{\mathrm{k}}(\omega)\cdot\vec{F}_{\mathrm{l}}(\omega)+\cdots$$

and E_{s}^{0} is the energy of the unperturbed (isolated) molecular system.

These equations show that there is a direct relationship between the polarizabilities and the total energy of a quantum-mechanical system. According to the generalized Hellman-Feynman theorem, the derivative of the total energy with respect to some parameter (here, the applied electric field) is related to the expectation (average) value of the derivative of the Hamiltonian with respect to the same parameter, which can be written as

$$\frac{\partial E_{\mathrm{g}}}{\partial \vec{F}(\omega)} = \left\langle \psi_{\mathrm{g}} \middle| \frac{\partial \hat{H}}{\partial \vec{F}(\omega)} \middle| \psi_{\mathrm{g}} \right\rangle \tag{1.7}$$

where $\hat{H}$ is the Hamiltonian for the entire system. At the limit of static polarizabilities ($\omega = 0$), these equations allow us to define a series of derivative relationships between the total system energy and molecular polarizabilities:

$$-\left(\frac{\partial E_{\mathrm{g}}}{\partial \vec{F}(0)}\right)_{\vec{F}(0)\to 0} = \vec{\mu}_0 \tag{1.8}$$

$$-\left(\frac{\partial^2 E_{\mathrm{g}}}{\partial \vec{F}(0)^2}\right)_{\vec{F}(0)\to 0} = \left(\frac{\partial \vec{\mu}}{\partial \vec{F}(0)}\right)_{\vec{F}(0)\to 0} = \alpha(0) \tag{1.9}$$

$$-\left(\frac{\partial^3 E_{\mathrm{g}}}{\partial \vec{F}(0)^3}\right)_{\vec{F}(0)\to 0} = \left(\frac{\partial^2 \vec{\mu}}{\partial \vec{F}(0)^2}\right)_{\vec{F}(0)\to 0} = \beta(0) \tag{1.10}$$

$$-\left(\frac{\partial^4 E_{\mathrm{g}}}{\partial \vec{F}(0)^4}\right)_{\vec{F}(0)\to 0} = \left(\frac{\partial^3 \vec{\mu}}{\partial \vec{F}(\omega)^4}\right)_{\vec{F}(0)\to 0} = \gamma(0) \tag{1.11}$$

As we will see, these derivative relationships make it possible to understand relationships between polarization and molecular structure by examining the bond length alternation or bond order alternation in conjugated molecules.

1.2. Sum-over-states (SOS) expressions for molecular polarizabilities

From a theoretical perspective, molecular polarizabilities can be evaluated in a number of ways. Here, we focus on the sum-over-states (SOS) approach,[18] which provides practical insight into the relationships between molecular structure and NLO response. The SOS expressions allow for understanding of the molecular NLO properties in terms of the

ground-state and lowest several excited-state energies, the transition dipole moments among these states, and (in non-centrosymmetric molecules) the state dipole moments.

The SOS expressions are derived from from the perturbation theory expression of the Stark energy. The Stark energy terms at different orders (Equation 1.6) can be directly related to the optical nonlinearities based on their order in the field strength, *i.e.*, the SOS expression for the molecular polarizability at order (n - 1) is the n^{th}-order perturbation theory expression in the electric field. A first-order perturbation in the electric field relates to the zero-order polarizability in the SOS expression, *i.e.*, the ground-state dipole moment. We note that the first-order perturbation term is energetically stabilizing only if the electric field is oriented parallel to the dipole moment vector.

The second- through fourth-order perturbations, α_{ij}, β_{ijk}, and γ_{ijkl}, are expressed as:

$$\alpha_{\text{ij}}(\omega = \omega_{\text{p}}) = \sum_{w \neq g} \frac{\langle \psi_{\text{g}} | \hat{\mu}^{\text{i}} | \psi_{\text{w}} \rangle \langle \psi_{\text{w}} | \hat{\mu}^{\text{j}} | \psi_{\text{g}} \rangle}{E_{\text{gw}} - i\Gamma_{\text{gw}} - \hbar\omega_{\text{p}}} + \frac{\langle \psi_{\text{g}} | \hat{\mu}^{\text{j}} | \psi_{\text{w}} \rangle \langle \psi_{\text{w}} | \hat{\mu}^{\text{i}} | \psi_{\text{g}} \rangle}{E_{\text{gw}} - i\Gamma_{\text{gw}} + \hbar\omega_{\text{p}}} \tag{1.12}$$

$$\begin{aligned} \beta_{\text{ijk}}(\omega = [\omega_{\text{p}} + \omega_{\text{q}}]; \omega_{\text{p}}, \omega_{\text{q}}) \\ = I_{\text{p,q}} \sum_{v \neq g} \sum_{w \neq g} \Bigg[& \frac{\langle \psi_{\text{g}} | \hat{\mu}^{\text{i}} | \psi_{\text{v}} \rangle \langle \psi_{\text{v}} | \bar{\mu}^{\text{k}} | \psi_{\text{w}} \rangle \langle \psi_{\text{w}} | \hat{\mu}^{\text{j}} | \psi_{\text{g}} \rangle}{(E_{\text{gv}} - i\Gamma_{\text{gv}} - \hbar\omega)(E_{\text{gw}} - i\Gamma_{\text{gw}} - \hbar\omega_{\text{p}})} \\ & + \frac{\langle \psi_{\text{g}} | \hat{\mu}^{\text{k}} | \psi_{\text{v}} \rangle \langle \psi_{\text{v}} | \bar{\mu}^{\text{j}} | \psi_{\text{w}} \rangle \langle \psi_{\text{w}} | \hat{\mu}^{\text{i}} | \psi_{\text{g}} \rangle}{(E_{\text{gv}} - i\Gamma_{\text{gv}} + \hbar\omega_{\text{q}})(E_{\text{gw}} - i\Gamma_{\text{gw}} + \hbar\omega)} \\ & + \frac{\langle \psi_{\text{g}} | \hat{\mu}^{\text{k}} | \psi_{\text{v}} \rangle \langle \psi_{\text{v}} | \bar{\mu}^{\text{i}} | \psi_{\text{w}} \rangle \langle \psi_{\text{w}} | \hat{\mu}^{\text{j}} | \psi_{\text{g}} \rangle}{(E_{\text{gv}} - i\Gamma_{\text{gv}} + \hbar\omega_{\text{q}})(E_{\text{gw}} - i\Gamma_{\text{gw}} - \hbar\omega_{\text{p}})} \Bigg] \end{aligned} \tag{1.13}$$

$$\gamma_{\mathrm{ijkl}}\left(\omega = [\omega_{\mathrm{p}} + \omega_{\mathrm{q}} + \omega_{\mathrm{r}}]; \omega_{\mathrm{p}}, \omega_{\mathrm{q}}, \omega_{\mathrm{r}}\right) \tag{1.14}$$

$$= I_{\mathrm{p,q,r}}$$

$$\times \left\{ \sum_{u \neq g} \sum_{v \neq g} \sum_{w \neq g} \left[\frac{\langle \psi_{\mathrm{g}} | \hat{\mu}^{\mathrm{i}} | \psi_{\mathrm{u}} \rangle \langle \psi_{\mathrm{u}} | \bar{\mu}^{\mathrm{l}} | \psi_{\mathrm{v}} \rangle \langle \psi_{\mathrm{v}} | \bar{\mu}^{\mathrm{k}} | \psi_{\mathrm{w}} \rangle \langle \psi_{\mathrm{w}} | \hat{\mu}^{\mathrm{j}} | \psi_{\mathrm{g}} \rangle}{\left(E_{\mathrm{gu}} - i\Gamma_{\mathrm{gu}} - \hbar\omega\right)\left(E_{\mathrm{gv}} - i\Gamma_{\mathrm{gv}} - \hbar\omega_{\mathrm{p}} - \hbar\omega_{\mathrm{q}}\right)\left(E_{\mathrm{gw}} - i\Gamma_{\mathrm{gw}} - \hbar\omega_{\mathrm{p}}\right)} \right.\right.$$

$$+ \frac{\langle \psi_{\mathrm{g}} | \hat{\mu}^{\mathrm{l}} | \psi_{\mathrm{u}} \rangle \langle \psi_{\mathrm{u}} | \bar{\mu}^{\mathrm{i}} | \psi_{\mathrm{v}} \rangle \langle \psi_{\mathrm{v}} | \bar{\mu}^{\mathrm{k}} | \psi_{\mathrm{w}} \rangle \langle \psi_{\mathrm{w}} | \hat{\mu}^{\mathrm{j}} | \psi_{\mathrm{g}} \rangle}{\left(E_{\mathrm{gu}} - i\Gamma_{\mathrm{gu}} + \hbar\omega_{\mathrm{r}}\right)\left(E_{\mathrm{gv}} - i\Gamma_{\mathrm{gv}} - \hbar\omega_{\mathrm{p}} - \hbar\omega_{\mathrm{q}}\right)\left(E_{\mathrm{gw}} - i\Gamma_{\mathrm{gw}} - \hbar\omega_{\mathrm{p}}\right)}$$

$$+ \frac{\langle \psi_{\mathrm{g}} | \hat{\mu}^{\mathrm{j}} | \psi_{\mathrm{u}} \rangle \langle \psi_{\mathrm{u}} | \bar{\mu}^{\mathrm{k}} | \psi_{\mathrm{v}} \rangle \langle \psi_{\mathrm{v}} | \bar{\mu}^{\mathrm{i}} | \psi_{\mathrm{w}} \rangle \langle \psi_{\mathrm{w}} | \hat{\mu}^{\mathrm{l}} | \psi_{\mathrm{g}} \rangle}{\left(E_{\mathrm{gu}} - i\Gamma_{\mathrm{gu}} + \hbar\omega_{\mathrm{p}}\right)\left(E_{\mathrm{gv}} - i\Gamma_{\mathrm{gv}} + \hbar\omega_{\mathrm{p}} + \hbar\omega_{\mathrm{q}}\right)\left(E_{\mathrm{gw}} - i\Gamma_{\mathrm{gw}} - \hbar\omega_{\mathrm{r}}\right)}$$

$$+ \left.\left. \frac{\langle \psi_{\mathrm{g}} | \hat{\mu}^{\mathrm{j}} | \psi_{\mathrm{u}} \rangle \langle \psi_{\mathrm{u}} | \bar{\mu}^{\mathrm{k}} | \psi_{\mathrm{v}} \rangle \langle \psi_{\mathrm{v}} | \bar{\mu}^{\mathrm{l}} | \psi_{\mathrm{w}} \rangle \langle \psi_{\mathrm{w}} | \hat{\mu}^{\mathrm{i}} | \psi_{\mathrm{g}} \rangle}{\left(E_{\mathrm{gu}} - i\Gamma_{\mathrm{gu}} + \hbar\omega_{\mathrm{p}}\right)\left(E_{\mathrm{gv}} - i\Gamma_{\mathrm{gv}} + \hbar\omega_{\mathrm{p}} + \hbar\omega_{\mathrm{q}}\right)\left(E_{\mathrm{gw}} - i\Gamma_{\mathrm{gw}} + \hbar\omega\right)} \right] \right.$$

$$- \sum_{u \neq g} \sum_{w \neq g} \left[\frac{\langle \psi_{\mathrm{g}} | \hat{\mu}^{\mathrm{i}} | \psi_{\mathrm{u}} \rangle \langle \psi_{\mathrm{u}} | \hat{\mu}^{\mathrm{l}} | \psi_{\mathrm{g}} \rangle \langle \psi_{\mathrm{g}} | \hat{\mu}^{\mathrm{k}} | \psi_{\mathrm{w}} \rangle \langle \psi_{\mathrm{w}} | \hat{\mu}^{\mathrm{j}} | \psi_{\mathrm{g}} \rangle}{\left(E_{\mathrm{gu}} - i\Gamma_{\mathrm{gu}} - \hbar\omega\right)\left(E_{\mathrm{gu}} - i\Gamma_{\mathrm{gu}} - \hbar\omega_{\mathrm{r}}\right)\left(E_{\mathrm{gw}} - i\Gamma_{\mathrm{gw}} - \hbar\omega_{\mathrm{p}}\right)} \right.$$

$$+ \frac{\langle \psi_{\mathrm{g}} | \hat{\mu}^{\mathrm{i}} | \psi_{\mathrm{u}} \rangle \langle \psi_{\mathrm{u}} | \hat{\mu}^{\mathrm{l}} | \psi_{\mathrm{g}} \rangle \langle \psi_{\mathrm{g}} | \hat{\mu}^{\mathrm{k}} | \psi_{\mathrm{w}} \rangle \langle \psi_{\mathrm{w}} | \hat{\mu}^{\mathrm{j}} | \psi_{\mathrm{g}} \rangle}{\left(E_{\mathrm{gu}} - i\Gamma_{\mathrm{gu}} - \hbar\omega_{\mathrm{r}}\right)\left(E_{\mathrm{gw}} - i\Gamma_{\mathrm{gw}} + \hbar\omega_{\mathrm{q}}\right)\left(E_{\mathrm{gw}} - i\Gamma_{\mathrm{gw}} - \hbar\omega_{\mathrm{p}}\right)}$$

$$+ \frac{\langle \psi_{\mathrm{g}} | \hat{\mu}^{\mathrm{l}} | \psi_{\mathrm{u}} \rangle \langle \psi_{\mathrm{u}} | \hat{\mu}^{\mathrm{i}} | \psi_{\mathrm{g}} \rangle \langle \psi_{\mathrm{g}} | \hat{\mu}^{\mathrm{j}} | \psi_{\mathrm{w}} \rangle \langle \psi_{\mathrm{w}} | \hat{\mu}^{\mathrm{k}} | \psi_{\mathrm{g}} \rangle}{\left(E_{\mathrm{gu}} - i\Gamma_{\mathrm{gu}} + \hbar\omega\right)\left(E_{\mathrm{gu}} - i\Gamma_{\mathrm{gu}} + \hbar\omega_{\mathrm{r}}\right)\left(E_{\mathrm{gw}} - i\Gamma_{\mathrm{gw}} + \hbar\omega_{\mathrm{p}}\right)}$$

$$+ \left.\left. \frac{\langle \psi_{\mathrm{g}} | \hat{\mu}^{\mathrm{l}} | \psi_{\mathrm{u}} \rangle \langle \psi_{\mathrm{u}} | \hat{\mu}^{\mathrm{i}} | \psi_{\mathrm{g}} \rangle \langle \psi_{\mathrm{g}} | \hat{\mu}^{\mathrm{j}} | \psi_{\mathrm{w}} \rangle \langle \psi_{\mathrm{w}} | \hat{\mu}^{\mathrm{k}} | \psi_{\mathrm{g}} \rangle}{\left(E_{\mathrm{gu}} - i\Gamma_{\mathrm{gu}} + \hbar\omega_{\mathrm{r}}\right)\left(E_{\mathrm{gw}} - i\Gamma_{\mathrm{gw}} - \hbar\omega_{\mathrm{q}}\right)\left(E_{\mathrm{gw}} - i\Gamma_{\mathrm{gw}} + \hbar\omega_{\mathrm{p}}\right)} \right] \right\}$$

where $\hbar\omega_{\mathrm{p,q,r}}$ denote the electric-field energies; g is the electronic ground state and u, v, and w are electronic excited states; $\bar{\mu}_{xy}$ is the transition dipole moment between states x and y if $x \neq y$, or if x and y are the same $\bar{\mu}$ indicates the difference between the state dipole moments of state x and the ground state; E_{gw} is the transition energy from state g to state w; i is the imaginary unit; Γ_{gw} is a damping factor for excited state w related to the excited-state lifetime; and $I_{\mathrm{p,q,r}}$ is the average over the terms obtained by simultaneous permutation of the incident photon frequency and the dipole moment operator.

While the expressions for the higher-order molecular polarizabilities appear complex, they can be greatly simplified through physically reasonable assumptions to more modest forms, as we will show in the following section. We note that the numerators contain only products of state dipole moments and transition dipole moments, while the denominators contain products that include the energies of electronic transitions and of the components of the electric field. Since high-energy excited states necessarily lead to large denominators in the SOS expressions, it is often possible in molecular systems to truncate the sums to only a small handful of low-energy excited states.

1.3. Evolution of the polarizabilities of model organic molecules

To elucidate practical molecular design principles, the relationships outlined within the SOS expressions must be linked to molecular structure.[9,10,19-21] Fortunately, consideration of chromophore chemical structure can lead to dramatic simplifications of the SOS models. As such, we now turn to a discussion of the relationships between the molecular structure and electronic properties of prototypical π-conjugated molecules. Here, we consider as model π-conjugated chromophores (Figure 1.2):

(i) polyenes – neutral structures with an even number of carbon or equivalent atoms along the backbone;

(ii) donor-acceptor substituted polyenes – polyenes with an electron-donating moiety substituted on one end of the molecular structure and an electron-withdrawing group on the opposite end;

(iii) cyanine-like systems (or polymethines) – positively or negatively charged structures with an odd number of carbon or equivalent atoms along the backbone.

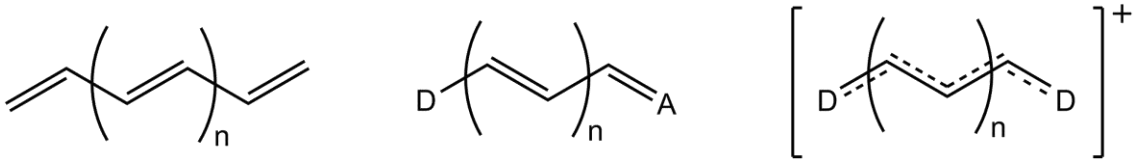

Figure 1.2. General molecular structures of (left) polyenes, (center) donor-acceptor substituted polyenes, and (right) polymethines.

We first focus on rationalizing the interplay between chemical makeup, molecular geometry, and electronic structure, paying particular attention to the bond order and bond length alternation (BOA and BLA, respectively) along the polymethine backbone. From there, we show how key parameters in the SOS expressions for α, β, and γ – the ground-state and excited-state dipole moments, energies of the first several excited states, and transition dipole moments among the first few states – relate to BOA and BLA.

1.3.1. Molecular Orbitals of π-Conjugated Systems

To qualitatively assess the electronic structure of simple π-conjugated systems, we start within the Hückel, or tight-binding, framework.[22-24] Within this model, one can derive a picture of the electronic structure by considering a single p_z orbital on each atom in the π system; the p_z orbitals on adjacent (bonded) atoms are linked electronically by an electronic coupling element β (*aka* resonance or transfer integral). For example, in the simplest π-conjugated structure, ethylene (Figure 1.3), each carbon atom contributes a single p_z orbital, resulting in two π molecular orbitals (MOs): the additive linear

combination of the atomic p_z orbitals leads to a bonding π MO that is energetically stabilized by the β relative to the energy of the isolated p_z atomic orbitals; similarly, the subtractive combination forms an antibonding MO that is energetically destabilized (by an amount equal to β) with a node in the middle of the carbon-carbon bond.

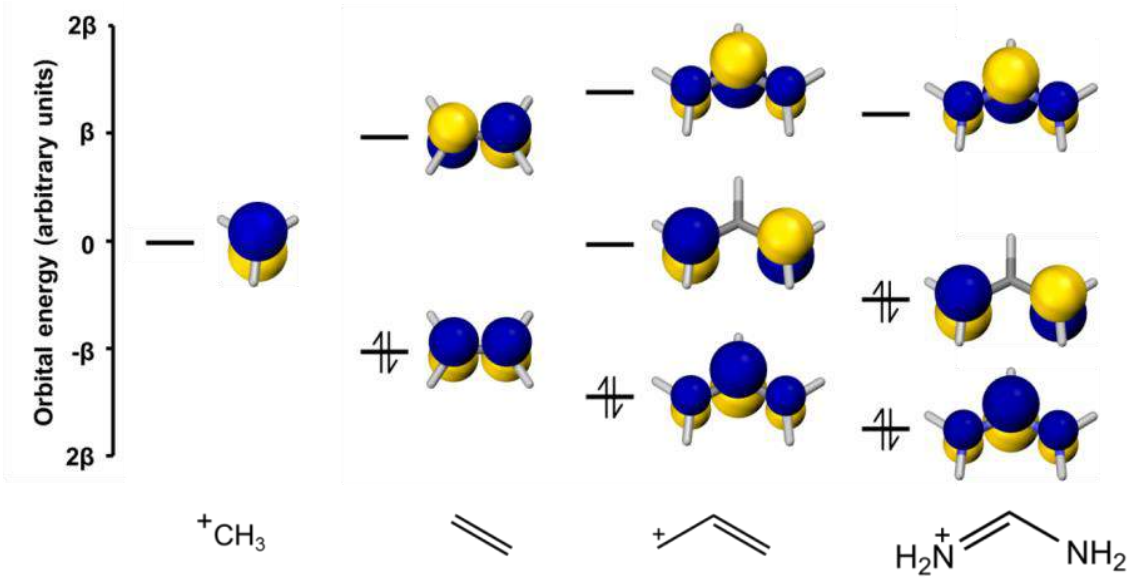

Figure 1.3. Hückel molecular orbitals and energies for ethylene, allyl cation, and the one-carbon streptocyanine.

Adding a third carbon atom to the chain introduces both a third atomic p_z orbital and MO to the electronic structure. As in ethylene, the lowest-energy MO of the allyl radical (a neutral species with spin ½) is bonding across both carbon-carbon bonds, while the highest-energy MO, this time with two nodes, is antibonding across both carbon-carbon bonds. The additional MO in the system has a single node (*i.e.* no electron density) positioned on the central carbon atom and is non-bonding across both carbon-carbon bonds. Within the Hückel model, interactions among atomic orbitals on non-adjacent carbons are neglected, hence the non-bonding allyl MO lies at the zero of energy and is at

the energetic midpoint between the bonding and antibonding MOs. The resulting electronic structure reveals a smaller HOMO-LUMO gap versus ethylene.

Since the atomic orbital contributions to the allyl radical MOs are not equal, ionization (through either removal or addition of an electron) results in an unequal charge distribution across the carbon atoms of the allylic structure.[25] Oxidation results in only the bonding MO being occupied, with each terminal carbon atoms carrying a +½ net atomic charge (the central carbon atom has no net atomic charge); this is a consequence of the MO having one-half of its probability density on the central carbon atom and one-quarter each on the terminal carbon atoms. Reduction to form the allyl anion results in two electrons on the non-bonding MO; as these electrons can only reside on the terminal carbon atoms, these two atoms each carry a –½ net atomic charge.

Of particular interest for the study of the molecular NLO response are streptocyanines: polymethine cations of odd length with terminal amino groups.[25-32] For example, the shortest streptocyanine is formed by replacing the terminal carbon atoms of the allyl cation with nitrogen atoms. Due to the larger electronegativity of nitrogen as compared with carbon and energetic stabilization of the nitrogen p_z orbital *vs*. the carbon p_z orbital, each streptocyanine MO is stabilized as compared with the parent allyl. While the relative stability of the individual MOs of streptocyanines as compared to their all carbon counterparts is dictated by the amount of electron density on each atom, the variations are small relative to the energetic gaps between the MOs, resulting in similar orbital energy correlation diagrams for the two molecular families.

Importantly, the Hückel model does not include electron-electron interactions. It is therefore of interest to compare the electronic structures derived from the Hückel model with those from wavefunction (*i.e.*, Hartree-Fock and variations thereof) or density functional theory methods (Figure 1.4) that explicitly include electron-electron interactions. Inclusion of these interactions in the case of the allyl anion and cation alters the energetic spacing among the MOs and, significantly, results in unequal shifts of the occupied and unoccupied orbital energies and a corresponding widening of the energetic gap between the highest-occupied and lowest-unoccupied MOs (HOMO and LUMO, respectively). Similarly, the HOMO-LUMO energy gap broadens for polyenes.[10,25]

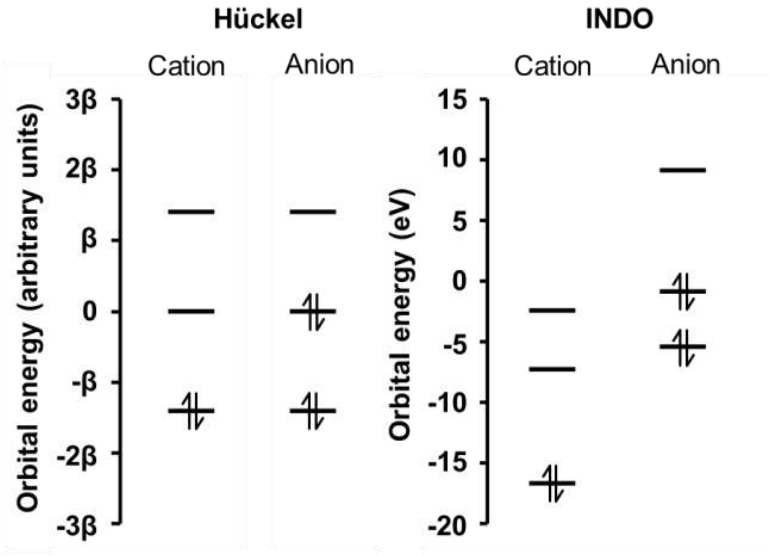

Figure 1.4. Hückel (left) and INDO (right) energies of the π molecular orbitals in the allyl cation and anion (note the differences of the energy axes for the Hückel and INDO correlation diagrams).

As one considers longer polyene (C_{2h} symmetry) and polymethine (C_{2v} symmetry) chains, the considerable differences between the geometric and electronic structures become more apparent. In the neutral polyenes, all carbon atoms possess net atomic

charges close to zero.[25] The HOMO-LUMO gap, as expected, narrows as the system (conjugation) length increases (Figure 1.5), with the degree of stabilization for the HOMO and LUMO being (nearly) symmetric. As a reminder, the nodes of the polyene frontier MOs fall between atoms (*i.e.* on bonds). The nodal pattern found for the HOMO and LUMO, as such, provides a glimpse into the expected geometries of the ground and first-excited states: the HOMO is bonding across the nominally double bonds and antibonding across the nominally single bonds, giving rise to the double-bond–single-bond pattern of the polyene ground state. Conversely, the reverse is true for the LUMO, and one could anticipate the double-bond–single-bond pattern of the first-excited state, when an electron populates the state through photo-excitation, to switch with respect to the ground state.

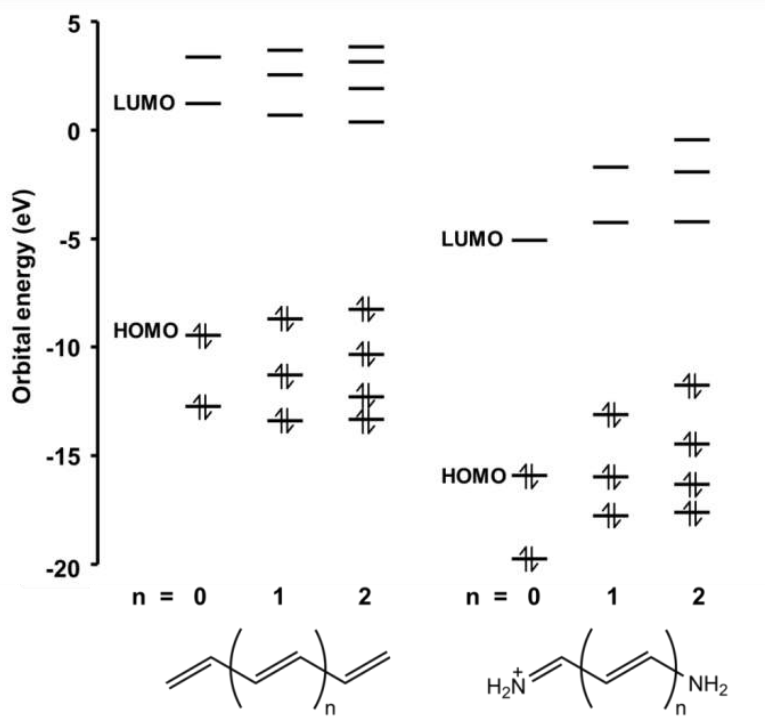

Figure 1.5. Energies of the polyene and polymethine frontier π molecular orbitals as determined at the INDO level.

The difference in the bonding / non-bonding character between adjacent carbon-carbon bonds results in a significant degree of bond-order alternation (BOA ≈ -0.6) – recall that in molecular orbital theory that the bond order between two atoms is the sum over all occupied orbitals of the bonding/antibonding character between the two atoms. As the carbon-carbon bond lengths are highly sensitive to the bond order, there arises a significant degree of bond-length alternation (BLA ≈ 0.1 Å) among the atoms in the polyene backbone.[33,34] We note that here we define BOA and BLA as the difference in average bond orders and lengths, respectively, between the nominally double bonds and the nominally single bonds, so both BOA and BLA can range from positive to negative. By convention, BOA is negative and BLA is positive in polyene-like structures, and their signs are reversed when the pattern of double and single bonds is inverted. BOA and BLA are also sometimes defined as the absolute average of the differences between consecutive bond orders and lengths, respectively, which results in only positive values.

Likewise in the polymethines, the HOMO-LUMO gap decreases with increasing system (conjugation) length. However, here the decrease is associated mostly with a marked energetic destabilization of the HOMO; recall, as well, that the HOMO-LUMO gap in polymethines is smaller than that for polyenes of similar size. Unlike in the polyenes, the wavefunction nodes of the frontier π MOs can fall both on the atoms and on the bonds. For instance, the HOMOs of C_{2v}-symmetric polymethines have nodes on the odd-numbered carbon atoms, resulting in the HOMOs being non-bonding across all bonds.[25,31] Since the HOMOs are largely localized on alternate carbons, the polymethines therefore have a significant degree of charge alternation along the π backbone, in contrast

with the bond-length alternation of the polyenes.[31,35-37] Another consequence of the nodes falling on the atoms is that polymethines present a similar degree of bonding and antibonding character for all bonds along the backbone, resulting in a negligibly small BOA and BLA.[31,37-39] This is reasonable if we conceptualize the polymethine structure as a linear combination of two resonance structures, each with the charge localized on one of the two ends of the molecular structure. Because the double-bond–single-bond pattern is reversed between the two resonance structures, BLA and BOA are an average of the two and are thus close to zero.

The BOA and BLA of linear conjugated systems can be tuned through a variety of routes, including: (i) chemically by adding an electron-donating substituent to one end of the polyene molecular structure and an electron-withdrawing substituent to the opposite end (Figure 1.6), forming a so-called donor–π-bridge–acceptor system; (ii) changing the dielectric constant of the surrounding medium; or (iii) applying an electric field along the length (conjugated path) of the molecule. In a very simplified model, we can conceptualize the resulting ground-state electronic structure as a mixture of two resonance structures: a neutral structure with polyene-like alternation of double and single bonds (left panel of Figure 1.6), and a zwitterionic structure where a full charge is transferred from the donor to the acceptor and the pattern of single and double bonds is reversed relative to the neutral structure (right panel of Figure 1.6). When the donor and acceptor are very weak, the neutral form dominates and the molecular structure is essentially unchanged from the polyene. At the opposite limit of very strong donors and acceptors, the zwitterionic structure dominates and the pattern of single and double bonds

is inverted, resulting in a reversal of the signs of BOA and BLA (Figure 1.7). Critically, at intermediate donor and acceptor strengths, the geometries pass through the cyanine limit, where BOA and BLA necessarily equal zero. As will be discussed in the following section, even small changes in BOA lead to dramatic changes the chromophore linear and non-linear optical properties. The discussion will center around the evolution of the molecular properties as a function of BOA, focusing in particular on the polyene limit (BOA ≈ -0.6), the cyanine limit (BOA = 0), and the zwitterionic limit (BOA ≈ +0.6). Unless otherwise indicated, the molecular properties described in the following sections depend on the magnitude but not the sign of BOA.

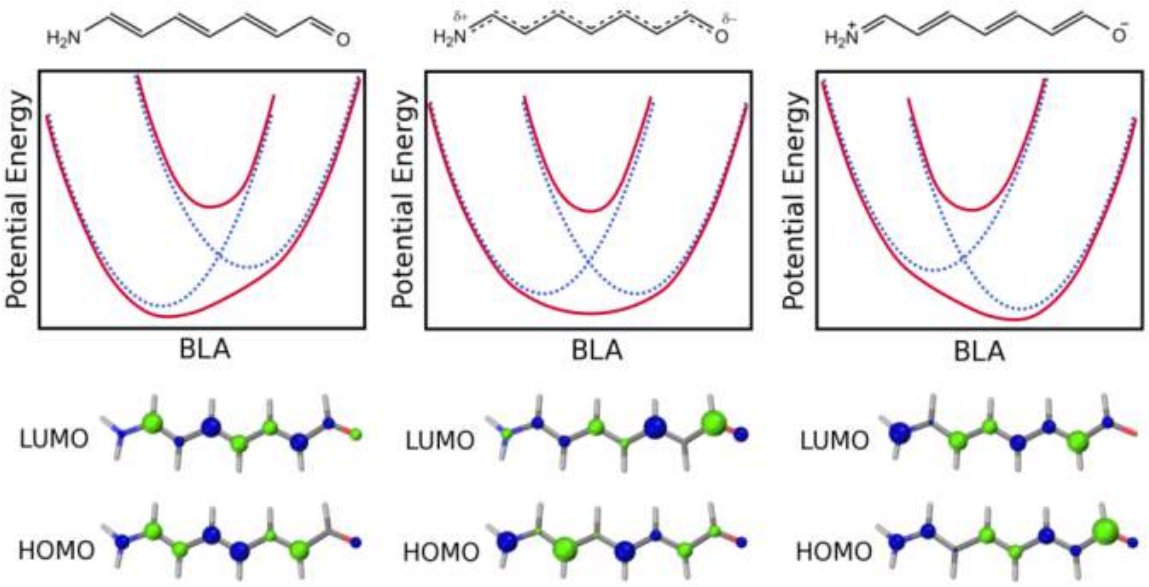

Figure 1.6. Polyene-like, cyanine-like, and zwitterionic valence bond structures for a donor-acceptor substituted polyene.

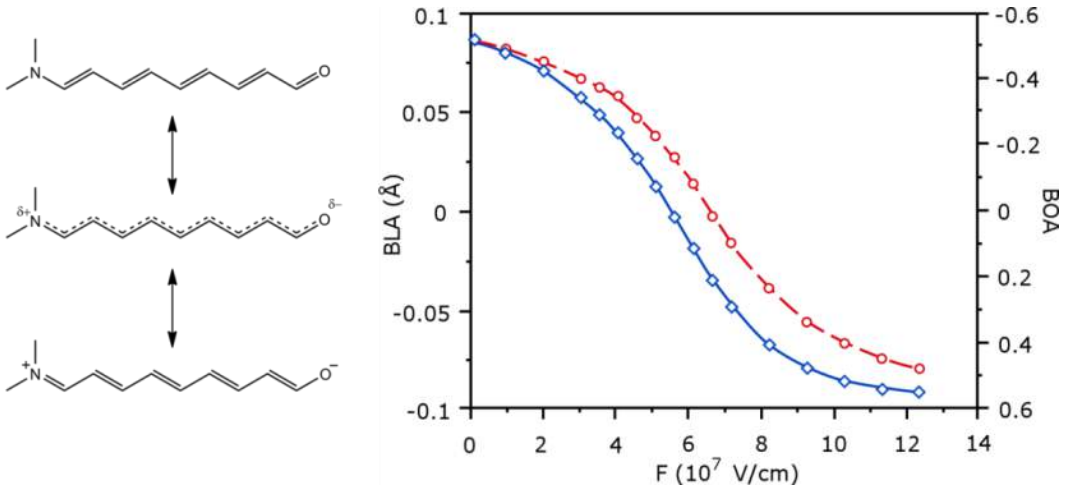

Figure 1.7. (Left) Resonance structures of a prototypical donor-acceptor substituted polyene: (top) neutral (or polyene limit), (center) cyanine limit, and (bottom) zwitterionic limit. (Right) Evolution of bond length alternation (BLA; circles) and bond order alternation (BOA; diamonds) as a function of the applied electric field F along the long molecular axis.[20]

1.3.2. Excited-State Properties of π-Conjugated Systems

We now turn to the excited-state properties of polyenes, donor-acceptor polyenes, and polymethines, with particular focus on the relationship between the ground state (*g*) and the two lowest excited states (defined here as *e* and *e'*). This discussion will revolve around results derived from electronic-structure calculations at the INDO/SDCI level that include a perturbation to the system from an electric field applied along the long-axis of the conjugated structure so as to vary the BOA from the polyene limit (BOA ≈ -0.6) to the zwitterionic limit (BOA ≈ 0.6). State *e* arises from an one-electron excitation from HOMO → LUMO and (for both polyenes and polymethines) has B-type symmetry,[40,41] while state *e'* is of A-type symmetry and is a linear combination of three excitations: two one-electron excitations (HOMO-1 → LUMO and HOMO → LUMO+1) and one two-electron HOMO, HOMO → LUMO, LUMO excitation.[40,41]

A critical change that accompanies the shift in BOA is a shift in the relative transition energies between the ground state and the excited states *e* (E_{ge}) and *e'* ($E_{ge'}$), Figure 1.8. At the polyene limit, $E_{ge'}$ is smaller than E_{ge} for molecules larger than hexatriene,[40,42,43] while at the cyanine limit $E_{ge'}$ is significantly larger than E_{ge}.[32,41,44] Experimentally, the $E_{ge'}/E_{ge}$ ratio in polymethines is observed to be on the order of 1.7.[45] Additionally, E_{ge} is significantly smaller at the cyanine limit than it is at the polyene limit for molecules of the similar length due to the smaller HOMO-LUMO gap.[39] As the molecular lengths are increased, the first two excited-state energies both decrease, but the ratio of their energies and their relative ordering are not significantly affected.

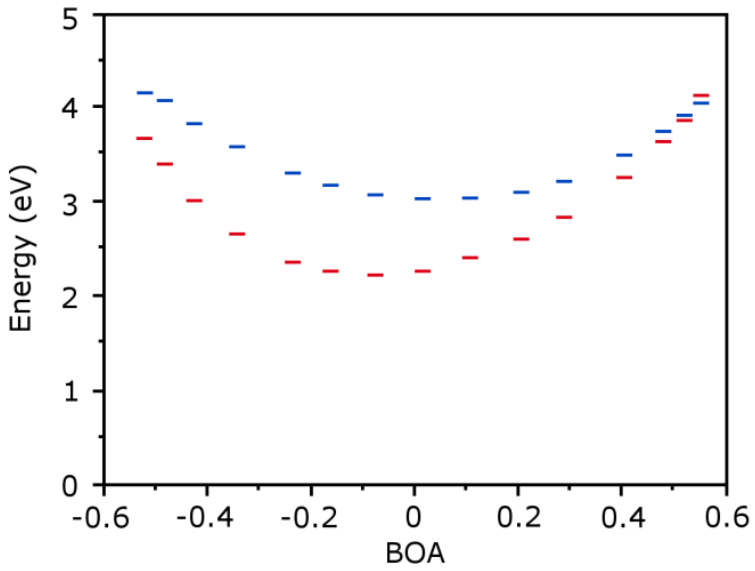

Figure 1.8. Evolution with BOA of the energies of states *e* (red) and *e'* (blue) of a prototypical donor-acceptor substituted polyene at the INDO/SDCI level.[20]

The shape of the OPA and TPA peaks is strongly dependent on the change in molecular geometry upon excitation. At the polyene limit, an excitation from *g* to *e* involves a shift in π-bond density from the nominally double bonds to the nominally single bonds. Thus,

an excitation to state *e* causes a substantial change in equilibrium geometry (as discussed previously), which leads to a broad absorption band with a vibronic progression.[25] The transition from *e* to *e'* similarly involves a significant geometry change. Such considerations imply that both the OPA and TPA peaks are broadened through vibronic effects.

In contrast, at the cyanine limit, a transition from *g* to *e* essentially moves charge from the odd-numbered carbon atoms to the even-numbered carbon atoms along the polymethine backbone and does not alter much the π-bond density or the molecular geometry. MO analysis of the excitation from *e* to *e'* similarly points to a small change in geometry. This suggests that the OPA and TPA peaks will be narrow because of small vibronic coupling, as is observed experimentally.[45] As will be discussed in more detail later, this has important effects in terms of how far the incoming light must be detuned from the excited state energies to avoid unwanted absorption.

Turning our attention to the transition dipole moments among the lowest electronic states, at any value of BOA the transition dipole moment μ_{ge} from the ground state *g* to excited state *e* is large and increases with increasing molecular length. Interestingly, molecules at the cyanine limit have significantly larger μ_{ge} values than molecules of similar length at the polyene limit[39,46] – μ_{ge} is strongly enhanced by reducing BOA as the ground-state and excited-state wavefunctions become quite similar and maintain large spatial overlap. Due to symmetry considerations, the transition dipole moment $\mu_{ge'}$ from the ground state to excited state *e'* is zero in the polyenes (C_{2h}) and negligibly small in the polymethines

(C_{2v}) and in donor-acceptor systems. As will be discussed in detail in Chapter 3, the transition dipole moment $\mu_{ee'}$ between excited states *e* and *e'* is typically relatively small at both the polyene and cyanine limits; however, polyenes also have higher-lying excited states with significant coupling to state *e*.[45]

The state dipole moments of states *g* and *e* also change in correspondence with the change in BOA, and hence there is an evolution of the difference in the state dipole moments $\Delta\mu_{eg}$. The state dipole moment μ_g of the ground state is approximately proportional to the amount of charge transfer from the donor to the acceptor and increases nearly linearly with BOA. In contrast, because state *e* involves a HOMO → LUMO excitation, μ_e depends on the distribution of the LUMO across the molecule. At the polyene, cyanine, and zwitterionic limits, both the HOMO and the LUMO are distributed evenly across the molecule, so $\mu_e = \mu_g$ and $\Delta\mu_{eg} = (\mu_e - \mu_g) = 0$. At negative BOA values between the polyene and cyanine limits, the HOMO is localized primarily on the end of the molecule closer to the donor while the LUMO is localized primarily near the opposite (electron-deficient) end of the molecule. A HOMO → LUMO excitation therefore shifts the electron density from the donor to the acceptor, increasing the molecular dipole moment; hence, $\Delta\mu_{eg}$ is positive. When BOA is positive, this pattern is reversed: the HOMO is localized primarily near the acceptor whereas the LUMO is localized primarily near the donor, so $\Delta\mu_{eg}$ is negative. $\Delta\mu_{eg}$ is maximized when BOA $\approx \pm 0.4$.

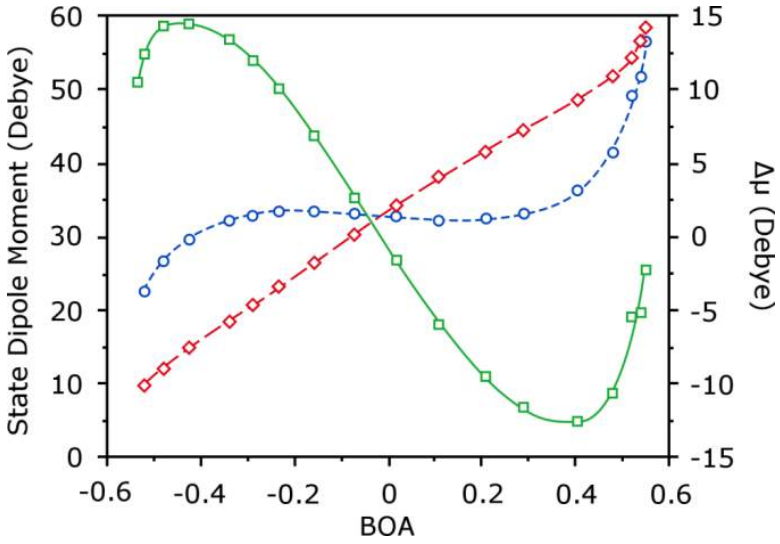

Figure 1.9. Evolution with BOA of μ_g (diamonds), μ_e (circles), and $\Delta\mu_{eg}$ (squares) in a prototypical donor-acceptor substituted polyene.

1.4. The SOS Expression Applied to Molecular Systems

To this point we have defined the derivative relationships between molecular polarizability and energy, developed general SOS expressions for multiple-order polarizabilities, and discussed the relationships between the ground- and excited-state properties the π-conjugated molecules. Now we will bring these topics together by using the excited-state properties discussed in the previous section to understand the dependence of the molecular NLO properties on BLA, and relate those properties to the derivative polarizability relationships. We first consider the polarizabilities at the static limit ($\hbar\omega = 0$), then discuss the effect of changing $\hbar\omega$ on the dynamic NLO properties. As the polarizabilities are complex quantities, we will discuss both the real and imaginary parts. Since the molecules under consideration have the largest components of their polarizabilities along their long (conjugated) axes, with only small contributions coming from the orthogonal directions, we will focus solely on the long-axis polarizabilities of the molecules, defined here as α_{xx}, β_{xxx}, and γ_{xxxx}.

1.4.1. The SOS expression for α_{xx}

For the molecular structures discussed this far, only one low-energy excited state (state *e*) is strongly coupled to the ground state. As such, the SOS expression for α_{ij} (Equation 1.12) can be simplified (again, considering only the long-axis component) to

$$\alpha_{xx} \propto \frac{\mu_{ge}^2}{\left(E_{ge} - \hbar\omega - i\Gamma_{ge}\right)} \qquad 1.15$$

Using this expression, we establish the dependence of α_{xx} on BOA. As discussed above, as BOA approaches the cyanine limit, μ_{ge} increases while E_{ge} decreases, leading to a substantial increase in α_{xx} (Figure 1.10). In fact, polymethines are among the most polarizable molecules known. The increase in α_{xx} when approaching the cyanine limit corresponds with a derivative picture of the polarizability, as compared to Figure 1.7. Since μ_g has a nearly linear relationship with BOA across this series, we can see that BOA (and thus μ_g) are most sensitive to changes in the electric field (and thus α_{xx} is largest) near the cyanine limit.

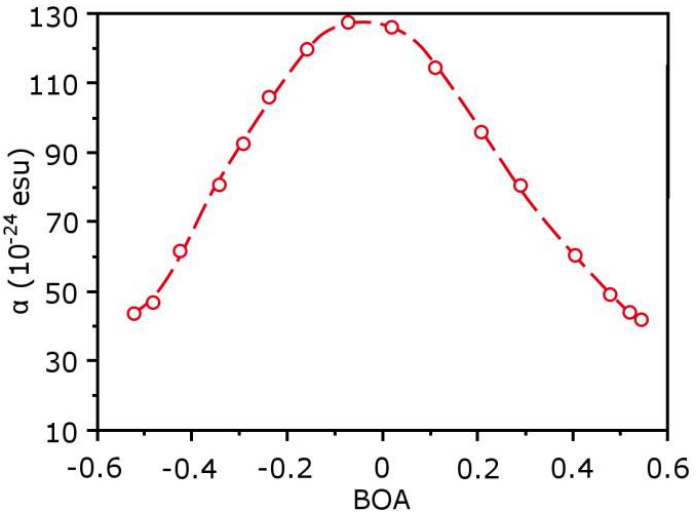

Figure 1.10. Evolution with BOA of α_{xx} in a prototypical donor-acceptor substituted polyene.[20]

The evolution of α_{xx} is also consistent with a physical perspective when we consider α_{xx} as the change in the dipole moment when a weak electric field is applied. As before, we will consider the ground-state structure of a donor-acceptor polyene as a linear combination of the neutral and zwitterion resonance structures. At the cyanine limit, the two resonance structures have the same energy, leading to equal mixing. When a weak external electric field is applied along the long molecular axis, one of the two resonance structures is slightly stabilized relative to the other. Because the energies of the resonance structures are similar, a small change in their relative energies induces a relatively large change in the contribution of each resonance structure to the overall molecular structure; thus, the electric field causes a large polarization of the molecule and α_{xx} is large. In contrast, near the polyene limit, one resonance form is substantially lower in energy than the other and dominates the molecular electronic structure. Even though the electric field causes the same change in the energy gap between the resonance structures as in the cyanine, the lower-energy form still dominates the molecular structure; thus, the electric field causes a smaller polarization and α_{xx} is smaller than in the cyanine case.

The SOS expression for α_{xx} allows us to evaluate the dependence of α_{xx} on the energy $\hbar\omega$ of the incoming light. The denominator in Equation 1.15 includes an imaginary term and the difference between the excitation energy and the energy of the incoming light. As $\hbar\omega$ approaches E_{ge}, the denominator becomes small and the real part $\mathrm{Re}(\alpha_{xx})$ of α increases. This effect is known as pre-resonant enhancement, since α_{xx} is enhanced as $\hbar\omega$ approaches resonance with the first excited state. $\mathrm{Re}(\alpha_{xx})$ is related to the material refractive index (typically reported at optical frequencies) and to the dielectric constant

(typically reported at radio frequencies; at such low frequencies, nuclear and molecular motions also contribute significantly to polarization). When $\hbar\omega$ becomes very close to E_{ge}, the imaginary term $i\Gamma_{ge}$ dominates and Im(α_{xx}) becomes large. The magnitude of Im(α_{xx}) is related to the OPA cross-section of the molecule.

1.4.2. The SOS expression for β_{xxx}

As in the case of α_{ij}, by considering the long-axis static polarizability and assuming that only one low-energy excited state is strongly coupled to the ground state, the SOS expression for β_{ijk} (Equation 1.13) can be simplified to

$$\beta_{xxx} \propto \frac{\mu_{ge}^2 \Delta\mu_{eg}}{\left(E_{ge} - \hbar\omega - i\Gamma_{ge}\right)^2} \qquad 1.16$$

The (μ_{ge}^2/E_{ge}^2) portion of the SOS expression is largest when BOA is small, in a similar manner as α_{xx}. In contrast, $\Delta\mu_{eg}$ is small at the polyene, cyanine, and zwitterionic limits and is large in magnitude at intermediate BOA. By considering the product of these two terms, we see that β_{xxx} is positive between the polyene and cyanine limits and negative between the cyanine and zwitterionic limits (Figure 1.11). β_{xxx} is largest in magnitude when the product of (μ_{ge}^2/E_{ge}^2) and $\Delta\mu_{eg}$ is large; i.e., when BOA is $\approx \pm 0.2$.

The evolution of β_{xxx} determined via the SOS expression corresponds with the derivative relationship between α_{xx} and β_{xxx}. Near the polyene, cyanine, and zwitterionic limits where α_{xx} is relatively constant, β_{xxx} approaches zero. Between these limits, β_{xxx} is positive at negative values of BOA where α_{xx} is increasing, while β_{xxx} is negative at positive values of BOA where α_{xx} is decreasing.

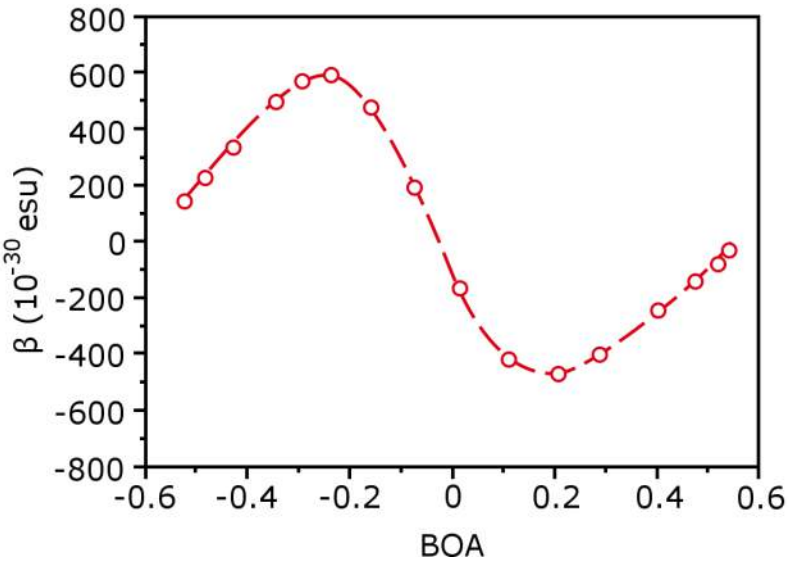

Figure 1.11. Evolution with BOA of β_{xxx} in a prototypical donor-acceptor substituted polyene.[20]

Physically, β_{xxx} is large when the molecule is more susceptible to polarization in one direction than to polarization in the opposite direction. The evolution of β_{xxx} predicted by the SOS expression corresponds with this physical picture. At the polyene and cyanine limits, the molecule is nearly symmetric and is equally susceptible to polarization in either direction, so β_{xxx} is close to zero. At negative values of BOA between these limits, an electric field applied in the positive direction along the long molecular axis polarizes the molecule such that it becomes more cyanine-like and increases the linear polarizability, whereas an electric field applied in the opposite direction polarizes the molecule such that it becomes more polyene-like, decreasing the linear polarizability. The difference in polarizability depending on the direction of the electric field implies that β_{xxx} is positive. If BOA is positive, the reverse is true and β_{xxx} is negative.

As in the case of α_{xx}, the dynamic second-order polarizability β_{xxx} depends on the energy $\hbar\omega$ of the incoming light. As $\hbar\omega$ approaches E_{ge}, the denominator becomes small and β_{xxx} increases due to pre-resonant enhancement. If $\hbar\omega$ is very close to E_{ge}, then linear absorption dependent on Im(α_{xx}) dominates the molecular response.

1.4.3. The SOS expression for γ_{xxxx}

The simplified SOS expression for γ_{ijkl} (Equation 1.1), taking into account the static long-axis component and an assumption that only one excited state is strongly coupled to the ground state, contains three terms:

$$\gamma_{xxxx} \propto \frac{\mu_{ge}^2 \Delta\mu_{eg}^2}{\left(E_{ge} - \hbar\omega - i\Gamma_{ge}\right)^2\left(E_{ge} - 2\hbar\omega - i\Gamma_{ge}\right)} \quad \mathbf{D}$$

$$+ \sum_{e'} \frac{\mu_{ge}^2 \mu_{ee'}^2}{\left(E_{ge} - \hbar\omega - i\Gamma_{ge}\right)^2\left(E_{ge'} - 2\hbar\omega - i\Gamma_{ge'}\right)} \quad \mathbf{T}$$

$$- \frac{\mu_{ge}^4}{\left(E_{ge} - \hbar\omega - i\Gamma_{ge}\right)^3} \quad \mathbf{N} \qquad (1.17)$$

The three terms are denoted **D** (for dipolar term, which is non-zero only in non-centrosymmetric systems), **T** (for two-photon term, which derives from the fact that in centrosymmetric systems this term involves transitions from the one-photon excited state *e* to two-photon absorbing excited states *e'*), and **N** (for negative term, due to the minus sign in front of the term). The first two terms come from the first summation in the full SOS expression; in both cases, we assume that *u* = *w* = state *e*. State *v* in the summation can be either state *e* (in the case of the **D** term) or state *e'* (in the case of the **T** term). The **N** term is a simplification of the second summation in the full expression.

To understand the magnitude of γ_{xxxx}, we need to consider the individual magnitudes of each of the three terms in the SOS expression (Figure 1.12). The **N** term depends only on μ_{ge} and E_{ge}; it has a large negative contribution to γ_{xxxx} when BOA is small and a smaller negative contribution to γ_{xxxx} when BOA is large. The **T** term has an additional dependence on $\mu_{ee'}$ and $E_{ge'}$. Near the cyanine limit, $E_{ge'}$ is substantially larger than E_{ge}, and $\mu_{ee'}$ is typically smaller than μ_{ge}; the **T** term is therefore substantially smaller than the **N** term. Near the polyene limit, $E_{ge'}$ is comparable to E_{ge}, and there are additional two-photon absorbing excited states relatively close in energy to state *e* with non-negligible coupling to state *e*. In this case, the **T** term is somewhat larger than the **N** term. In non-centrosymmetric molecules, the **D** term can also have a significant contribution to γ. Owing to its dependence on $(\Delta\mu_{eg})^2$, the **D** term is 0 at the polyene and cyanine limits and has a significant positive contribution to γ_{xxxx} at intermediate BOA.

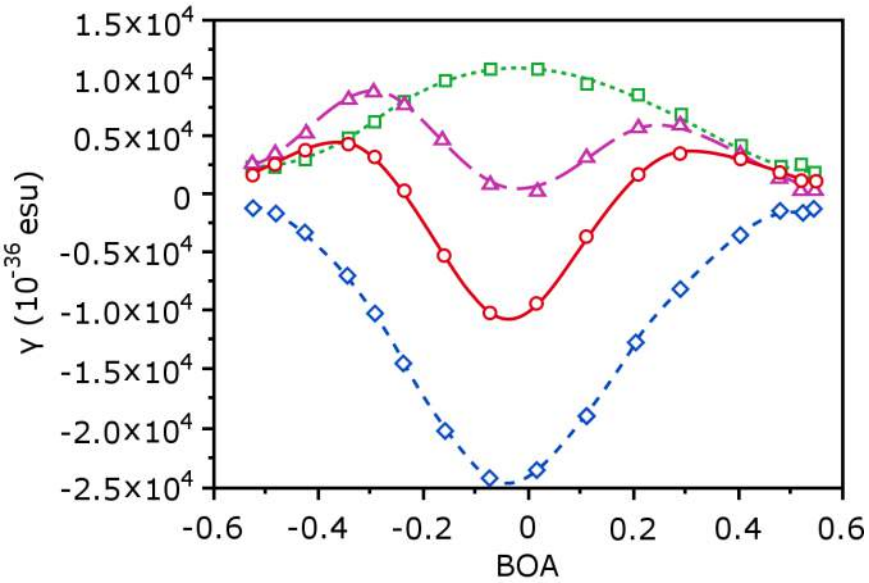

Figure 1.12. Evolution with BOA of γ_{xxxx} (circles & solid line) and the D (triangles; long dashed line), T (squares, short dashed line), and N (diamonds, medium dashed line) terms in a prototypical donor-acceptor substituted polyene.[20]

The sum of these three terms reveals the overall dependence of γ_{xxxx} on BOA. At the polyene limit, the **T** term is slightly larger than the **N** term, so Re(γ_{xxxx}) is small and positive. As the magnitude of BOA decreases, Re(γ_{xxxx}) becomes more positive due to the increasing contribution of the **D** term and reaches its maximum positive value at BOA $\approx \pm 0.3$. At smaller values of BOA, the **N** term dominates, and Re(γ_{xxxx}) becomes large and negative. Re(γ_{xxxx}) reaches its maximum absolute value at the cyanine limit.

The BOA dependence of γ_{xxxx} is consistent with its derivative relationship with β_{xxx}. Re(γ_{xxxx}) passes through zero at BOA $\approx \pm 0.2$, where β_{xxx} reaches its maximum absolute values. The positive peaks in γ_{xxxx} at BOA $\approx \pm 0.3$ correspond to the geometries where β_{xxx} is increasing most steeply, and the large negative peak in γ_{xxxx} at BOA = 0 corresponds to the large negative slope of β_{xxx} in that structure.

From a physical perspective, the BOA dependence of γ_{xxxx} is likewise reasonable. Since γ_{xxxx} corresponds with a quartic term in the molecular energy upon perturbation, we can think of γ_{xxxx} as a change in an "effective α" as the strength of the electric field increases. At the cyanine limit, α_{xx} is extremely large, but a large polarization induced by a strong electric field shifts the molecular geometry toward a structure with larger BOA and smaller α_{xx}. The potential well for polarization is effectively steeper than a harmonic potential would imply, so γ_{xxxx} is large and negative. In contrast, α_{xx} is substantially smaller at the polyene limit than at the cyanine limit, but a large polarization tends to decrease BOA and shift the molecular geometry toward a structure with larger α_{xx}. Thus,

the potential well for polarization is in this case effectively broader than a harmonic potential, so γ_{xxxx} is positive.

Various third-order NLO processes have different dependence on the frequencies of the applied electric fields. For example, third-harmonic generation (THG) is dependent on $\gamma_{xxxx}(3\omega;\omega,\omega,\omega)$ to generate photons at three times the energy of the incoming light. The nonlinear refractive index and TPA depend on the real and imaginary parts, respectively, of $\gamma_{xxxx}(\omega;\omega,-\omega,\omega)$. To understand the TPA cross-section, we note that the denominator in the SOS expression for $\gamma_{xxxx}(\omega;\omega,-\omega,\omega)$ contains both terms with one-photon resonances [($E_{ge} - i\Gamma_{ge} - \hbar\omega$) terms in the denominators of all three terms] and terms with two-photon resonances [($E_{ge} - i\Gamma_{ge} - 2\hbar\omega$) and ($E_{ge'} - i\Gamma_{ge'} - 2\hbar\omega$) terms in the denominators of the **D** and **T** terms, respectively]. At a two-photon resonance, the molecule will exhibit two-photon absorption (TPA) directly proportional to Im(γ_{xxxx}). The TPA cross-section δ_{TPA} is largest if E_{ge} is relatively close to $\hbar\omega$, so as to obtain pre-resonant enhancement; because the light is close in energy to a one-photon resonance, all terms in the denominator will be small. However, if E_{ge} is too close to $\hbar\omega$, one-photon absorption will dominate.

As discussed previously, AOS applications require a very large |Re(γ_{xxxx})| and a FOM >> 4π. To achieve a large |Re(γ_{xxxx})|, $\hbar\omega$ can be tuned to be close to E_{ge} to attain significant pre-resonant enhancement. However, some care must be taken to avoid TPA. One major advantage of polymethines is that |Re(γ_{xxxx})| is inherently maximized at the cyanine limit. In addition, the excited-state spacing of polymethines provides benefits for AOS (Figure

1.13). In polyenes and most other π-conjugated systems, the first OPA and TPA states are similar in energy, and the peaks are significantly broadened due to vibronic coupling. In this situation, to avoid losses due to TPA, the energy $\hbar\omega$ of the incoming light must be less than half the energy of the first TPA state. This limits the magnitude of $\mathrm{Re}(\gamma_{xxxx})$ because there is little pre-resonant enhancement. In contrast, polymethines have both a substantial energy gap between states *e* and *e'* and narrow absorption peaks. Thus, $\hbar\omega$ can be larger such that $E_{ge} < 2\hbar\omega < E_{ge'}$ while still avoiding significant TPA. Because the energy difference between E_{ge} and $\hbar\omega$ is small in this case, $\mathrm{Re}(\gamma_{xxxx})$ can be much larger due to pre-resonant enhancement. The requisite figure-of-merit for AOS has recently been achieved in selenopyrylium polymethines in dilute solution.[47]

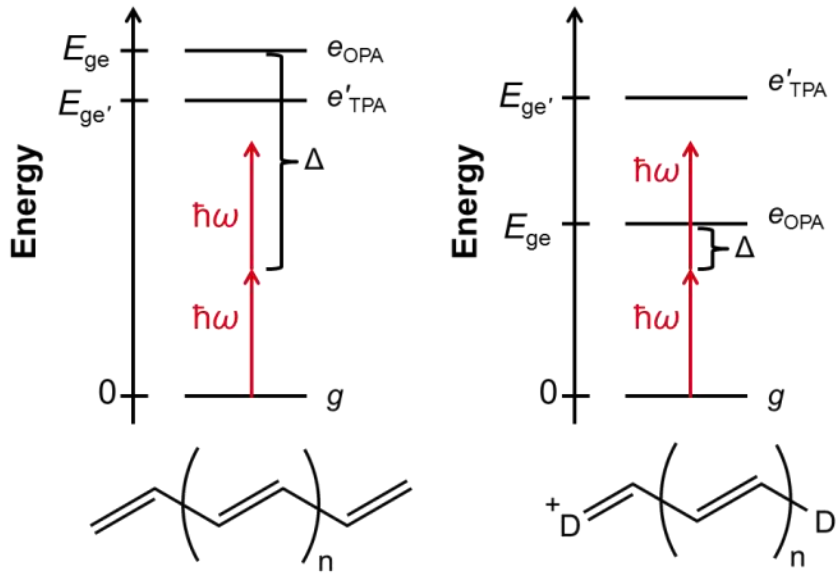

Figure 1.13. Schematic energy-state diagrams for: a) typical π-conjugated chromophores such as polyenes; and b) cyanine-type molecules. The ground-state is marked as *g*, the first one-photon allowed excited state as e_{OPA} and the first two-photon allowed excited state as *e'*; the energy of the optical signal is represented by $\hbar\omega$ and the detuning between the input photon energy and the energy of the state *e* is given by Δ.[47]

1.5. Effects of Environment

Despite the favorable molecular NLO properties of polymethines for AOS applications, translating these properties from the isolated molecules to materials with a large $Re(\chi^{(3)})$ suitable for devices has proven quite challenging. Although to this point we have focused on the structure-property relationships for isolated molecules, the interactions between the polymethines and their environment (*e.g.* solvent, counterion, other polymethines) play a key role in determining their optical and NLO properties. Understanding and controlling these effects will be critical to develop polymethine-based materials that can be used in device applications.

1.5.1. Effects of counterion and solvent

In solution, long polymethines often do not maintain symmetric geometries, leading to dramatic changes in terms of their linear and nonlinear optical properties. The experimental absorption spectra of long polymethines in solution have broad absorption peaks[48-51] and significant reduction in their linear absorption,[52,53] suggesting that their symmetric cyanine-like character is lost. Even a relatively small increase in BLA can significantly reduce the magnitude of $Re(\gamma)$.[19,20] Notably, the length at which symmetry breaking occurs is strongly dependent on the polymethine structure and environment; the onset of symmetry breaking has been observed in molecules with polymethine bridges as short as three carbon atoms[54] or longer than thirteen carbon atoms.[55]

Polymethine symmetry breaking is due to a delicate interplay between solvent and counterion effects. For certain long polymethines, the OPA peak becomes broader in

more polar solvents, suggesting that the key interaction leading to symmetry-breaking is stabilization of the charge-localized geometry by the solvent.[56] In contrast, for some polymethines of moderate length, polymethine-counterion interactions can become the driving force for symmetry breaking: the absorption peak is significantly broadened in less polar solvents, particularly with small counterions such as halides.[52] Although the extent of localization of the wavefunction[29,57] and the dynamics of ion-pairing are particularly challenging to model, computational studies can provide some insight into the polymethine-counterion interactions.[32,58,59] In long polymethines, the counterion tends to localize near one end of the molecule, causing a significant increase in BLA and reduction in $|\mathrm{Re}(\gamma)|$.[32] Consideration of implicit solvation shields the interaction between the polymethine and counterion such that the geometries and NLO properties of the polymethines become more similar to those of the isolated polymethine.

1.5.2. Effect of aggregation

Polymethines have long been known to aggregate,[60] dramatically changing their optical and NLO properties. Experimental evidence suggests that both J-aggregates (slipped geometry; bathochromic shift)[61-70] and H-aggregates (cofacial geometry; hypsochromic shift)[71-75] occur for various polymethines, as well as perpendicular aggregates[76] and more complex structures.[77-79] This aggregation can dramatically affect the polymethine NLO properties. Crystal structures suggest that polymethine-polymethine interactions within aggregates can induce symmetry-breaking and increase BLA,[80] shifting the molecular properties from cyanine-like toward polyene-like. Aggregation can also close the window

between the polymethine first and second excited states[32] and enhance TPA by an order of magnitude,[81] making it more challenging to achieve the requisite FOM for AOS.

1.6. Thesis Objectives and Outlook

The recent development of polymethines with the requisite FOM for AOS in dilute solution[16] has been a critical step toward realizing AOS devices. These NLO properties must now be translated to thin films with large polymethine concentrations to achieve a large $\mathrm{Re}(\chi^{(3)})$ while maintaining a large FOM. This requires elucidating several important relationships between the polymethine structure and the molecular and macroscopic properties. Although many of the fundamental structure-property relationships determining the NLO properties of the isolated polymethines have been explored, more work is still needed to fully understand the polymethine second excited state properties and the NLO properties of the large π-conjugated counterions used to minimize aggregation. Because maintaining symmetric polymethine geometries is critical to maintain cyanine-like NLO properties, the roles of solvent and the counterion electric field on molecular symmetry must be understood. In addition, as polymethine-polymethine interactions have a significant detrimental effect on the NLO properties, the geometries and electronic properties of polymethine aggregates as large concentration must be evaluated.

The emphasis of the work described here is on theoretical investigations of the structure-property relationships that determine the third-order nonlinear optical properties of polymethines and polymethine-based materials. These investigations include quantum-

chemical evaluation of the polymethine and counterion geometric and electronic structures and excited-state properties, in addition to molecular dynamics studies of the geometries of polymethine bulk aggregation.

In Chapter 2, we review the theoretical approaches relevant to the work described in this thesis. We first describe quantum-mechanical approaches: we begin with the Schrödinger equation and Hartree-Fock, then turn to semiempirical and post-Hartree-Fock methods; finally, we describe the basic principles of Density Functional Theory and various approximate functionals. We end with a description of atomistic force fields and the principles of molecular dynamics.

Chapters 3-5 describe theoretical studies of the molecular properties of polymethines. Focusing initially on C_{2v}-symmetric polymethines, in Chapter 3 we decompose the transition dipole moment $\mu_{ee'}$ between the polymethine first and second excited states into component transitions to understand its dependence on polymethine length and substituents. In particular, we show that the magnitude of $\mu_{ee'}$ depends on the spatial extent and energetic spacing of the first several frontier molecular orbitals. Turning to symmetry-broken structures, in Chapter 4 we discuss the relationship between BLA, which describes the polymethine geometric structure, and BOA, which probes the polymethine electronic structure. We show that BOA is a more broadly applicable predictor of the molecular NLO properties than is BLA, particularly when considering non-equilibrium geometries. In Chapter 5, we theoretically evaluate the length of the onset of polymethine symmetry-breaking. We analyze the polymethine vibrational

spectra and present preliminary evidence on the potential energy surfaces displaced along key vibrational modes.

In Chapter 6, we show that the XPh_4 systems, which are used as bulky counterions to minimize polymethine symmetry-breaking, have small negative Re(γ) values. We show that unlike in polymethines, these systems have a band of excited states involving single-electron excitations within the π-system, several of which have significant coupling to the ground state.

Finally, we describe molecular dynamics studies of polymethine bulk aggregation in Chapter 7, focusing in particular on the geometries of polymethine-counterion and polymethine-polymethine interactions and the electronic couplings between polymethines. We evaluate the effect of counterion size on the aggregation of prototypical streptocyanines and the effect of bulky substituents on the aggregation of thiopyrylium polymethines.

1.7. References

(1) Cisco Visual Networking Index: Forecast and Methodology, 2013–2018 (White Paper). [Online Early Access]. Published Online: 2014.

(2) *Optical fiber telecommunications IV*; San Diego: Academic Press, 2002.

(3) Ramaswami, R. *Optical networks : a practical perspective*; San Francisco: Morgan Kaufmann Publishers, 1998.

(4) Hinton, H. S. *IEEE Spectrum* **1992**, *29*, 42.

(5) Albores-Mejia, A.; Gomez-Agis, F.; Dorren, H. J. S.; Leijtens, X. J. M.; De Vries, T.; Yok-Siang, O.; Heck, M. J. R.; Notzel, R.; Robbins, D. J.; Smit, M. K.; Williams, K. A. *J. Lightwave Technol.* **2010**, *28*, 2984.

(6) Gibbs, H. M. *Optical bistability : controlling light with light*; Orlando: Academic Press, 1985.

(7) Stegeman, G. I.; Wright, E. M.; Finlayson, N.; Zanoni, R.; Seaton, C. T. *J. Lightwave Technol.* **1988**, *6*, 953.

(8) Stegeman, G. I.; Wright, E. M. *Optical and Quantum Electronics* **1990**, *22*, 95.

(9) Hales, J. M.; Barlow, S.; Kim, H.; Mukhopadhyay, S.; Brédas, J.-L.; Perry, J. W.; Marder, S. R. *Chem. Mater.* **2014**, *26*, 549.

(10) Gieseking, R. L.; Mukhopadhyay, S.; Risko, C.; Marder, S. R.; Brédas, J.-L. *Adv. Mater.* **2014**, *26*, 68.

(11) *Photonics in switching*; Boston: Academic Press, 1993.

(12) Driessen, A.; Hoekstra, H.; Horst, F.; Krijnen, G. J. M.; Offrein, B. J.; van Schoot, J. B. P.; Lambeck, P. V.; Popma, T. J. A. *IEE Proceedings-Optoelectronics* **1998**, *145*, 227.

(13) Boyd, R. W. *Nonlinear optics*; 2nd ed. ed.; San Diego, Calif.: Academic Press, 2003.

(14) Stegeman, G. I.; Torruellas, W. E. *Phil. Trans. R. Soc. A* **1996**, *354*, 745.

(15) Mizrahi, V.; Delong, K. W.; Stegeman, G. I.; Saifi, M. A.; Andrejco, M. J. *Opt. Lett.* **1989**, *14*, 1140.

(16) Hales, J. M.; Matichak, J.; Barlow, S.; Ohira, S.; Yesudas, K.; Bredas, J.-L.; Perry, J. W.; Marder, S. R. *Science* **2010**, *327*, 1485.

(17) Stegeman, G. I.; Torruellas, W. In *Electrical, Optical, and Magnetic Properties of Organic Solid State Materials*; Garito, A. F., Jen, A. K. Y., Lee, C. Y. C., Dalton, L. R., Eds. 1994; Vol. 328, p 397.

(18) Orr, B. J.; Ward, J. F. *Mol. Phys.* **1971**, *20*, 513.

(19) Marder, S. R.; Gorman, C. B.; Meyers, F.; Perry, J. W.; Bourhill, G.; Brédas, J. L.; Pierce, B. M. *Science* **1994**, *265*, 632.

(20) Meyers, F.; Marder, S. R.; Pierce, B. M.; Bredas, J. L. *J. Am. Chem. Soc.* **1994**, *116*, 10703.

(21) Bredas, J. L.; Adant, C.; Tackx, P.; Persoons, A.; Pierce, B. M. *Chem. Rev.* **1994**, *94*, 243.

(22) Hückel, E. *Z. Phys.* **1931**, *70*, 204.

(23) Hückel, E. *Z. Phys.* **1931**, *72*, 310.

(24) Hückel, E. *Z. Phys.* **1932**, *76*, 628.

(25) Salem, L. *The molecular orbital theory of conjugated systems*; 4th print. with corrections ed.; W. A. Benjamin: Reading, Mass., 1974, c1966.

(26) Johr, T.; Wernke, W.; Pfeiffer, M.; Lau, A.; Dahne, L. *Chem. Phys. Lett.* **1995**, *246*, 521.

(27) Wernke, W.; Pfeiffer, M.; Johr, T.; Lau, A.; Grahn, W.; Johannes, H.-H.; Dahne, L. *Chem. Phys.* **1997**, *216*, 337.

(28) Fabian, J. *J. Mol. Struct.: THEOCHEM* **2006**, *766*, 49.

(29) Iordanov, T. D.; Davis, J. L.; Masunov, A. E.; Levenson, A.; Przhonska, O. V.; Kachkovski, A. D. *Int. J. Quantum Chem.* **2009**, *109*, 3592.

(30) Fabian, J. *Dyes Pigm.* **2010**, *84*, 36.

(31) Jacquemin, D. *J. Phys. Chem. A* **2011**, *115*, 2442.

(32) Mukhopadhyay, S.; Risko, C.; Marder, S. R.; Bredas, J. L. *Chem. Sci.* **2012**, *3*, 3103.

(33) Drenth, W.; Wiebenga, E. H. **1955**.

(34) Baughman, R. H.; Kohler, B. E.; Levy, I. J.; Spangler, C. *Synth. Met.* **1985**, *11*, 37.

(35) Dahne, S.; Ranft, J. Z. *Z. Phys. Chem.* **1963**, *224*, 65.

(36) Dahne, S.; Kulpe, S. *Abh. Akad. Wiss. DDR, Abt. Math. Naturwiss., Tech.* **1977**, *8*, 1.

(37) Kachkovski, A. D.; Dekhtyar, M. L. *Dyes Pigm.* **1996**, *30*, 43.

(38) Groth, P. *Acta Chem. Scand., Ser. B* **1987**, *41*, 547.

(39) Meyers, F.; Marder, S. R.; Pierce, B. M.; Bredas, J. L. *J. Am. Chem. Soc.* **1994**, *116*, 10703.

(40) Angeli, C.; Pastore, M. *J. Chem. Phys.* **2011**, *134*, 184302.

(41) Schreiber, M.; Buß, V.; Fülscher, M. P. *Phys. Chem. Chem. Phys.* **2001**, *3*, 3906.

(42) Cave, R. J.; Davidson, E. R. *J. Phys. Chem.* **1988**, *92*, 614.

(43) Lappe, J.; Cave, R. J. *J. Phys. Chem. A* **2000**, *104*, 2294.

(44) Send, R.; Valsson, O.; Filippi, C. *J. Chem. Theory Comput.* **2011**, *7*, 444.

(45) Fu, J.; Padilha, L. A.; Hagan, D. J.; Van Stryland, E. W.; Przhonska, O. V.; Bondar, M. V.; Slominsky, Y. L.; Kachkovskii, A. *J. Opt. Soc. Am. B: Opt. Phys.* **2007**, *24*, 56.

(46) Kachkovsky, A.; Pilipchuk, N.; Kurdyukov, V.; Tolmachev, A. *Dyes Pigm.* **2006**, *70*, 212.

(47) Hales, J. M.; Matichak, J.; Barlow, S.; Ohira, S.; Yesudas, K.; Bredas, J. L.; Perry, J. W.; Marder, S. R. *Science* **2010**, *327*, 1485.

(48) Tolbert, L. M.; Zhao, X. *J. Am. Chem. Soc.* **1997**, *119*, 3253.

(49) Terenziani, F.; Przhonska, O. V.; Webster, S.; Padilha, L. A.; Slominskii, Y. L.; Davydenko, I. G.; Gerasov, A. O.; Kovtun, Y. P.; Shandura, M. P.; Kachkovski, A. D.; Hagan, D. J.; Van Stryland, E. W.; Painelli, A. *J. Phys. Chem. Lett.* **2010**, *1*, 1800.

(50) Kachkovski, O. D.; Tolmachov, O. I.; Slominskii, Y. L.; Kudinova, M. O.; Derevyanko, N. O.; Zhukova, O. O. *Dyes Pigm.* **2005**, *64*, 207.

(51) Lepkowicz, R. S.; Przhonska, O. V.; Hales, J. M.; Fu, J.; Hagan, D. J.; Van Stryland, E. W.; Bondar, M. V.; Slominsky, Y. L.; Kachkovski, A. D. *Chem. Phys.* **2004**, *305*, 259.

(52) Bouit, P.-A.; Aronica, C.; Toupet, L.; Guennic, B. L.; Andraud, C.; Maury, O. *J. Am. Chem. Soc.* **2010**, *132*, 4328.

(53) Hu, H.; Przhonska, O. V.; Terenziani, F.; Painelli, A.; Fishman, D.; Ensley, T. R.; Reichert, M.; Webster, S.; Bricks, J. L.; Kachkovski, A. D.; Hagan, D. J.; Van Stryland, E. W. *Phys. Chem. Chem. Phys.* **2013**, *15*, 7666.

(54) Barlow, S.; Henling, L. M.; Day, M. W.; Marder, S. R. *Chem. Commun.* **1999**, 1567.

(55) Tolbert, L. M.; Ogle, M. E. *J. Am. Chem. Soc.* **1990**, *112*, 9519.

(56) Lepkowicz, R. S.; Przhonska, O. V.; Hales, J. M.; Fu, J.; Hagan, D. J.; Van Stryland, E. W.; Bondar, M. V.; Slominsky, Y. L.; Kachkovski, A. D. *Chemical Physics* **2004**, *305*, 259.

(57) Fabian, J. *Journal of Molecular Structure: THEOCHEM* **2006**, *766*, 49.

(58) Karaman, R.; Menger, F. M. *J. Mol. Struct.: THEOCHEM* **2010**, *959*, 87.

(59) Bamgbelu, A.; Wang, J.; Leszczynski, J. *J. Phys. Chem. A* **2010**, *114*, 3551.

(60) Jelley, E. E. *Nature* **1936**, *138*, 1009.

(61) Aydin, M.; Jean-Mary, F.; Stevens, N.; Akins, D. L. *J. Phys. Chem. B* **2004**, *108*, 9695.

(62) Busse, G.; Frederichs, B.; Petrov, N. K.; Techert, S. *Phys. Chem. Chem. Phys.* **2004**, *6*, 3309.

(63) Kawabe, Y.; Kato, S.; Honda, M.; Yoshida, J. *Proc. SPIE* **2010**, *7765*, 776503.

(64) Kemnitz, K.; Yoshihara, K.; Tani, T. *J. Phys. Chem.* **1990**, *94*, 3099.

(65) Li, Z.-Y.; Jin, Z.-H.; Kasatani, K.; Okamoto, H. *Chin. Phys. Lett.* **2005**, *22*, 2571.

(66) Belfield, K. D.; Bondar, M. V.; Hernandez, F. E.; Przhonska, O. V.; Yao, S. *Chem. Phys.* **2006**, *320*, 118.

(67) Shelkovnikov, V. V.; Markov, R. V.; Plekhanov, A. I.; Simanchuk, A. E.; Ivanova, Z. M. *High Energy Chem.* **2002**, *36*, 260.

(68) Tanaka, J.; Tanaka, M.; Hayakawa, M. *Bull. Chem. Soc. Jpn.* **1980**, *53*, 3109.

(69) Tani, K.; Ito, C.; Hanawa, Y.; Uchida, M.; Otaguro, K.; Horiuchi, H.; Hiratsuka, H. *J. Phys. Chem. B* **2008**, *112*, 836.

(70) Virgili, T.; Clark, J.; Cabanillas-Gonzalez, J.; Bazzana, L.; Vishnubhatla, K. C.; Osellame, R.; Ramponi, R.; Lanzani, G. *J. Mater. Chem.* **2010**, *20*, 519.

(71) Baraldi, I.; Caselli, M.; Momicchioli, F.; Ponterini, G.; Vanossi, D. *Chem. Phys.* **2002**, *275*, 149.

(72) Batchelor, E. K.; Gadde, S.; Kaifer, A. E. *Supramolec. Chem.* **2010**, *22*, 40.

(73) Caselli, M.; Latterini, L.; Ponterini, G. *Phys. Chem. Chem. Phys.* **2004**, *6*, 3857.

(74) Gadde, S.; Batchelor, E. K.; Weiss, J. P.; Ling, Y.; Kaifer, A. E. *J. Am. Chem. Soc.* **2008**, *130*, 17114.

(75) Moritz, E. D.; Sahyun, M. R. V. *J. Photochem. Photobiol., A* **2005**, *169*, 211.

(76) Etter, M. C.; Kress, R. B.; Bernstein, J.; Cash, D. J. *J. Am. Chem. Soc.* **1984**, *106*, 6921.

(77) Didraga, C.; Pugzlys, A.; Hania, P. R.; von Berlepsch, H.; Duppen, K.; Knoester, J. *J. Phys. Chem. B* **2004**, *108*, 14976.

(78) Mishra, A.; Behera, R. K.; Behera, P. K.; Mishra, B. K.; Behera, G. B. *Chem. Rev.* **2000**, *100*, 1973.

(79) von Berlepsch, H.; Böttcher, C.; Dähne, L. *J. Phys. Chem. B* **2000**, *104*, 8792.

(80) Dahne, L.; Reck, G. *Angew. Chem. Int. Ed.* **1995**, *34*, 690.

(81) Belfield, K. D.; Bondar, M. V.; Hernandez, F. E.; Przhonska, O. V.; Yao, S. *Chemical Physics* **2006**, *320*, 118.

CHAPTER 2

THEORETICAL METHODOLOGY

In this chapter, we review the computational methodologies used to study the ground-state and excited-state properties of π-conjugated molecules and materials. We first discuss electronic-structure approaches, introducing Hartree-Fock and the related semiempirical and post-Hartree-Fock methodologies, then overview Density Functional Theory approaches and various approximate functionals. Finally, we discuss atomistic simulation approaches, including the energetic terms in the force fields and the principles of dynamics simulations. The notation and terminology here are adapted primarily from Szabo and Ostlund,[1] Jensen,[2] Frenkel and Smit,[3] and Koch and Holthausen.[4]

2.1. Electronic Structure Methods

2.1.1. Schrödinger Equation

The quantum nature of a system of particles can be described using the time-independent Schrodinger equation,

$$\mathbf{H}\Psi_i = E_i\Psi_i \tag{2.1}$$

where **H** is the Hamiltonian operator for a system of nuclei and electrons, E_i is the energy of the system in eigenstate *i*, and Ψ_i is the wavefunction of the system in eigenstate *i*. The Hamiltonian for a system of *M* nuclei (n) and *N* electrons (e) can be written in terms of a sum of potential energy terms (**T**) and kinetic energy terms (**V**) as (in atomic units)

$$\mathbf{H}_{\text{tot}} = \mathbf{T}_{\text{e}} + \mathbf{T}_{\text{n}} + \mathbf{V}_{\text{ne}} + \mathbf{V}_{\text{ee}} + \mathbf{V}_{\text{nn}} \tag{2.2}$$

$$= -\frac{1}{2}\sum_{i=1}^{N}\nabla_i^2 - \frac{1}{2}\sum_{A=1}^{M}\frac{1}{M_A}\nabla_A^2 - \sum_{i=1}^{N}\sum_{A=1}^{M}\frac{Z_A}{r_{iA}} + \sum_{i=1}^{N}\sum_{j>i}^{N}\frac{1}{r_{ij}} + \sum_{A=1}^{M}\sum_{B>A}^{M}\frac{Z_A Z_B}{r_{AB}}$$

where M_A is the ratio of the mass of nucleus A to the mass of an electron; Z_A is the atomic number of nucleus A; Laplacian operators ∇_i^2 and ∇_A^2 indicate the second partial derivatives with respect to the coordinates of electron i and nucleus A, respectively; and r_{xy} is the distance between particles x and y.

2.1.2. Born-Oppenheimer Approximation

Because the Schrödinger equation contains many degrees of freedom, exact solutions are only available for the simplest systems. For systems of chemical interest, approximations must be made. Since even the lightest nuclei are more than three orders of magnitude heavier than electrons, the nuclei move much more slowly than do the electrons. In most systems, it is thus reasonable to assume that the motion of the electrons and the nuclei can be separated. The electrons can be treated as moving in a field of fixed nuclei, referred to as the Born-Oppenheimer approximation. This simplifies several terms of the Hamiltonian: the kinetic energy of the nuclei $\mathbf{T}_{\text{n}}$ can be neglected, and the repulsion of the nuclei $\mathbf{V}_{\text{nn}}$ can be treated as a constant. This results in the electronic Hamiltonian

$$\mathbf{H}_{\text{elec}} = -\sum_{i=1}^{N}\frac{1}{2}\nabla_i^2 - \sum_{i=1}^{N}\sum_{A=1}^{M}\frac{Z_A}{r_{iA}} + \sum_{i=1}^{N}\sum_{j>i}^{N}\frac{1}{r_{ij}} \tag{2.3}$$

which leads to the electronic Schrödinger equation

$$\mathbf{H}_{\text{elec}}\Psi_{\text{elec}} = E_{\text{elec}}\Psi_{\text{elec}} \tag{2.4}$$

where Ψ_{elec} is the electronic wavefunction, which depends explicitly on the electron coordinates but only parametrically on the nuclear coordinates. The total energy is

$$E_{\text{tot}} = E_{\text{elec}} + E_{\text{nuc}} \tag{2.5}$$

where E_{nuc} is the nuclear repulsion energy.

2.1.3. Hartree-Fock Approximation

Even with the simplifications introduced by the Born-Oppenheimer approximation, the electronic Schrödinger equation is still too complex to solve for systems of chemical interest. In the independent-particle approximation, the total wavefunction Ψ_{H} can be approximated as a product of spin-orbital wavefunctions χ_i for each electron:

$$\Psi_{\text{H}}(x_1, x_2, \dots, x_N) = \chi_i(x_1)\chi_j(x_2) \dots \chi_k(x_N) \tag{2.6}$$

where x_N contains the spatial and spin coordinates of electron *N*. This expression is known as the Hartree product. However, the Hartree product is not antisymmetric with respect to the exchange of two electrons.

To satisfy the antisymmetry principle, Hartree-Fock (HF) theory, also referred to as self-consistent field (SCF) theory, represents the wavefunction as a Slater determinant of spin-orbitals as

$$\Psi_{\text{H}}(x_1, x_2, \dots, x_N) = \frac{1}{\sqrt{N!}} \begin{vmatrix} \chi_i(x_1) & \chi_j(x_1) & \cdots & \chi_k(x_1) \\ \chi_i(x_2) & \chi_j(x_2) & \cdots & \chi_k(x_2) \\ \vdots & \vdots & \ddots & \vdots \\ \chi_i(x_N) & \chi_j(x_N) & \dots & \chi_k(x_N) \end{vmatrix} \tag{2.7}$$

where the factor $1/\sqrt{N!}$ is a normalization factor. This ensures the indistinguishability of the electrons. Each spin-orbital can be considered as a product of its spatial part ψ_i and its spin part with spin either α or β as

$$\chi_i(x_N) = \begin{cases} \psi_i(r_N)\alpha(\omega) \\ \psi_i(r_N)\beta(\omega) \end{cases} \tag{2.8}$$

According to the variational principle, the expectation value of the Hamiltonian is

$$\langle \mathbf{H} \rangle = \frac{\langle \Psi | \mathbf{H} | \Psi \rangle}{\langle \Psi | \Psi \rangle} \geq E_0 \tag{2.9}$$

where $\langle \mathbf{H} \rangle = E_0$ only if Ψ is an eigenfunction of the Hamiltonian with eigenvalue E_0. Within these approximations, the electronic component of the HF energy can be expressed as

$$E_{\mathrm{HF}} = \sum_i^N \left(i\middle|\hat{h}\middle|i\right) + \frac{1}{2}\sum_i^N \sum_j^N (ii|jj) - (ij|ji) \tag{2.10}$$

where the one-electron integral

$$\left(i\middle|\hat{h}\middle|i\right) = \int \chi_i^*(x_1)\left[-\frac{1}{2}\nabla_i^2 - \sum_A^M \frac{Z_A}{r_{iA}}\right]\chi_i(x_1)dx_1 \tag{2.11}$$

corresponds to the kinetic energy and the electron-nuclear attraction for electron *i* and

$$(ii|jj) = \iint \chi_i^*(x_1)\chi_i(x_1)\frac{1}{r_{12}}\chi_j^*(x_2)\chi_j(x_2)dx_1dx_2 \tag{2.12}$$

$$(ij|ji) = \iint \chi_i^*(x_1)\chi_j(x_1)\frac{1}{r_{12}}\chi_j^*(x_2)\chi_i(x_2)dx_1dx_2 \tag{2.13}$$

correspond to the Coulomb and exchange integrals, respectively.

The HF orbitals are typically expressed as linear combinations of atom-centered Gaussian functions. The orbitals are optimized iteratively through a self-consistent approach to obtain the lowest possible energy within the constraints of orthonormal orbitals.

2.1.4. Semiempirical methods

HF scales as the fourth power of the number of basis functions because of the two-electron integrals. This computational cost can be further reduced by using semiempirical methods to reduce the number of integrals that must be computed. The first approximation to decrease the computational cost is to consider only the valence electrons explicitly. A minimal basis set is also used: hydrogen has one s-orbital basis function, and most other atoms have one s-orbital and three p-orbitals for a total of four basis functions.

The key approximation in semiempirical methods is the Zero Differential Overlap (ZDO) approximation. Within this approximation, it is assumed that basis functions centered on different atoms have no overlap. This greatly reduces the number of integrals that must be computed. All one-electron integrals with involving three centers are assumed to be zero, and all two-electron integrals involving three or four centers are set to zero. Because of these approximations, the remaining integrals must be parameterized to fit higher-level computational results or experimental results. The details of which integrals are neglected and which parameters are used define the semiempirical method. In particular, in the Intermediate Neglect of Differential Overlap (INDO) method, all two-center two-electron integrals except those of the Coulomb type are neglected. The simplified Hamiltonian can

be used as a starting point for calculations of the excited states, as will be discussed in the next section.

2.1.5. Post Hartree-Fock Methods

As HF is a mean-field theory, explicit electron correlation is neglected. This approximation limits the accuracy of many chemical properties that are of interest. To address these limitations, many methodologies know as post Hartree-Fock methods have been developed to correct for the effects of electron correlation. These methods include both perturbation theory based methods such as Møller-Plesset theory and methods that explicitly include multiple Slater determinants such as configuration interaction (CI) and coupled-cluster (CC). Because both CI and CC consider multiple Slater determinants, multiple eigenfunctions and eigenvalues can be computed to evaluate not only the ground-state properties but also the excited-state properties.

2.1.5.1. Configuration Interaction

In CI, the many-electron wavefunction is expanded as a sum of Slater determinants $|\Psi\rangle$. Here, $|\Psi_0\rangle$ represents the SCF wavefunction, $|\Psi_a^r\rangle$ represents a Slater determinant that is different from $|\Psi_0\rangle$ only by replacing the spin orbital χ_a with χ_r corresponding to a single-electron excitation, and $|\Psi_{ab}^{rs}\rangle$ and $|\Psi_{abc}^{rst}\rangle$ analogously represent doubly- and triply-excited Slater determinants, respectively. The total wavefunction $|\Phi_0\rangle$ of the ground state and the wavefunctions $|\Phi_N\rangle$ of the excited states can be expressed in a full configuration interaction (CI) picture as

$$|\Phi\rangle = c_0|\Psi_0\rangle + \sum_{a,r} c_a^r|\Psi_a^r\rangle + \sum_{\substack{a<b \\ r<s}} c_{ab}^{rs}|\Psi_{ab}^{rs}\rangle + \sum_{\substack{a<b<c \\ r<s<t}} c_{abc}^{rst}|\Psi_{abc}^{rst}\rangle + \cdots \qquad 2.14$$

$$= c_0|\Psi_0\rangle + c_S|\mathrm{S}\rangle + c_D|\mathrm{D}\rangle + c_T|\mathrm{T}\rangle + \cdots$$

where c_0, c_a^r, etc. are the CI coefficients for each Slater determinant in the total wavefunction. This equation can be condensed by using the CI coefficient c_S and the determinant $|\mathrm{S}\rangle$ to represent all single excitations and analogous terms to represent the multi-electron excitations.

According to Brillouin's theorem, the singly-excited determinants cannot interact directly with the SCF ground state, and so $\langle\Psi_0|\mathbf{H}|\mathrm{S}\rangle$=0. In addition, since there is no coupling between determinants that differ by more than two orbitals, $\langle\Psi_0|\mathbf{H}|\mathrm{T}\rangle$=0 and higher-order terms such as $\langle\mathrm{S}|\mathbf{H}|\mathrm{Q}\rangle$=0. The wavefunctions and corresponding energies can be obtained as the eigenvectors and eigenvalues of the CI matrix (shown only as the upper triangle)

$$\begin{bmatrix} \langle\Psi_0|\mathbf{H}|\Psi_0\rangle & 0 & \langle\Psi_0|\mathbf{H}|\mathrm{D}\rangle & 0 & \cdots \\ & \langle\mathrm{S}|\mathbf{H}|\mathrm{S}\rangle & \langle\mathrm{S}|\mathbf{H}|\mathrm{D}\rangle & \langle\mathrm{S}|\mathbf{H}|\mathrm{T}\rangle & \cdots \\ & & \langle\mathrm{D}|\mathbf{H}|\mathrm{D}\rangle & \langle\mathrm{D}|\mathbf{H}|\mathrm{T}\rangle & \cdots \\ & & & \langle\mathrm{T}|\mathbf{H}|\mathrm{T}\rangle & \cdots \\ & & & & \ddots \end{bmatrix} \qquad 2.15$$

The lowest eigenvalue of this matrix corresponds to the ground-state energy, and the higher eigenvalues correspond to the excited-state energies.

Since typical atomic and molecular systems have many occupied and unoccupied spin orbitals, the number of electron configurations in the full-CI picture (where all possible electron configurations are considered) can be extremely large. For systems with more than a handful of electrons, full CI is not practical, and the number of electron

configurations that are considered must be truncated; however, one disadvantage is that these truncated approaches are in general not size-consistent.

One truncation approach is to limit the excitations to those within a limited active space which includes only some of the occupied and unoccupied orbitals. The excitations can also be selected based on the number of excitations relative to the ground state or another reference determinant. When only single excitations (SCI) are considered, the SCF ground state cannot mix with any of the excited determinants according to Brillouin's theorem. Thus, a CI calculation provides the SCF ground state and a series of excited states composed of linear combinations of single excitations. Multi-electron excitations can be incorporated through various approaches. Both single and double excitations from the SCF ground state can be considered in an SDCI approach. Alternatively, higher-lying excitations can be selected using a multi-reference determinant (MRDCI) approach, where several reference determinants are selected and single (or higher) excitations are performed relative to each reference determinant.

2.1.5.2. Coupled Cluster Methods

To compute the electron correlation in a size-consistent manner, the coefficients of the higher-order excitations can be expressed in terms of the coefficients of lower-order excitations. In the coupled-cluster approximation, the coefficient of a quadruple excitation can be approximated as a product of the two component double excitations:

$$c_{abcd}^{rstu} \approx c_{ab}^{rs} c_{cd}^{tu} \qquad 2.16$$

To utilize this approximation, the wavefunction can be expressed in cluster form using the exponential ansatz as

$$|\Phi^{CC}\rangle = e^{\hat{T}}|\Psi_0\rangle \tag{2.17}$$

where the exponential can be expressed in terms of a Taylor series expansion as

$$|\Phi^{CC}\rangle = \left(1 + \hat{T} + \frac{\hat{T}^2}{2!} + \frac{\hat{T}^3}{3!} + \cdots\right)|\Psi_0\rangle \tag{2.18}$$

In this expression, $\hat{T}$ is the excitation operator

$$\hat{T} = \hat{T}_1 + \hat{T}_2 + \hat{T}_3 + \cdots \tag{2.19}$$

$$\hat{T}_1|\Psi_0\rangle = \sum_{a,r} t_a^r \Psi_a^r$$

$$\hat{T}_2|\Psi_0\rangle = \sum_{\substack{r>s \\ a>b}} t_{ab}^{rs} \Psi_{ab}^{rs}$$

where $\hat{T}_1$ is the single-excitation operator giving coefficients t_a^r for the singly-excited determinants and the higher-order excitations are similarly defined. Because the cluster expansion of the wavefunction includes the higher-order terms $\hat{T}^2$, $\hat{T}^3$, etc., this allows for size-consistency.

The energy of the CC wavefunction can be written as

$$E_{\mathrm{CC}} = \langle\Psi_0|He^{\hat{T}}|\Psi_0\rangle \tag{2.20}$$

Because the Hamiltonian contains only one-electron and two-electron operators, the ground-state energy depends only on the coefficients of the single and double excitations.

To maintain a reasonable computational cost, the excitation operator $\hat{T}$ is typically truncated. In CCSD, only single and double excitations are considered; in CCSDT, single, double, and triple excitations are considered. CC2 is a relatively new computational method derived from CCSD where the double excitations are treated perturbatively only to first order.[5]

2.1.6. Density Functional Theory

One alternative approach to Hartree-Fock based methods is Density Functional Theory (DFT), based on the proof by Hohenberg and Kohn[6] that the ground-state electronic energy depends only on the electron density. This effectively simplifies the full wavefunction with 3*N* spatial variables to an electron density with only three spatial variables, which allows for consideration of large systems that are not practical to evaluate using expensive post-HF methods.

2.1.6.1. Hohenberg-Kohn Theorems

DFT is based on the two Hohenberg-Kohn theorems. The first is that the external potential $V_{ext}(r)$ is, within a constant, a unique functional of $\rho(r)$; thus, the ground-state energy is a unique functional of the electron density. Because $\rho(r)$ uniquely determines the Hamiltonian, it also uniquely determines all other molecular properties. Thus, the average value of any observable is a functional of the electron density:

$$\langle A \rangle = A[\rho(r)] \tag{2.21}$$

The total electronic energy of the system can be written as a functional of the electron density as

$$E_v[\rho] = T_v[\rho] + E_{eN}[\rho] + E_{ee}[\rho] \quad 2.22$$

where $T_v[\rho]$ is the kinetic energy, $E_{eN}[\rho]$ is the electron-nuclear electrostatic attraction, and $E_{ee}[\rho]$ is the electron-electron repulsion. The universal functional of Hohenberg and Kohn is a sum of the kinetic energy and electron-electron repulsion terms:

$$F_{HK}[\rho] = T_v[\rho] + E_{ee}[\rho] \quad 2.23$$

However, the exact form of this equation is not known and must be approximated. The electron-electron repulsion can be separated into the Coulomb integral $J[\rho]$, which is known exactly, and various non-classically defined terms including exchange, electron correlation, and self-interaction, which are not known exactly.

The second Hohenberg-Kohn theorem is nearly equivalent to the variational principle, stating that the electron density that minimizes the total functional energy is the true ground-state density ρ_0:

$$E_0 \leq E_v[\rho] = T_v[\rho] + E_{eN}[\rho] + E_{ee}[\rho] \quad 2.24$$

As in wavefunction-based methods, this allows the ground-state energy and electron density to be computed through a self-consistent process starting from a trial density.

2.1.6.2. Kohn-Sham Equations/Theorem

Because the kinetic energy is poorly represented by orbital-free DFT, the practical application of orbital-free DFT to chemical systems has been limited. This limitation has been addressed through the introduction of orbitals by Kohn and Sham.[7] In the Kohn-Sham model, the problem of interacting electrons in an external potential is simplified to

a system of non-interacting electrons in an effective potential. The kinetic energy is thus split into two terms: an orbital-based term that can be computed exactly, and a small correction term. The exact kinetic energy of the non-interacting system is

$$T_s = -\frac{1}{2}\sum_{i}^{N}\langle\varphi_i|\nabla^2|\varphi_i\rangle \tag{2.25}$$

The approximate density of the system can be written as a sum of the electron densities of the occupied one-electron orbitals as

$$\rho_{\text{approx}} = \sum_{i}^{N}|\varphi_i|^2 \tag{2.26}$$

where it is assumed that all molecular orbitals have integer occupation. The difference between the kinetic energy computed using the approximate density and that of the exact density is referred to as the kinetic correlation energy.

Using this kinetic energy, the total energy of the system can be written as

$$E_v[\rho] = T_s[\rho] + E_{eN}[\rho] + J[\rho] + E_{xc}[\rho] \tag{2.27}$$

where the exchange-correlation term contains all of the parts of the Hamiltonian that cannot be computed exactly:

$$E_{xc}[\rho] = (T[\rho] - T_s[\rho]) + (E_{ee}[\rho] - J[\rho]) \tag{2.28}$$

The first term in this expression is the kinetic correlation energy, and the second incorporates both the potential correlation energy and the exchange energy. The accuracy of a DFT functional depends on the accuracy of the selected exchange-correlation functional for the system and properties of interest.

2.1.6.3. Approximate Exchange-Correlation Functionals

Although Kohn-Sham DFT is in principle exact, practical applications require that the exchange-correlation energy be approximated. Unlike in wavefunction methods, there is not a systematic hierarchy of functionals that can be used to approach the exact result. However, a "Jacob's ladder" hierarchy of functionals has been used to categorize the many available functionals and provide broad guidelines about what functionals may in general provide more accurate results.

Local Density Approximation

In the Local Density Approximation (LDA), the local electron density at each point is treated as a uniform electron gas, under the assumption that the electron density varies slowly over space. The exchange energy is given by the Dirac formula

$$E_x^{LDA}[\rho] = -C_x \int \rho^{4/3}(\vec{r}) d\vec{r} \qquad 2.29$$

where $C_x = 3/4\sqrt[3]{3/\pi}$. The analytical form of the correlation energy is not known, so expressions for the correlation energy are derived from quantum Monte Carlo simulations for the uniform electron gas.

In molecular systems, the accuracy of this approach is limited because the electron density varies significantly over space. In particular, LDA approaches tend to underestimate the exchange energy and overestimate the correlation energy and bond strengths.

Generalized Gradient Approximation

To improve upon LDA, the inhomogeneity of the electron density over space in molecular systems must be considered. One approach is to include information about the gradient of the electron density $\nabla\rho_\sigma(\vec{r})$; approaches using this information are called Generalized Gradient Approximation (GGA) functionals. In these approaches, the total exchange and correlation energies are typically computed by adding a term that depends on the gradient to the LDA exchange and correlation energies, respectively. The total GGA functional is typically constructed by adding an exchange functional to a correlation functional.

Hybrid Functionals

The exchange energy is typically significantly larger than the correlation energy, so an accurate representation of the exchange energy is particularly important to compute an accurate total energy. DFT functionals suffer from self-interaction error (SIE), since the density of a single electron causes a non-zero Coulomb repulsion $J[\rho]$; in contrast, Hartree-Fock exchange is exact in the limit of non-interacting electrons. Thus, the exchange energy can be improved by mixing some fraction of Hartree-Fock exchange into the DFT exchange-correlation functional:

$$E_{xc}^{hybrid} = aE_x^{HF} + (1-a)E_x^{KS} + E_c^{KS} \qquad 2.30$$

Many hybrid functionals have been developed using this general approach, the most popular being B3LYP.[8,9] This approach generally improves the accuracy of the molecular

properties; however, the fraction of HF exchange that must be added to compute accurate results depends on the system and the properties of interest.

Long-Range Corrected Functionals

Although hybrid functionals can decrease SIE, hybrid functionals still do not have the correct asymptotic behavior for long-range exchange interactions. Hartree-Fock exchange has the correct long-range asymptotic behavior and no SIE at long-range, whereas the exchange in GGA functionals is more accurate for describing short-range interactions. To address these limitations, long-range corrected (LRC) functionals have recently been developed. In these functionals, the Coulomb operator is split into short-range and long-range components.[10,11] This separation is typically done using an error function

$$\frac{1}{r} = \frac{erfc(\omega)}{r} + \frac{erf(\omega)}{r} \qquad 2.31$$

where ω is a range-separation parameter that controls the distance at which the transition from DFT to HF exchange occurs. The general form of an LRC functional is

$$E_{xc}^{LRC} = E_x^{SR-KS} + E_x^{SR-HF} + E_x^{LR-HF} + E_c^{KS} \qquad 2.32$$

Much work has gone into determining appropriate range-separation parameters for a variety of molecular systems.[12,13]

2.2. Atomistic Simulations

For systems containing thousands of atoms or more, it is not computationally feasible to use even the most inexpensive electronic-structure methods. In atomistic molecular mechanics (MM) and molecular dynamics (MD) simulations, the electronic energy is instead expressed as a function of the nuclear positions using parameters derived from

experimental or quantum-mechanical results. By neglecting quantum-mechanical effects, the dynamics of the system can be treated using classical mechanics.

2.2.1. Force Fields

The force field energy is expressed as a series of terms describing the bonded (stretch, bend, and torsion) and non-bonded (Van der Waals and electrostatic) interactions between the atoms:

$$E = E_{str} + E_{bend} + E_{tors} + E_{vdw} + E_{el} \tag{2.33}$$

2.2.1.1. Bonded Interactions

The stretch energy expresses the energy for bonded pairs of atoms A-B as a function of bond length. For reasons of computational expense, a harmonic potential is typically used; this potential is usually sufficient to describe the potential at bond lengths R^{AB} near the energetic minimum.

$$E_{str}(R^{AB}) = k^{AB}(R^{AB} - R_0^{AB})^2 \tag{2.34}$$

Parameters for the equilibrium bond length R_0^{AB} and the force constant k^{AB} must be determined from experimental data or quantum-chemical calculations.

The bend energy expresses the energy to bend the angle between a set of three bonded atoms A-B-C. As with the stretch energy, a harmonic approximation is typically used.

$$E_{bend}(\theta^{ABC}) = k^{ABC}(\theta^{ABC} - \theta_0^{ABC})^2 \tag{2.35}$$

The parameters for the equilibrium angle θ_0^{ABC} and the force constant k^{ABC} must similarly be determined.

The torsional energy describes the energy associated with rotation about bond B-C in a bonded set of four atoms A-B-C-D. As the energetic barrier for torsion is often small and the molecule may rotate through a large range of torsion angles at moderate temperatures, the torsional potential must be periodic. The torsional potential is typically written as a sum of cosine functions. This sum maybe formulated in several ways; in the Ryckaert-Bellemans form, the torsional energy is expressed as:

$$E_{tors}(\omega^{ABCD}) = \sum_n V_n^{ABCD}(\cos\omega^{ABCD})^n \qquad 2.36$$

where the coefficients V_n^{ABCD} must be determined.

2.2.1.2. Non-Bonded Interactions

Intermolecular interactions and intramolecular interactions between atoms far apart in the molecule are expressed in terms of van der Waals and electrostatic interactions. The van der Waals term includes exchange-repulsion at short interatomic distances and weak attraction due to dispersion at intermediate distances. This term is typically expressed using a Lennard-Jones potential:

$$E_{vdw}(R^{AB}) = \varepsilon^{AB}\left[\left(\frac{R_0^{AB}}{R^{AB}}\right)^{12} - 2\left(\frac{R_0^{AB}}{R^{AB}}\right)^{6}\right] \qquad 2.37$$

where the energy of the dispersion interaction has an R^{-6} dependence and that of the repulsive part has an R^{-12} dependence. R_0^{AB} is the minimum-energy distance, and ε^{AB} is

the depth of the potential well. The pairwise terms are usually expressed in terms of the atomic van der Waals radii and interaction energies as

$$R_0^{AB} = R_0^A + R_0^B \qquad 2.38$$

$$\varepsilon^{AB} = \sqrt{\varepsilon^A \varepsilon^B}$$

The electrostatic interactions, including charge-charge, charge-dipole, dipole-dipole and higher multipole interactions, are typically computed by treating the molecular charge distribution as point charges centered at the atoms. The interactions between the point charges are treated using the Coulomb potential:

$$E_{el}(R^{AB}) = \frac{Q^A Q^B}{\varepsilon R^{AB}} \qquad 2.39$$

where the atomic charges Q^A and Q^B can be determined from quantum-chemical calculations or written in terms of standard atomic charges for the given atom types, and ε is the dielectric constant.

2.2.2. Molecular Dynamics

2.2.2.1. Equation of Motion

Since the atomic nuclei are reasonably heavy, their motion can be treated classically using Newton's second equation, **F** = *m***a**. This equation can be written as a differential equation in terms of the atomic coordinates as

$$-\frac{dV}{d\mathbf{r}} = m\frac{d^2\mathbf{r}}{dt^2} \qquad 2.40$$

where *V* is the potential energy of the system and **r** contains all atomic coordinates.

To simulate a trajectory over time, Newton's equations of motion must be integrated over time. The atomic positions $\mathbf{r}_{i+1}$ at time step i+1 can in general be written in terms of the atomic positions $\mathbf{r}_i$, velocities $\mathbf{v}_i$, and accelerations $\mathbf{a}_i$ at time step i in terms of a Taylor expansion

$$\mathbf{r}_{i+1} = \mathbf{r}_i + \frac{\partial r}{\partial t}(\Delta t) + \frac{1}{2}\frac{\partial^2 r}{\partial t^2}(\Delta t)^2 + \cdots \qquad 2.41$$

$$= \mathbf{r}_i + \mathbf{v}_i(\Delta t) + \frac{1}{2}\mathbf{a}_i(\Delta t)^2 + \cdots$$

where Δt is the time step between steps i and i+1.

The most common integration algorithm is the Verlet algorithm, where the positions of the particles at time $(t + \Delta t)$ are computed in terms of the positions and accelerations at time t and the positions at time $(t - \Delta t)$:

$$\mathbf{r}_{i+1} = 2\mathbf{r}_i - \mathbf{r}_{i-1} + \mathbf{a}_i(\Delta t)^2 \qquad 2.42$$

In this algorithm, the velocities are not explicitly used to compute the new atomic positions; however, the velocities can be approximated as:

$$\mathbf{v}_i = \frac{\mathbf{r}_{i+1} - \mathbf{r}_{i-1}}{2\Delta t} \qquad 2.43$$

Time steps on the order of 1 fs are typically needed to obtain sufficient accuracy, as this time is roughly an order of magnitude faster than the fastest molecular vibrations.

2.2.2.2. Ensembles

An ensemble is a collection of a large number of microscopic states that describe all possible states of a system. A macroscopic experimental observable corresponds to an average over these microscopic states. The microcanonical ensemble (NVE),

corresponding to an isolated system, contains all microscopic states with constant number of atoms (N), volume (V), and energy (E). The isobaric-isothermal (NPT) ensemble is much more representative of typical laboratory conditions, as the number of atoms, pressure (P), and temperature (T) are held constant by coupling the system to external heat and pressure baths.

To compute macroscopic observables, it is necessary to average over the microscopic states in a given ensemble. According to the ergodic hypothesis, given infinite time, a system will pass through all possible microscopic states. Thus, by averaging over a sufficiently long time, MD simulations can be used to compute macroscopic observables that correspond to experimentally relevant quantities.

2.3. Software

The computational methods used in this dissertation were implemented in the following software: Gaussian09 (Rev B.01),[14] QChem 4.0,[15] Turbomole V6.1,[16] ZINDO, and GROMACS 4.5.4.[17]

2.4. References

(1) Szabo, A. S. O. N. S. *Modern quantum chemistry : introduction to advanced electronic structure theory*; 1st , Rev. ed.; McGraw-Hill: New York, 1989.

(2) Jensen, F. *Introduction to computational chemistry*; Hoboken, NJ, 2007.

(3) Frenkel, D. S. B. *Understanding molecular simulation : from algorithms to applications*; 2nd ed.; Academic Press: San Diego, 2002.

(4) Koch, W. H. M. C. *A chemist's guide to density functional theory*; New York, 2001.

(5) Christiansen, O.; Koch, H.; Jorgensen, P. *Chem. Phys. Lett.* **1995**, *243*, 409.

(6) Hohenberg, P.; Kohn, W. *Phys. Rev. B* **1964**, *136*, B864.

(7) Kohn, W.; Sham, L. J. *Phys. Rev.* **1965**, *140*, 1133.

(8) Lee, C. T.; Yang, W. T.; Parr, R. G. *Phys. Rev. B* **1988**, *37*, 785.

(9) Becke, A. D. *J. Chem. Phys.* **1993**, *98*, 5648.

(10) Gill, P. M. W.; Adamson, R. D.; Pople, J. A. *Mol. Phys.* **1996**, *88*, 1005.

(11) Savin, A.; Flad, H. J. *Int. J. Quantum Chem.* **1995**, *56*, 327.

(12) Baer, R.; Livshits, E.; Salzner, U. In *Annual Review of Physical Chemistry, Vol 61*; Leone, S. R., Cremer, P. S., Groves, J. T., Johnson, M. A., Richmond, G., Eds. 2010; Vol. 61, p 85.

(13) Refaely-Abramson, S.; Baer, R.; Kronik, L. *Phys. Rev. B* **2011**, *84*.

(14) Gaussian 09, Revision B.01, M. J. Frisch, G. W. Trucks, H. B. Schlegel, G. E. Scuseria, M. A. Robb, J. R. Cheeseman, G. Scalmani, V. Barone, B. Mennucci, G. A. Petersson, H. Nakatsuji, M. Caricato, X. Li, H. P. Hratchian, A. F. Izmaylov, J. Bloino, G. Zheng, J. L. Sonnenberg, M. Hada, M. Ehara, K. Toyota, R. Fukuda, J. Hasegawa, M. Ishida, T. Nakajima, Y. Honda, O. Kitao, H. Nakai, T. Vreven, J. A. Montgomery, Jr., J. E. Peralta, F. Ogliaro, M. Bearpark, J. J. Heyd, E. Brothers, K. N. Kudin, V. N. Staroverov, T. Keith, R. Kobayashi, J. Normand, K. Raghavachari, A. Rendell, J. C. Burant, S. S. Iyengar, J. Tomasi, M. Cossi, N. Rega, J. M. Millam, M. Klene, J. E. Knox, J. B. Cross, V. Bakken, C. Adamo, J. Jaramillo, R. Gomperts, R. E. Stratmann, O. Yazyev, A. J. Austin, R. Cammi, C. Pomelli, J. W. Ochterski, R. L. Martin, K. Morokuma, V. G. Zakrzewski, G. A. Voth, P. Salvador, J. J. Dannenberg, S. Dapprich, A. D. Daniels, O. Farkas, J. B. Foresman, J. V. Ortiz, J. Cioslowski, and D. J. Fox, Gaussian, Inc., Wallingford CT, 2010.

(15) Yihan Shao, Laszlo Fusti-Molnar, Yousung Jung, Jurg Kussmann, Christian Ochsenfeld, Shawn T. Brown, Andrew T.B. Gilbert, Lyudmila V. Slipchenko, Sergey V. Levchenko, Darragh P. O'Neill, Robert A. DiStasio Jr., Rohini C. Lochan, Tao Wang, Gregory J.O. Beran, Nicholas A. Besley, John M. Herbert, Ching Yeh Lin, Troy Van Voorhis, Siu Hung Chien, Alex Sodt, Ryan P. Steele, Vitaly A. Rassolov, Paul E. Maslen, Prakashan P. Korambath, Ross D. Adamson, Brian Austin, Jon Baker, Edward F. C. Byrd, Holger Daschel, Robert J. Doerksen, Andreas Dreuw, Barry D. Dunietz, Anthony D. Dutoi, Thomas R. Furlani, Steven R. Gwaltney, Andreas Heyden, So Hirata, Chao-Ping Hsu, Gary Kedziora, Rustam Z. Khaliullin, Phil Klunzinger, Aaron M. Lee, Michael S. Lee, WanZhen Liang, Itay Lotan, Nikhil Nair, Baron Peters, Emil I. Proynov, Piotr A. Pieniazek, Young Min Rhee, Jim Ritchie, Edina Rosta, C. David Sherrill, Andrew C. Simmonett, Joseph E. Subotnik, H. Lee Woodcock III, Weimin Zhang, Alexis T. Bell, Arup K. Chakraborty, Daniel M. Chipman, Frerich J. Keil, Arieh Warshel, Warren J. Hehre, Henry F. Schaefer III, Jing Kong, Anna I. Krylov, Peter M.W. Gill and Martin Head-Gordon. Phys. Chem. Chem. Phys., 8, 3172 (2006).

(16) TURBOMOLE V6.1 2009, a development of University of Karlsruhe and Forschungszentrum Karlsruhe GmbH, 1989-2007, TURBOMOLE GmbH, since 2007; available from http://www.turbomole.com.

(17) Written by Emile Apol, Rossen Apostolov, Herman J.C. Berendsen, Aldert van Buuren, Pär Bjelkmar, Rudi van Drunen, Anton Feenstra, Gerrit Groenhof, Peter Kasson, Per Larsson, Pieter Meulenhoff, Teemu Murtola, Szilard Pall, Sander Pronk, Roland Schulz, Michael Shirts, Alfons Sijbers, Peter Tieleman, Berk Hess, David van der Spoel, and Erik Lindahl. Copyright (c) 1991-2000, University of Groningen, The Netherlands. Copyright (c) 2001-2010, The GROMACS development team at Uppsala University & The Royal Institute of Technology, Sweden.

CHAPTER 3

IMPACT OF THE NATURE OF THE EXCITED-STATE TRANSITION DIPOLE MOMENTS ON THE THIRD-ORDER NONLINEAR OPTICAL RESPONSE OF POLYMETHINE DYES FOR ALL-OPTICAL SWITCHING APPLICATIONS

3.1. Introduction

As discussed in the Introduction, polymethines inherently have large negative Re(γ) values, whereas polyenes have positive Re(γ) values.[1,2] This can be understood in terms of the first several excited-state energies, state dipole moments, and transition dipole moments via the SOS expressions (Equations 1.14 and 1.17). The large negative Re(γ) characteristic of polymethines originates from the inherently large transition dipole moment μ_{ge} between the ground- and first-excited states,[2] which is raised to the fourth power in the **N** term and therefore dominates the SOS expression. While many polymethines studied to date have large |Re(γ)|, they also tend to have significant TPA that reduces the figure-of-merit.[3,4] This TPA-dependence arises primarily from the **T** term, which involves a sum over transitions from the first excited state to higher-lying TPA-allowed states, in particular the 2A state *e'*. Hence, when considering the design of molecular structures with **N** >> **T**, the contribution from the second excited state (*e.g.*, $E_{ge'}$ and $\mu_{ee'}$) becomes the most significant characteristic to evaluate.

While it is generally found that the ratio of $E_{ge'}$ to E_{ge} is around 1.7,[5] the relationship between polymethine chemical structure and $\mu_{ee'}$ is not well understood. Although $\mu_{ee'}$ is

small enough in some polymethines that the role of the **T** term in Re(γ) is negligible,[3,5,6] in other structures $\mu_{ee'}$ is comparable in magnitude to μ_{ge}.[7] Thus, it is important to better understand the relationship between chemical structure and $\mu_{ee'}$. Since the **T** term in the SOS expression for Re(γ) is positive,[8] a small $\mu_{ee'}$ aids in maximizing |Re(γ)|; in addition, since the **T** term plays the most significant role in determining the Im(γ) magnitude, a small $\mu_{ee'}$ leads to a small TPA cross-section in state *e'*, which helps keep Im(γ) small. We note, in contrast, that the **T** term for polyenes is typically larger than the **N** term as the polyenes have many low-lying TPA states, resulting in a positive, smaller Re(γ).[2]

Achieving detailed insight into the structure-property relationships that affect $\mu_{ee'}$ is thus critical to the design of chromophores with improved NLO properties for AOS.[9] Here, we use electronic-structure methods to examine $\mu_{ee'}$ for a series of streptocyanines (*i.e.*, polymethines with amino end substituents) and polyenes (Figure 3.1) that have long been used as model systems in computational and experimental studies of NLO response.[2,10-13] The molecular structures are varied in terms of the (i) conjugated path length and (ii) donor/acceptor substitution in the center of the molecular unit to evaluate effects common to the design of molecules for NLO response. We find that a critical parameter determining the magnitude of $\mu_{ee'}$ is the energetic spacing among the first several frontier molecular orbitals, in particular the energetic gaps between the HOMO-1 and HOMO levels and the LUMO and LUMO+1 levels. As will be shown, the unique nodal patterns of the MOs in polymethines make donor/acceptor substitution in the center of the molecular unit a straightforward way of tuning the MO spacing. The insights gleaned in

our theoretical study of how the substituents impact the structure-property relationships are applicable to a much broader range of structural modifications to the polymethines.

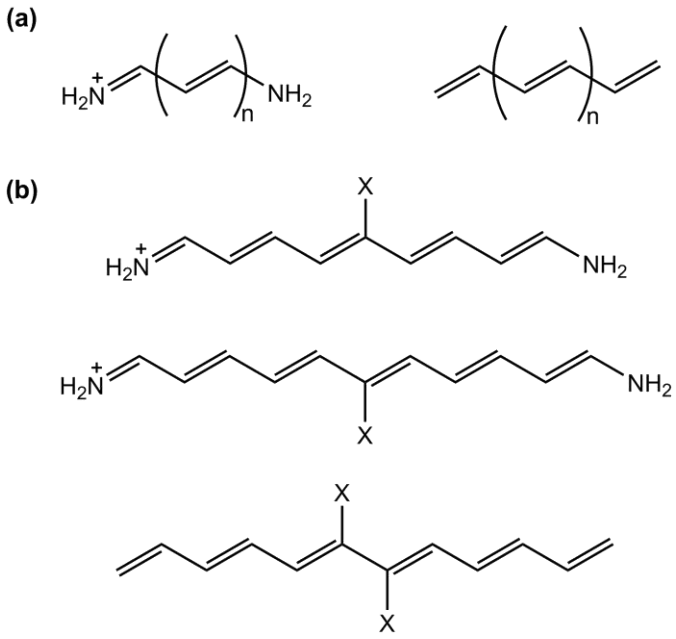

Figure 3.1. Chemical structures of (a) general streptocyanines and polyenes and (b) donor- or acceptor-substituted streptocyanines and polyenes (X = $-OCH_3$, $-CF_3$).

3.2. Methodology

We first note that an important aspect from our calculations is to determine how the transition density changes as a function of molecular length and substitution. Just as a state dipole moment can be considered as a sum of contributions from the charge density associated with each atom, a transition dipole moment can be considered as a sum of contributions from the transition density at each atom, which is computed as the product of the wavefunctions of the initial and final states. In addition, since each wavefunction is a sum of contributions from the various electronic configurations, the transition dipole moment can be considered as a sum of contributions from each pair of initial and final

electronic configurations. Hence, the decomposition of the transition dipole moments into (i) atomic transition densities and (ii) contributions from the component electronic configurations via the molecular orbitals and configuration interaction (CI) coefficients[14] provides a valuable tool to examine molecular structure effects on $\mu_{ee'}$. This insight will be used to evaluate how common chemical modifications to polyenes and polymethines affect the NLO response. We note that the polymethines have very little geometric change upon excitation, as evidenced by the sharp absorption peaks with little vibronic structure in the experimental OPA and TPA spectra[5] and computed OPA spectra;[15,16] therefore, we have neglected vibronic effects and focused solely on the electronic components of the transition dipole moments.

The geometric structures of the polymethines and polyenes were optimized via density functional theory (DFT) with the ωB97X functional[17] and cc-pVDZ basis set[18] as implemented in the Gaussian 09 (Rev. B.01) suite of programs.[19] The excited-state properties were then evaluated using an SDCI approach with the INDO Hamiltonian;[2,14,20] this approach has previously provided excellent agreement with the experimental TPA properties of π-conjugated systems.[21,22] The SDCI active space included all single-electron excitations within the 20 highest-lying occupied molecular orbitals (MOs) and 20 lowest-lying unoccupied MOs and all double-electron excitations within the four highest-lying occupied MOs and four lowest-lying unoccupied MOs.[23]

The transition dipole moment $\mu_{ee'}$ between states *e* and *e'* is an off-diagonal matrix element of the dipole operator $\vec{\mu}$:

$$\mu_{ee'} = \left\langle \Psi_e \left| \vec{\mu} \right| \Psi_{e'} \right\rangle = \int \Psi_e^* e\vec{r}\, \Psi_{e'} d^3r = \int \rho_{e\to e'} e\vec{r}\, d^3r \qquad 3.1$$

where $\rho_{e\to e'}$ is the transition density between states e and e'. The total transition density and its decomposition into atomic and electronic-configuration components are determined using the CI coefficients and molecular orbitals from the INDO/SDCI calculations. The wave-functions $|\Psi_e\rangle$ and $|\Psi_{e'}\rangle$ from the INDO/SDCI calculations are expressed as a sum of electronic configurations $|\psi_j\rangle$ with coefficients c_j:

$$\left|\Psi_e\right\rangle = \sum_j c_j \left|\psi_j\right\rangle \qquad 3.2$$

The electronic configurations are spin-adapted so that the configurations are pure singlets:

No unpaired electrons: $\left|\psi_j\right\rangle = \left|\ldots n\bar{n}\, o\bar{o}\ldots\right\rangle$ 3.3

Two unpaired electrons: $\left|\psi_j\right\rangle = \frac{1}{\sqrt{2}}\left(\left|\ldots n\bar{n}\, o\bar{p}\ldots\right\rangle - \left|\ldots n\bar{n}\,\bar{o}p\ldots\right\rangle\right)$

Four unpaired electrons:

$$\left|\psi_j\right\rangle = \frac{1}{2}\left(\left|\ldots no\,\bar{p}\bar{q}\ldots\right\rangle - \left|\ldots n\bar{o}\,p\bar{q}\ldots\right\rangle - \left|\ldots \bar{n}\,o\bar{p}q\ldots\right\rangle + \left|\ldots \bar{n}\bar{o}pq\ \ldots\right\rangle\right)$$

$$\left|\psi_j\right\rangle = \frac{1}{2}\left(\left|\ldots n\bar{o}\,p\bar{q}\ldots\right\rangle - \left|\ldots n\bar{o}\bar{p}q\ldots\right\rangle - \left|\ldots \bar{n}op\ \bar{q}\ldots\right\rangle + \left|\ldots \bar{n}\,o\bar{p}q\ldots\right\rangle\right)$$

For each pair of electronic configurations, the transition dipole moment consists of an orbital component and a quantum prefactor. The orbital component can only be non-zero if the electronic configurations are no more than one orbital different. If the electronic configurations are one orbital different, the prefactor depends on both the number of

unpaired electrons in each configuration and the orbitals between which the electron moves. As an example, we show below the calculation of the quantum prefactor for the $|\mathrm{H} \rightarrow \mathrm{L}\rangle \rightarrow |\mathrm{H}, \mathrm{H} \rightarrow \mathrm{L}, \mathrm{L}\rangle$ transition:

$$\begin{aligned}
\left\langle \mathrm{H} \rightarrow \mathrm{L} \left| e\vec{r} \right| \mathrm{H}, \mathrm{H} \rightarrow \mathrm{L}, \mathrm{L} \right\rangle &= \frac{1}{\sqrt{2}}\left(\left\langle \ldots \mathrm{H}\,\overline{\mathrm{L}} \ldots \right| - \left\langle \ldots \overline{\mathrm{H}}\,\mathrm{L} \ldots \right| e\vec{r} \left(\left| \ldots \mathrm{L}\,\overline{\mathrm{L}} \ldots \right\rangle \right)\right) \\
&= \frac{1}{\sqrt{2}}\left(\left\langle \ldots \mathrm{H}\,\overline{\mathrm{L}} \ldots \left| e\vec{r} \right| \ldots \mathrm{L}\,\overline{\mathrm{L}} \ldots \right\rangle\right) - \frac{1}{\sqrt{2}}\left(\left\langle \ldots \overline{\mathrm{H}}\,\mathrm{L} \ldots \left| e\vec{r} \right| \ldots \mathrm{L}\,\overline{\mathrm{L}} \ldots \right\rangle\right) \\
&= \frac{1}{\sqrt{2}}\left(\left\langle \ldots \mathrm{H}\,\overline{\mathrm{L}} \ldots \left| e\vec{r} \right| \ldots \mathrm{L}\,\overline{\mathrm{L}} \ldots \right\rangle\right) + \frac{1}{\sqrt{2}}\left(\left\langle \ldots \mathrm{L}\,\overline{\mathrm{H}} \ldots \left| e\vec{r} \right| \ldots \mathrm{L}\,\overline{\mathrm{L}} \ldots \right\rangle\right) \\
\text{Quantum prefactor} &= \frac{1}{\sqrt{2}}(1+1) = \sqrt{2}
\end{aligned} \tag{3.4}$$

The orbital component of each transition dipole moment is determined by considering each molecular orbital as a sum of atomic orbitals φ_i with coefficients a_{ij}:

$$\left|\psi_j\right\rangle = \sum_i a_{ij} \left|\varphi_i\right\rangle \tag{3.5}$$

and computed as a product of the two atomic orbital coefficients and the atomic positions $\vec{r}$ by assuming that the transition density between each pair of atomic orbitals is centered at the position of the atom and using the zero differential overlap approximation:

$$\begin{aligned}
\left\langle \psi_j \left| e\vec{r} \right| \psi_k \right\rangle &= \left(\sum_i a_{ij} \left\langle \varphi_i \right| \right) e\vec{r} \left(\sum_l a_{lk} \left| \varphi_l \right\rangle \right) \\
&= \sum_i \sum_l a_{ij} a_{lk} e\vec{r} \delta_{il} \\
&= \sum_i a_{ij} a_{lk} e\vec{r}
\end{aligned} \tag{3.6}$$

3.3. Results and Discussion

We first discuss how changes to the chemical structure influence $\mu_{ee'}$ by investigating the influence of the conjugated path length in streptocyanines and in polyenes; we then turn

to the impact of chemical substitution with electron-accepting and electron-donating moieties.

3.3.1. Influence of the conjugated path length: Streptocyanines

In the unsubstituted streptocyanine series (n = 1 – 5), the first excited state *e* is of B_2 symmetry and is dominated by the HOMO → LUMO (H → L) transition (CI contribution of 80-85%), as previously noted for polymethines.[2] The μ_{ge} value is large and increases with increasing molecular length (Table 3.1): as the HOMOs and LUMOs within the series extend over the full π system, lengthening the molecule allows the transition density to be large near both ends of the molecule, far from the molecular center. We note that the computed E_{ge} values fall within 0.2 eV of reported experimental absorption maxima for the longer streptocyanines, though E_{ge} is somewhat underestimated for the shortest cyanines; importantly, the μ_{ge} values are in reasonable agreement with the experimental oscillator strengths.[24,25]

Table 3.1. Excited-state energies (eV) and transition dipole moments (Debye) for the streptocyanines.

Molecular Length (n)	E_{ge}	$E_{ge'}$	μ_{ge}	$\mu_{ee'}$
1	2.94	4.83	7.83	1.80
2	2.40	4.21	11.05	1.75
3	2.18	3.51	13.70	2.33
4	1.98	3.07	16.08	2.84
5	1.86	2.77	18.36	3.26

The second excited state *e'*, on the other hand, is described by three electronic configurations: two single-electron excitations (H-1 → L and H → L+1) and one double-

electron excitation (H, H → L, L). Since this state has A_1 symmetry, the transition from *e* to *e'* is one-photon-allowed.[26] However, $\mu_{ee'}$ is significantly smaller than μ_{ge}.

To understand the relatively small magnitude of $\mu_{ee'}$, we first consider the atomic transition densities. As shown in Figure 3.2, the atomic transition densities composing $\mu_{ee'}$ are small, a result that, at first sight, might appear to suggest poor orbital overlap in the transition. However, this is not the case as all of the orbitals involved in the transition are π orbitals that extend across the molecular backbone (Figure 3.3).

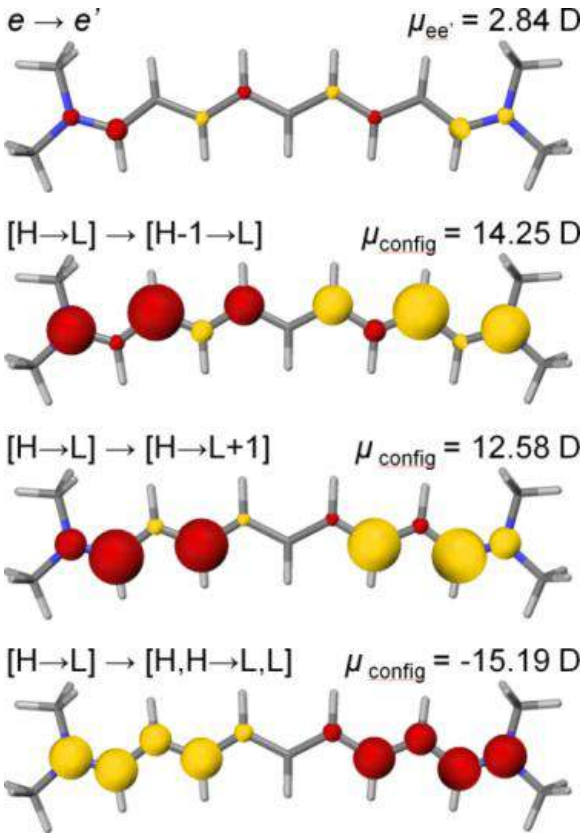

Figure 3.2. INDO/SDCI atomic transition densities and transition dipole moment $\mu_{ee'}$ as well as their major components for the (n=4) streptocyanine. The areas of the circles are proportional to the transition densities associated with each atom; the color represents the phase of the transition density.

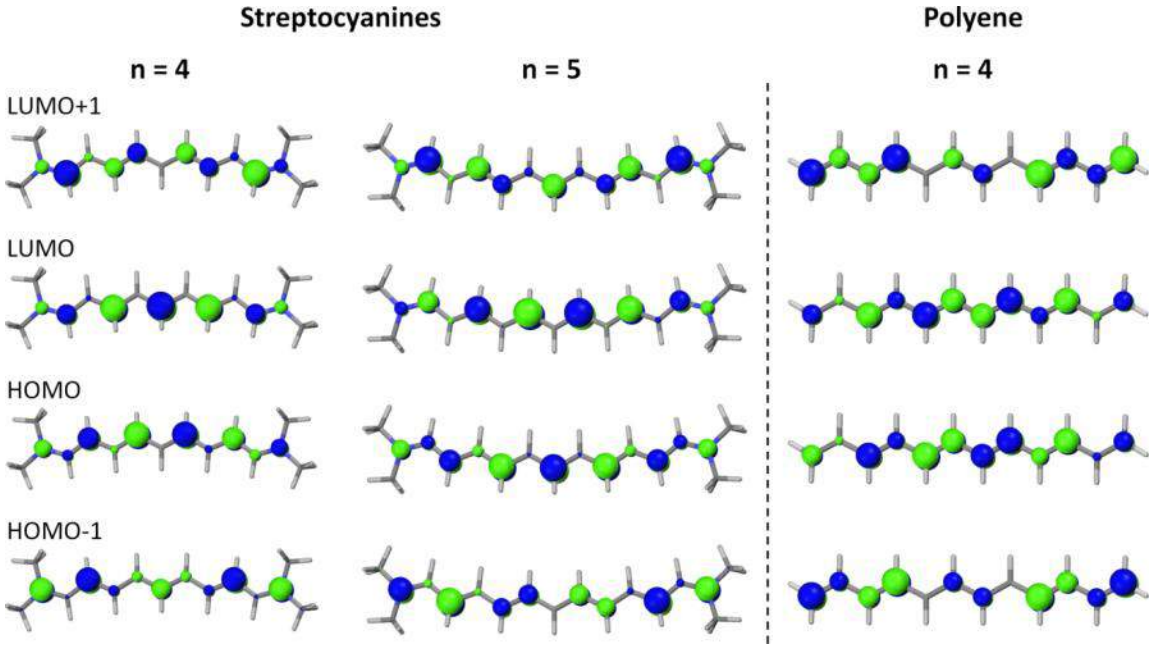

Figure 3.3. Frontier molecular orbitals of the streptocyanines and polyenes.

In fact, it is useful to separate $\mu_{ee'}$ into the components coming from each of the three pairs of electronic configurations involved in the $e \rightarrow e'$ transition to understand how they individually contribute to the total transition dipole moment. The decomposition strategy reveals that three terms dominate $\mu_{ee'}$ in the streptocyanines; they correspond to the transitions from [H → L] in state e to each of the three main electronic configurations describing e'. Interestingly, any pure transition involving one of these three pairs of configurations has a large transition dipole moment, comparable in magnitude to μ_{ge}, see Figure 3.2. The key result, however, is that the transitions to the two singly-excited configurations contribute to $\mu_{ee'}$ *with the same sign*, whereas the transition to the doubly-excited configuration has a contribution *of opposite sign*. This partial cancellation of terms leads to $\mu_{ee'}$ being significantly smaller than μ_{ge}.

Another important result is that, as the streptocyanine length increases, both the transition dipole moments of the component transitions comprising $\mu_{ee'}$ and the CI contributions for each configuration in *e'* change, see Figure 3.4, which determines to the dependence of $\mu_{ee'}$ on molecular length. The transition dipole moments for each of the three pure transitions increase as the polymethine length increases since the relevant molecular orbitals extend along the entire molecular π system. The energetic spacing of the frontier MOs (from the HOMO-1 level to the LUMO+1 level), shown in Figure 3.5, determines both the relative energies and CI contributions of the three component configurations in *e'*. For the shortest streptocyanines, the energetic gap between the LUMO and LUMO+1 levels is slightly smaller than the energetic gaps between the HOMO and LUMO levels and between the HOMO-1 and HOMO levels; thus, [H → L+1] configurations have slightly smaller energies than the other two configurations and therefore have the largest CI contributions to the second excited state. As the molecular length increases, the first several frontier MOs become more evenly spaced, and the energetic differences among the three configurations decrease. This leads to a decrease in the relative CI contribution of the [H → L+1] configuration and an increase in the contributions of the other configurations, particularly the doubly excited [H, H → L, L] configuration. We recall that for all molecular lengths, the contributions of the two singly excited configurations to $\mu_{ee'}$ have the same sign while the contribution of the doubly excited configuration has the opposite sign. Since the sum of the contributions of the single excitations decreases and the contribution of the double excitation increases, the change in the CI contributions results in significant cancellation and little increase in $\mu_{ee'}$ with increasing molecular length. We note that if the CI contributions were constant with increasing length and only

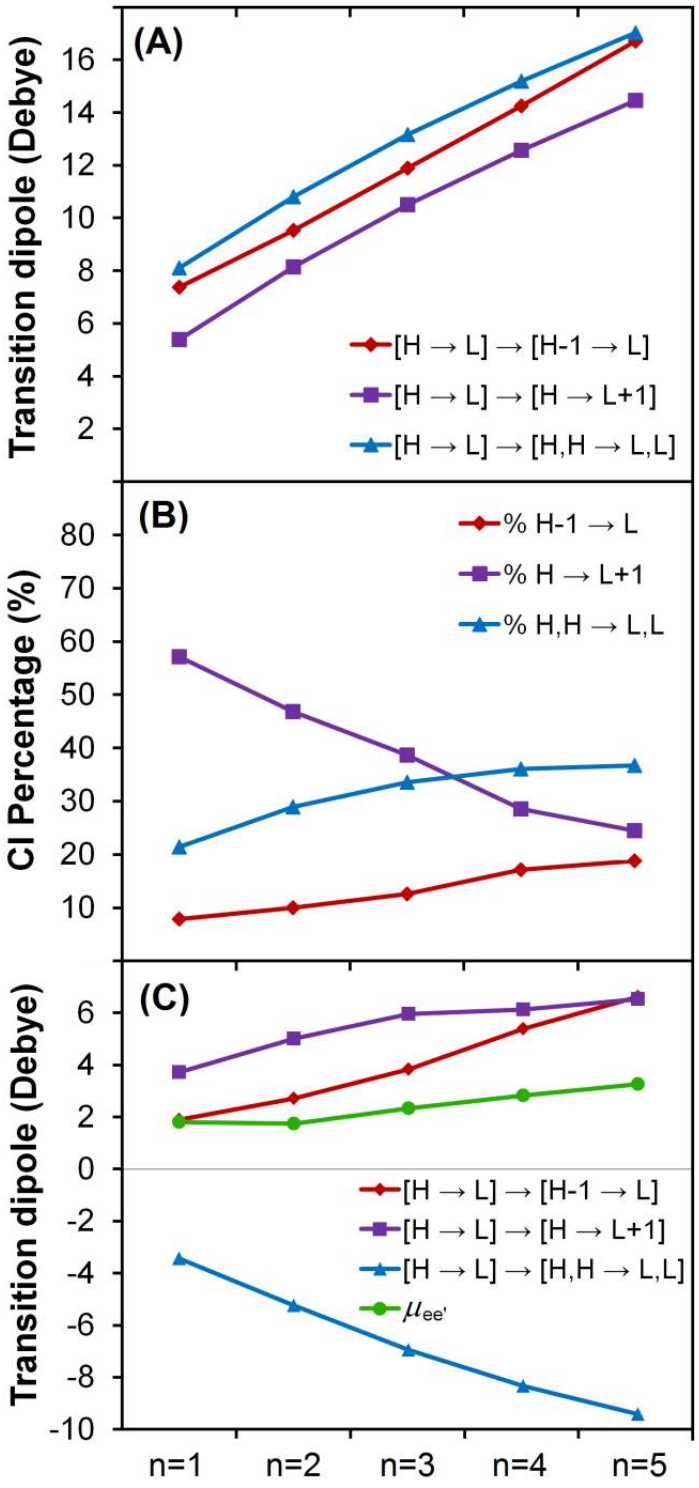

Figure 3.4. Evolution with streptocyanine length of: (A) the transition dipole moments of the pure component transitions; (B) the CI contributions of the primary excitations in *e'*; and (C) $\mu_{ee'}$ and its major components.

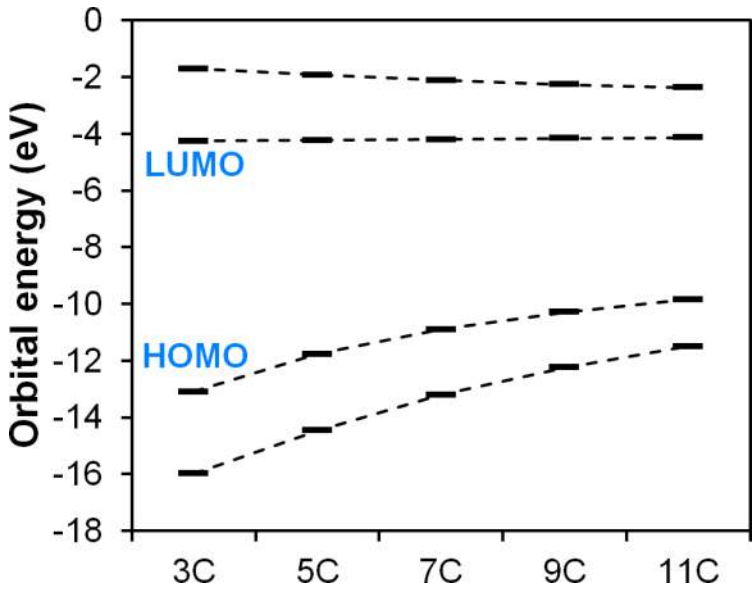

Figure 3.5. Energies of the streptocyanine frontier molecular orbitals at the INDO level.

the component transition dipole moments changed, $\mu_{ee'}$ would increase by about 4 D as the length increased from n=1 to n=5, instead of the actual value of 1.46 D.

3.3.2. Influence of the conjugated path length: Polyenes

As noted in the Introduction, the ordering of the first two excited states in long polyenes is reversed relative to polymethines: the $2A_g$ state *e'* is lower in energy than the $1B_u$ state *e*. Like in the streptocyanines, state *e* is primarily a H → L excitation and μ_{ge} is large (Table 3.2). State *e'* has significant contributions not only from the same three dominant excitations as in the streptocyanine state *e'* ([H-1 → L], [H → L+1], and [H, H → L, L]) but also has a substantial contribution (20-25%) from the double-electron excitation [H-1, H → L, L+1].[27] Since the transition dipole moment of a pure transition from [H → L] → [H-1, H → L, L+1] is substantially smaller than those of the other pure transitions, the contribution to $\mu_{ee'}$ is negligible and will not be considered further.

Table 3.2. Excited-state energies (eV) and transition dipole moments (Debye) for polyenes from hexatriene (n=1) to tetradecaheptaene (n=5). In these molecules, *e'* is the lowest excited state.

Molecular Length (n)	$E_{ge'}$	E_{ge}	$E_{ge''}$	$\mu_{ee'}$	μ_{ge}	$\mu_{ee''}$
1	4.69	6.11	8.70	2.30	6.00	12.3
2	4.49	5.48	7.86	3.93	7.57	14.4
3	4.46	5.19	7.38	3.48	9.10	18.1
4	4.18	4.94	6.76	4.39	10.6	20.3
5	4.00	4.44	6.30	5.39	11.8	22.3

In the polyenes, all three of the pure transitions with a significant contribution to $\mu_{ee'}$ have transition dipole moments that increase with length; however, the [H → L] → [H, H → L, L] transition dipole moment has a weaker dependence on molecular length than the other two transitions (Figure 3.6). This is due primarily to the spatial distribution of the orbitals involved in the transition. The polyene HOMO and LUMO levels are more localized near the center of the molecule (Figure 3.3), whereas the HOMO-1 and LUMO+1 levels have larger contributions at the polyene ends – these trends become even more pronounced as the molecular length increases. Since the spatial extents of the molecular orbitals involved in the [H → L] → [H, H → L, L] transition do not increase as rapidly as the molecular length, the corresponding transition dipole moment has an overall weaker length dependence; this is in contrast to the streptocyanines where the molecular orbitals have a more even distribution along the entire molecular backbone, leading to more similar length dependences among the pure transition dipole moments.

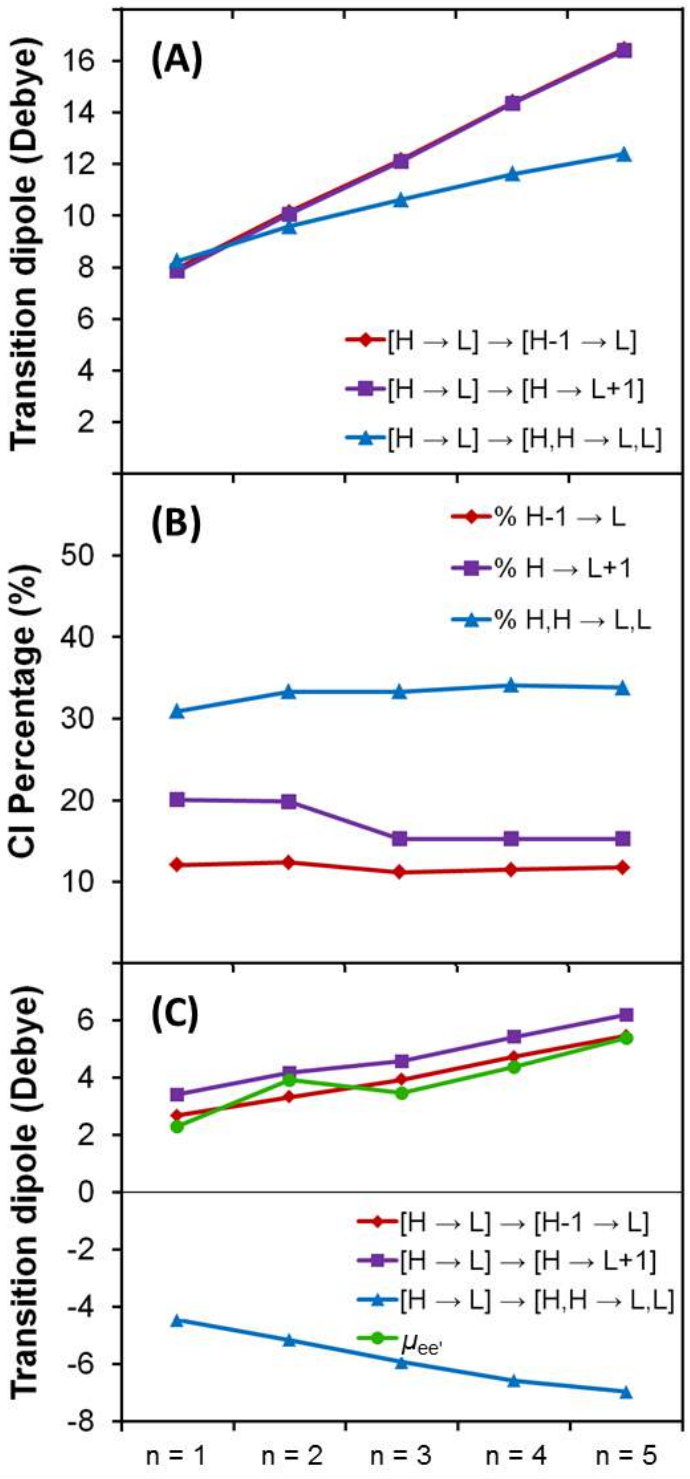

Figure 3.6. Evolution with polyene length of: (A) the transition dipole moments of the pure component transitions; (B) the CI contributions of the primary excitations in *e'*; and (C) $\mu_{ee'}$ and its major components.

As in the streptocyanines, the single excitations have contributions of the same sign to $\mu_{ee'}$, while the double excitation contributes with the opposite sign. In contrast, the CI contributions of the three electronic configurations contributing to the second excited states of the polyenes do not change significantly with length; as a result, $\mu_{ee'}$ increases linearly as the polyene length increases. Since $\mu_{ee'}$ is small in absolute value, the TPA cross-section of state *e'* is very small, in agreement with experimental observations.[28]

It is interesting to recall that computational[29-33] and experimental[28] evidence indicates that polyenes have a higher-lying mA_g state (*e"*) with a very significant TPA cross-section. The measured difference between the two-photon fluorescence activity of states *e'* and *e"* in octatetraene[28] implies that $\mu_{ee"}$ is on the order of three times the magnitude of $\mu_{ee'}$.[34] With the same computational strategy as that used to understand the magnitude of $\mu_{ee'}$, we find that state *e"* is primarily a linear combination of the same excitations that contribute to state *e'*; however, the sign of the double [H, H → L, L] excitation is reversed relative to that in state *e'*, so all three transitions contribute to $\mu_{ee"}$ in the same manner. Hence, we arrive at the critical conclusion that $\mu_{ee"}$ in polyenes is large due to this additive effect rather than cancellation among the major contributing terms seen for $\mu_{ee'}$.

3.3.3. Influence of electron-donating (methoxy) and -withdrawing (trifluoromethyl) substituents

The dependence of $\mu_{ee'}$ on the molecular orbital energies suggests design principles that can be used to modulate $\mu_{ee'}$ by controlling the energetic spacings among the first few

frontier molecular orbitals. If an electron-donating or electron-withdrawing substituent is added to the streptocyanine or polyene structures (here, a methoxy or a trifluoromethyl group), it primarily perturbs the energies of the molecular orbitals that have a significant weight of the wavefunction on the atom to which the substituent is bound. An important distinguishing feature between the polymethines and polyenes is that, in the case of the HOMO and LUMO levels, polymethines *can have nodes either on bonds or on carbon atoms*, whereas *nodes only exist on bonds* in polyenes. To address effects due to substitution with electron donors or acceptors while maintaining molecular symmetry, we have considered streptocyanines with one substituent on the central carbon atom and polyenes with substituents on the two central carbon atoms.

In polymethines, the π orbitals with an odd number of nodes have a node on the central carbon atom, while the remaining π orbitals have significant contribution to the wavefunction on the central carbon atom. In a streptocyanine containing *n* carbon-carbon double bonds, the HOMO has *n*+1 nodes (Figure 3.3); thus, the HOMO will have a node on the central carbon only if *n* is even. The LUMO+1 has the same *gerade* or *ungerade* symmetry as the HOMO, while the HOMO-1 and LUMO have the opposite symmetry. Due to this symmetry pattern, a substituent added to the central carbon of a streptocyanine where *n* is even primarily affects the HOMO-1 and LUMO orbital energies and has a much smaller effect on the HOMO and LUMO+1 energies; if *n* is instead odd, the pattern of which orbital energies are significantly affected is reversed.

The substituent has an important effect on the spacing of the polymethine frontier MOs. In particular, if *n* is even, an electron-withdrawing substituent stabilizes the HOMO-1 and LUMO, thereby narrowing the HOMO-LUMO gap but broadening the energetic spacing between the HOMO-1 and HOMO and between the LUMO and LUMO+1. This stabilizes the [H, H → L, L] excitation while having a smaller effect on the energies of the [H-1 → L] and [H → L+1] transitions. In this case, the coefficient of the double excitation in state *e'* increases, thereby decreasing $\mu_{ee'}$, see Figure 3.7. Conversely, if an electron-donating substituent is added in the same position, the HOMO-LUMO gap increases while the gaps between the HOMO-1 and HOMO and the LUMO and LUMO+1 decrease, thereby increasing $\mu_{ee'}$.

In contrast, if *n* is odd, a substituent on the central carbon atom primarily affects the HOMO and LUMO+1 energies, and the effect of the substituent on $\mu_{ee'}$ is reversed relative to the case where *n* is even. The stabilizing effect of the electron-withdrawing substituent in this case decreases the energetic spacing between the HOMO-1 and HOMO and the LUMO and LUMO+1, thus increasing $\mu_{ee'}$. The electron-donating substituent has the reverse effect and decreases $\mu_{ee'}$.

In the case of the polyenes, the frontier molecular orbitals have significant electron density on both central carbon atoms. Unlike in the polymethines, both electron-donating and electron-withdrawing substituents increase $\mu_{ee'}$ by 1-1.5 Debye and cause a slight reduction in the energetic spacing between the HOMO and HOMO-1. The contributions of the two single excitations to state *e'* increase with the addition of the substituents, with

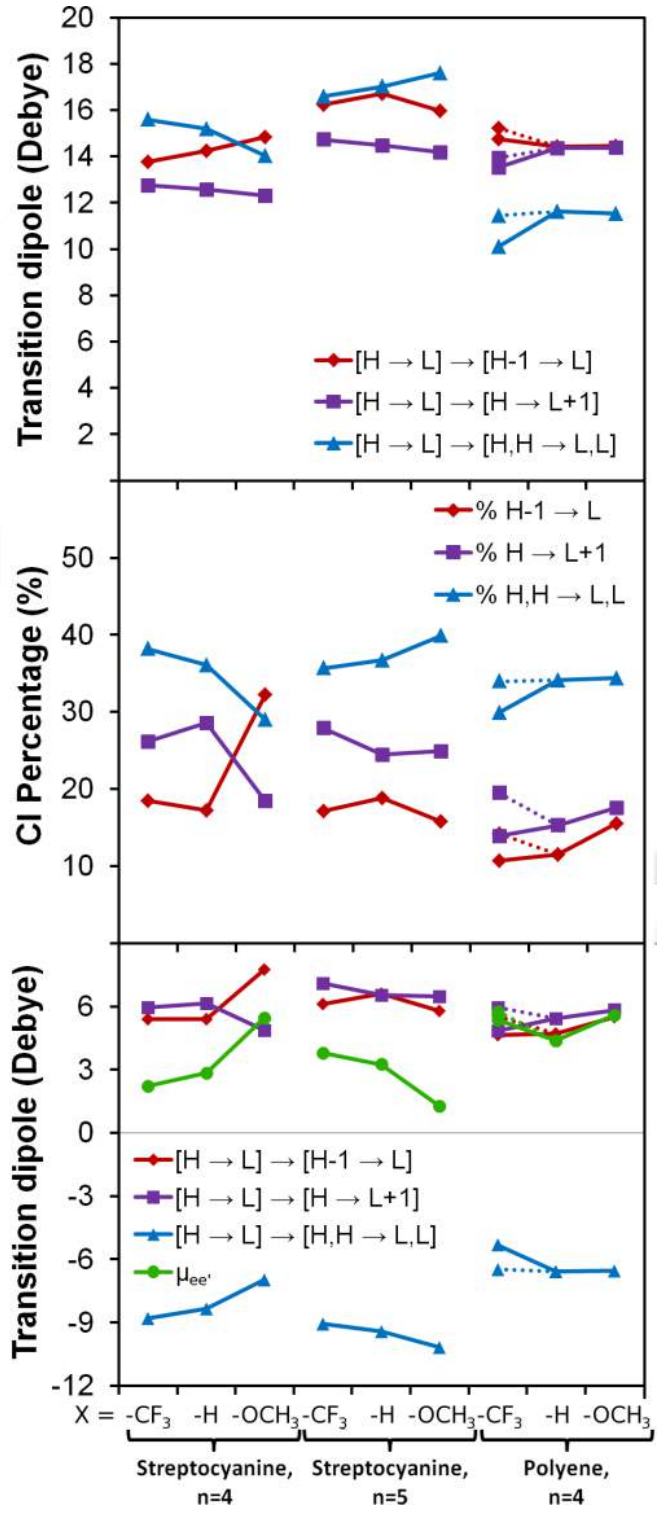

Figure 3.7. Evolution of $\mu_{ee'}$ and its major components with the addition of electron-donating and electron-withdrawing substituents to the (n=4 and n=5) streptocyanines and (n=4) polyene.

a corresponding decrease in the contribution of the [H-1, H → L, L+1] excitation. It must be noted that the trifluoromethyl substituents on the polyene result in a torsion angle of 140° instead of 180° around the central carbon-carbon bond; the energy-minimized geometry indicates that the torsion is related to energetically favorable hydrogen bonding interactions between the fluorine and hydrogen atoms (H-F distances of 2.29 and 2.17 Å). Data from both the energetic minimum (solid lines) and a planar structure with one imaginary frequency (dotted lines) are shown in Figure 3.7, and reveal a fairly minor change to the pattern of $\mu_{ee'}$ as a function of the geometric difference.

These results highlight the critical feature of the energetic spacing of the frontier molecular orbital, which can be dictated by chemical substitution and the nodal patterns along the conjugated backbone, in determining the magnitude of $\mu_{ee'}$. The sign of the evolution in $\mu_{ee'}$ depends not on whether the substituent is electron-donating or electron-withdrawing but instead on how the substituent affects the molecular orbital energetic spacings. In particular, $\mu_{ee'}$ is small only when there is a large energetic spacing between the HOMO-1 and HOMO levels and the LUMO and LUMO+1 levels, which allows for nearly complete cancellation among the leading terms that contribute to $\mu_{ee'}$.

3.4. Conclusions

Evaluating the potential of third-order nonlinear optical materials requires a detailed understanding of the nature of the optical response beyond the first excited state, and in particular of the characteristics of the two-photon absorbing states. Although a large $\mu_{ee'}$ is critical for applications where two-photon absorption is desired, all-optical switching

applications require molecules with small $\mu_{ee'}$. Here, we have used a decomposition scheme to understand how the one- and two-electron configurations contributing to the *e* and *e'* states and the transitions between them ultimately determine the strength of $\mu_{ee'}$. While it has been noted previously[14] that $\mu_{ee'}$ is generally large when state *e'* consists primarily of one single-electron excitation and is smaller when state *e'* consists of a linear combination of single-electron and double-electron excitations, we have demonstrated how molecular structure, including effects of both conjugation length and substitution, influences the transition dipole moments of the individual electronic transitions that comprise $\mu_{ee'}$ in streptocyanines and polyenes.

The decomposition of $\mu_{ee'}$ indicates that its magnitude results from the interplay of two key factors: (i) the magnitudes of the pure component transition dipole moments that contribute to $\mu_{ee'}$, which relate to the spatial extent of the relevant frontier molecular orbitals (essentially from HOMO-1 to LUMO+1); and (ii) the contribution (CI coefficients) of each excitation to state *e'*, resulting from the energetic spacing of the frontier molecular orbitals. In particular, to achieve a small $\mu_{ee'}$ in polymethines, the contribution of the [H, H $\rightarrow$ L, L] configuration in *e'* should be large as it contributes in subtractive fashion to $\mu_{ee'}$. This can be accomplished by maintaining a large energetic spacing between the HOMO-1 and HOMO levels and the LUMO and LUMO+1 levels, such that the three configurations with significant contributions to *e'* are comparable in energy. When electron-donating and electron-withdrawing moieties are substituted on the central portions of the conjugated backbones, our results demonstrate that the same

substituent can either increase or decrease $\mu_{ee'}$ depending on the nodal patterns of the bridge-based frontier molecular orbitals.

The critical role of the energetic spacing of the frontier molecular orbitals in determining the magnitude of $\mu_{ee'}$ suggests design principles that can be applied as a broader range of structural modifications to the polymethines are considered. This is particularly true for potential end-group substituents, which have not been taken into account here. Such careful consideration should enable the design of chromophores with the large FOM critical for AOS applications.

3.5. References

(1) Marder, S. R.; Gorman, C. B.; Meyers, F.; Perry, J. W.; Bourhill, G.; Brédas, J. L.; Pierce, B. M. *Science* **1994**, *265*, 632.

(2) Meyers, F.; Marder, S. R.; Pierce, B. M.; Bredas, J. L. *J. Am. Chem. Soc.* **1994**, *116*, 10703.

(3) Hales, J. M.; Matichak, J.; Barlow, S.; Ohira, S.; Yesudas, K.; Bredas, J. L.; Perry, J. W.; Marder, S. R. *Science* **2010**, *327*, 1485.

(4) Hales, J. M.; Zheng, S.; Barlow, S.; Marder, S. R.; Perry, J. W. *J. Am. Chem. Soc.* **2006**, *128*, 11362.

(5) Fu, J.; Padilha, L. A.; Hagan, D. J.; Van Stryland, E. W.; Przhonska, O. V.; Bondar, M. V.; Slominsky, Y. L.; Kachkovskii, A. *J. Opt. Soc. Am. B* **2007**, *24*, 56.

(6) Matichak, J. D.; Hales, J. M.; Barlow, S.; Perry, J. W.; Marder, S. R. *J. Phys. Chem. A* **2011**, *115*, 2160.

(7) Padilha, L. A.; Webster, S.; Przhonska, O. V.; Hu, H.; Peceli, D.; Ensley, T. R.; Bondar, M. V.; Gerasov, A. O.; Kovtun, Y. P.; Shandura, M. P.; Kachkovski, A. D.; Hagan, D. J.; Van Stryland, E. W. *J. Phys. Chem. A* **2010**, *114*, 6493.

(8) Orr, B. J.; Ward, J. F. *Mol. Phys.* **1971**, *20*, 513.

(9) Gieseking, R. L.; Mukhopadhyay, S.; Risko, C.; Marder, S. R.; Brédas, J.-L. *Adv. Mater.* **2014**, *26*, 68.

(10) Mukhopadhyay, S.; Risko, C.; Marder, S. R.; Brédas, J.-L. *Chem. Sci.* **2012**, *3*, 3103.

(11) Wernke, W.; Pfeiffer, M.; Johr, T.; Lau, A.; Grahn, W.; Johannes, H.-H.; Dahne, L. *Chem. Phys.* **1997**, *216*, 337.

(12) Pierce, B. M. *Proc. SPIE* **1991**, *1560*, 148.

(13) Johr, T.; Wernke, W.; Pfeiffer, M.; Lau, A.; Dahne, L. *Chem. Phys. Lett.* **1995**, *246*, 521.

(14) Zojer, E.; Beljonne, D.; Kogej, T.; Vogel, H.; Marder, S. R.; Perry, J. W.; Brédas, J. L. *J. Chem. Phys.* **2002**, *116*, 3646.

(15) Guillaume, M.; Liégeois, V.; Champagne, B.; Zutterman, F. *Chem. Phys. Lett.* **2007**, *446*, 165.

(16) Mustroph, H.; Reiner, K.; Mistol, J.; Ernst, S.; Keil, D.; Hennig, L. *ChemPhysChem* **2009**, *10*, 835.

(17) Chai, J.-D.; Head-Gordon, M. *J. Chem. Phys.* **2008**, *128*, 084106.

(18) Dunning, T. H. *J. Chem. Phys.* **1989**, *90*, 1007.

(19) Gaussian 09, Revision B.01, M. J. Frisch, G. W. Trucks, H. B. Schlegel, G. E. Scuseria, M. A. Robb, J. R. Cheeseman, G. Scalmani, V. Barone, B. Mennucci, G. A. Petersson, H. Nakatsuji, M. Caricato, X. Li, H. P. Hratchian, A. F. Izmaylov, J. Bloino, G. Zheng, J. L. Sonnenberg, M. Hada, M. Ehara, K. Toyota, R. Fukuda, J. Hasegawa, M. Ishida, T. Nakajima, Y. Honda, O. Kitao, H. Nakai, T. Vreven, J. A. Montgomery, Jr., J. E. Peralta, F. Ogliaro, M. Bearpark, J. J. Heyd, E. Brothers, K. N. Kudin, V. N. Staroverov, T. Keith, R. Kobayashi, J. Normand, K. Raghavachari, A. Rendell, J. C. Burant, S. S. Iyengar, J. Tomasi, M. Cossi, N. Rega, J. M. Millam, M. Klene, J. E. Knox, J. B. Cross, V. Bakken, C. Adamo, J. Jaramillo, R. Gomperts, R. E. Stratmann, O. Yazyev, A. J. Austin, R. Cammi, C. Pomelli, J. W. Ochterski, R. L. Martin, K. Morokuma, V. G. Zakrzewski, G. A. Voth, P. Salvador, J. J. Dannenberg, S. Dapprich, A. D. Daniels, O. Farkas, J. B. Foresman, J. V. Ortiz, J. Cioslowski, and D. J. Fox, Gaussian, Inc., Wallingford CT, 2010.

(20) Ohira, S.; Hales, J. M.; Thorley, K. J.; Anderson, H. L.; Perry, J. W.; Bredas, J. L. *J. Am. Chem. Soc.* **2009**, *131*, 6099.

(21) Zojer, E.; Beljonne, D.; Pacher, P.; Bredas, J. L. *Chem. Eur. J.* **2004**, *10*, 2668.

(22) Zojer, E.; Wenseleers, W.; Halik, M.; Grasso, C.; Barlow, S.; Perry, J. W.; Marder, S. R.; Brédas, J.-L. *ChemPhysChem* **2004**, *5*, 982.

(23) For the two shortest polyenes, the active space was reduced to 15 HOMOs and 15 LUMOs. Although excited-state energies can sometimes change significantly with changing the size of the active space or moving from an SDCI to an MRDCI approach, the transition dipoles are much less affected.

(24) Malhotra, S. S.; Whiting, M. C. *J. Chem. Soc.* **1960**, 3812.

(25) Fabian, J.; Hartmann, H. *Light Absorption of Organic Colorants*; Springer-Verlag: Heidelberg, New York, 1980.

(26) Because of the C_{2v} symmetry, the transition from state *g* to state *e'* is symmetry-allowed only along the short molecular axis and $\mu_{ge'}$ is negligibly small.

(27) Since this electronic configuration has four unpaired electrons, there are two singlet configurations that both contribute to the polyene state *e'*. Consideration of the orbital overlap would imply that the pure transition dipole moment for a transition from H → L to H-1, H → L, L+1 is roughly half that of the other excitations with large

contributions to $\mu_{ee'}$; however, since the two singlets have contributions of opposite signs to $\mu_{ee'}$, the effective transition dipole moment is substantially smaller.

(28) Kohler, B. E.; Terpougov, V. *J. Chem. Phys.* **1996**, *104*, 9297.

(29) Dixit, S.; Guo, D.; Mazumdar, S. *Phys. Rev. B* **1991**, *43*, 6781.

(30) Mazumdar, S.; Guo, D.; Dixit, S. N. *J. Chem. Phys.* **1992**, *96*, 6862.

(31) Luo, Y.; Agren, H.; Stafstrom, S. *J. Phys. Chem.* **1994**, *98*, 7782.

(32) Beljonne, D.; Shuai, Z.; Serrano-Andres, L.; Brédas, J. L. *Chem. Phys. Lett.* **1997**, *279*, 1.

(33) Knippenberg, S.; Rehn, D. R.; Wormit, M.; Starcke, J. H.; Rusakova, I. L.; Trofimov, A. B.; Dreuw, A. *J. Chem. Phys.* **2012**, *136*, 064107.

(34) According to Reference 28, the measured two-photon fluorescence is 63 times greater for state *e"* than for state *e'*. Given that the two-photon fluorescence activity is directly proportional to Im(γ) when $2\hbar\omega$ is equal to the state energy, the experimental state energies and two-photon fluorescence activities can be used to approximate the ratio of $\mu_{ee'}$ to $\mu_{ee''}$ via the **T** term in the SOS expression.

CHAPTER 4

POLYMETHINE MOLECULAR STRUCTURE AND NONLINEAR OPTICAL PROPERTIES: DISTINGUISHING THE EFFECTS OF BOND-LENGTH AND BOND-ORDER ALTERNATION

4.1. Introduction

As delineated in the Introduction, the nonlinear optical properties of linear conjugated systems are strongly dependent on the degree of bond length alternation (BLA) and bond order alternation (BOA) along the molecular backbone.[1,2] Critically, the average BLA is defined as the difference between the average lengths of the nominally single bonds and the nominally double bonds along the linear π-conjugated backbone, while the average BOA is defined as the difference between the average bond orders of the same two sets of bonds. Although often conflated, BLA presents a measure of the molecular geometric structure (which often but not always reflects the electronic structure), whereas BOA directly assesses the molecular electronic structure.

Although the relationships between BLA and the molecular NLO properties have proven widely useful, recent theoretical investigations have questioned the extent of the applicability of these relationships in molecular design: molecular structures extracted from molecular dynamics simulations in explicit solvent present a very weak correlation between BLA and β.[3] To explore this correlation further, here we elucidate the limits of when the commonly-used relationships between BLA and the molecular NLO properties are applicable. In particular, we demonstrate that BLA and BOA are well correlated only

when the molecular geometry is the equilibrium geometry in the environment of interest. As BOA probes the molecular electronic structure, BOA is a good predictor of the molecular optical and NLO properties regardless of whether BOA reflects the molecular geometry. These results have important implications for the computational approaches used to study the molecular NLO properties.

4.2. Computational Methodology

Geometry optimizations for streptocyanines with polymethine bridges of five and nine methine units between two amino end groups were performed at the wB97X/cc-pVDZ level[4-6] in electric fields ranging from 0 to +7.5 x 10^7 V/cm (5-carbon) or +4.5 x 10^7 V/cm (9-carbon).[7] The minima were confirmed by the absence of imaginary frequencies. The excited-state properties and Mulliken bond orders were computed using the INDO/SDCI approach with an active space of 15 HOMOs and 15 LUMOs (5-carbon) or 25 HOMOs and 25 LUMOs (9-carbon) for single excitations and 4 HOMOs and 4 LUMOs for double excitations; this approach has been widely used for evaluating the NLO properties of conjugated systems and shown to provide results consistent with experiment.[2,8-11] The NLO properties were computed at the static (zero-frequency) limit using a sum-over-states approach[12] that sums over 350 excited states.

4.3. Results and Discussion

To elucidate separately the roles of BLA and BOA on molecular properties, we consider a prototypical 5-carbon streptocyanine (Figure 4.1) in three series of calculations:

(1) an electric field is applied along the long molecular axis and the molecular geometry is fully optimized for each value of the electric field, as was done in the original computational studies[2] showing the relationships between BLA and the NLO properties;

(2) an electric field is applied along the long molecular axis as in series (1) but the molecular geometry is constrained (and unrelaxed) to the C_{2v}-symmetric molecular geometry; and

(3) the geometries derived in series (1) are considered in the absence of an external electric field.

As linear conjugated systems are highly polarizable, the electric field has a very large effect on the charge distribution along the long molecular axis.[2]

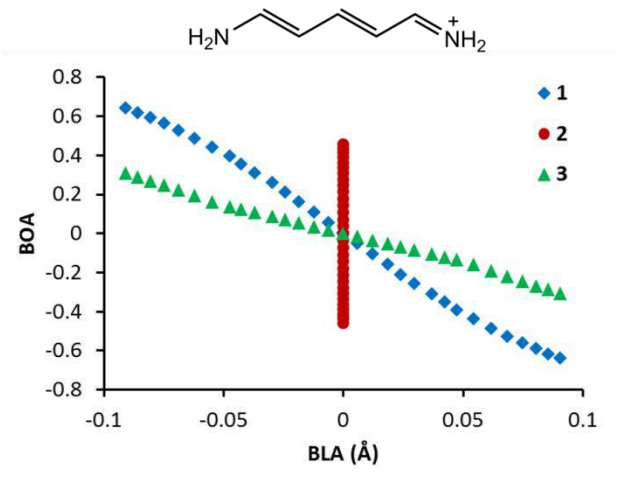

Figure 4.1. (Top) Chemical structure and (bottom) correlation between BLA and BOA for the 5-carbon streptocyanine. The three sets of colored symbols represent the different geometric and electric-field approximations employed in the study.

We first examine the evolution of BLA and BOA across each of the three series, which allows us to distinguish between the effects of BLA and BOA on the molecular properties. In Series 1 (blue diamonds, Figure 4.1), as the magnitude of the electric field increases, both BLA and BOA increase in magnitude from the cyanine limit (BLA = 0 Å, BOA = 0) to the polyene limit (BLA = -0.1 Å, BOA = +0.65; and BLA = +0.1 Å, BOA = -0.65), showing the characteristic range of geometric and electronic structures that have previously been observed in linear conjugated systems.[2] In contrast, in Series 2 (red circles, Figure 4.1), BLA is fixed at 0 Å. BOA, however, varies from -0.5 to +0.5 within the range of electric-field strengths examined. Even though the geometric structure is fixed, the BOA at each electric-field strength is roughly 70% of its value in the corresponding structure from Series 1. In Series 3 (green triangles, Figure 4.1), BLA varies from -0.1 Å to 0.1 Å; however, BOA for each geometry is only 30-50% of its value when the electric field is present. The geometric change induces only a relatively small change in the electronic structure in the absence of an electric field. Critically, these three series allow us to distinguish between changes in the geometric and electronic structures of the polymethines to show the relative effects of these two parameters on the NLO properties.

With the distinction between the geometric and electronic structures in mind, we consider the evolution of the ground-state dipole moment μ_g with BLA and BOA in these three series. In Series 1, μ_g is zero along the long molecular axis at the cyanine limit[13] and is large in magnitude at large values of both BLA and BOA (Figure 4.2). We note that the direction of the BLA axis has been reversed to ease comparison of the BLA and BOA

plots. The magnitude of μ_g near the polyene limit indicates that the positive charge is becoming localized primarily on one of the two terminal nitrogen atoms. In contrast, the other two series show notably different relationships between BLA and μ_g. In Series 2, there is substantial variation in μ_g despite the fixed molecular geometry; in Series 3, the variation in μ_g is relatively small despite the large change in geometry. When comparing the three series, the geometric structure alone is not sufficient to predict the molecular properties.

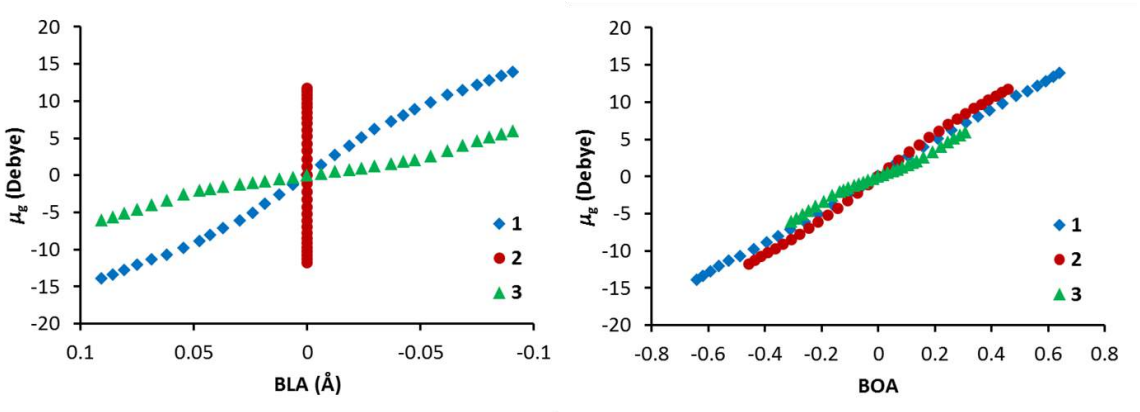

Figure 4.2. Correlation of μ_g with BLA and BOA for the 5-carbon streptocyanine. The three sets of colored symbols represent the different geometric and electric-field approximations employed in the study.

However, when bond orders are instead considered, all three series show nearly indistinguishable relationships between BOA and μ_g. Since BOA is a measure of the molecular electronic structure, BOA can be used to consistently predict the molecular properties. Importantly, when the geometry is far from the energetic minimum in the specific environment, BOA is a much more reliable predictor of the molecular properties than is BLA.

The evolution of the first excited-state energy E_{ge} is similarly correlated much more strongly with BOA than with BLA (Figure 4.3). As is typical of linear π-conjugated systems, E_{ge} is smaller near the cyanine limit than near the polyene limit. Importantly, in the absence of an electric field (Series 3), a very large change in the molecular geometry is required to induce any increase in E_{ge}; for BLA values up to 0.05 Å, E_{ge} remains within 0.01 eV of its value at the cyanine limit.

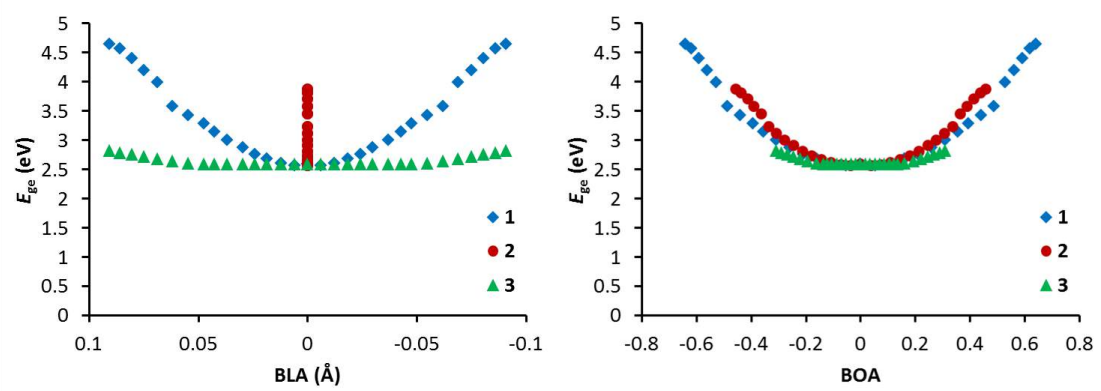

Figure 4.3. Correlation of E_{ge} with BLA and BOA for the 5-carbon streptocyanine.

The molecular NLO properties are likewise much more strongly correlated with BOA than with BLA across the three series (Figure 4.4). For α, β_x, and γ, Series 1 shows the evolution characteristic of linear conjugated systems with respect to either BLA or BOA; Series 2 and 3 show a similar evolution of the NLO properties only with respect to BOA. Without some knowledge of how the molecular structure relates to the environment, BLA cannot be used to predict (for instance) whether β_x is small or large or the sign of γ. As the NLO properties are computed using a sum-over-states approach in terms of the excited-state energies, state dipole moments, and transition dipole moments,[12] it is perhaps not surprising that a measure of the electronic structure is better at predicting the molecular NLO properties than is a geometric measure.

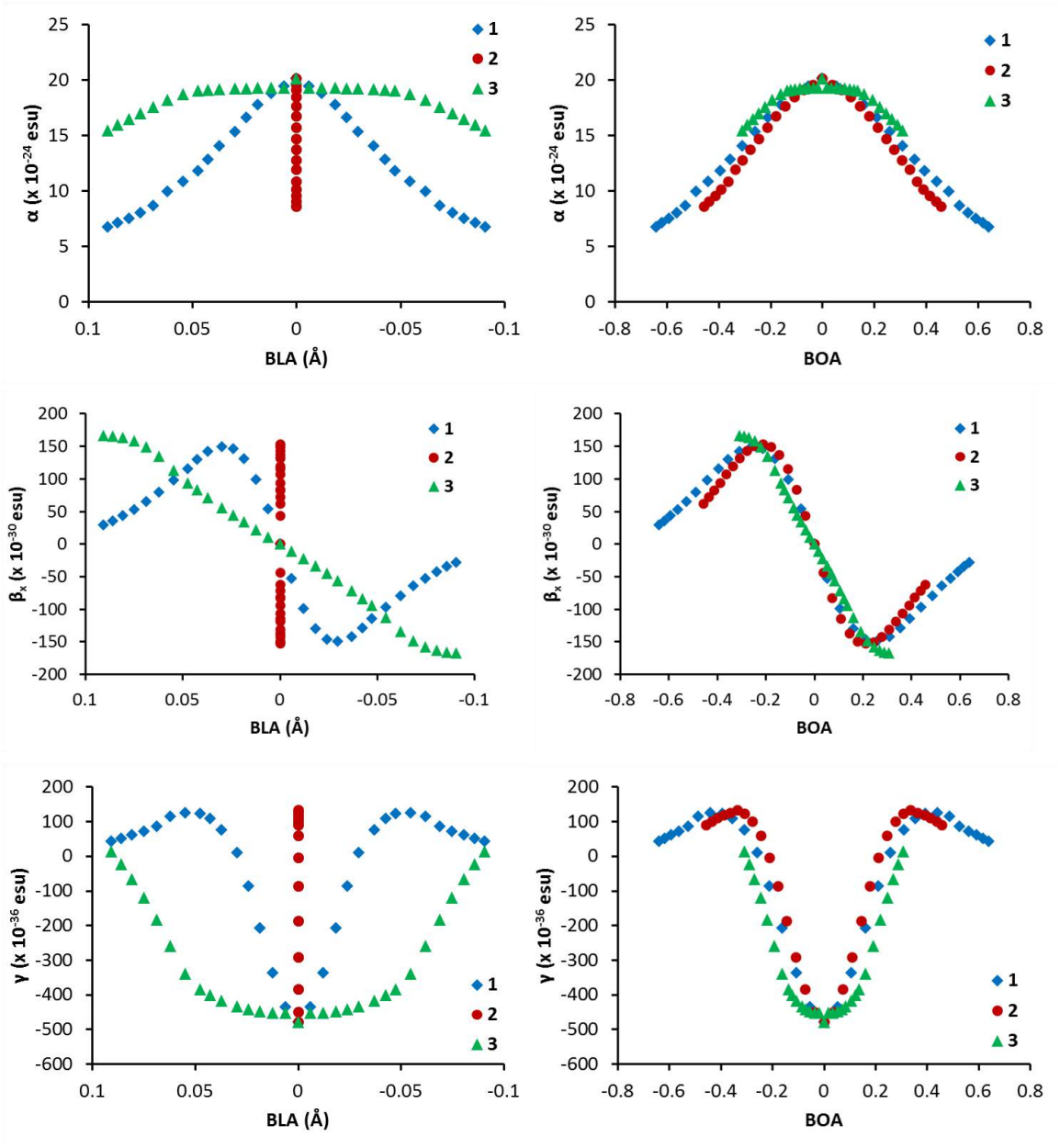

Figure 4.4. Correlation of (top) α, (middle) β_x, and (bottom) γ with BLA and BOA for the 5-carbon streptocyanine.

To demonstrate that this correlation can be generalized to other systems, we turn to analogous computations for the 9-carbon streptocyanine (Figure 4.5). The definitions of the three series are identical to those described previously for the 5-carbon streptocyanine. Here, it is likewise clear that BLA is a good predictor of the molecular

NLO properties only when the geometry is an energetic minimum in its electric-field environment; in contrast, BOA can be consistently used to predict the molecular NLO properties regardless of the geometric structure.

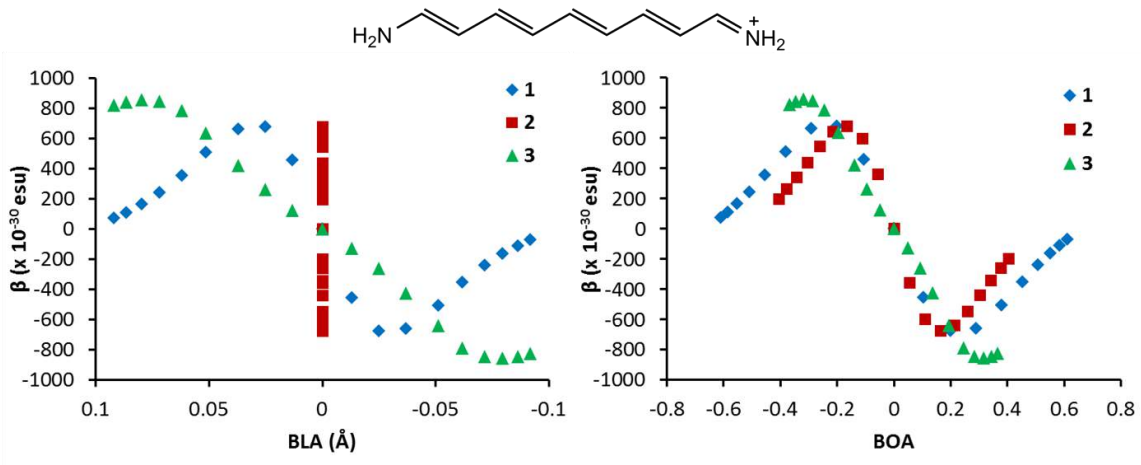

Figure 4.5. (Top) Chemical structure and (bottom) correlation β_x with BLA and BOA for the 9-carbon streptocyanine. The three sets of colored symbols represent the different geometric and electric-field approximations employed in the study.

4.4. Conclusions

Although BLA and BOA are often conflated, properly distinguishing and accounting for the relationships between the molecular geometric and electronic structures is critical to design studies that provide further understanding of relationships between the molecular structure and NLO properties. Experimentally, it is not possible to change the geometric and electronic structures independently; thus, the widely-applied correlations between BLA and the NLO properties should be generally reliable. Computationally, one must take great care in selecting an approach to adequately address the questions of interest. Several considerations must be taken into account:

(i) To understand the relationships between the molecular geometry and NLO properties, it is important to consider a geometry that is an energetic minimum in the environment (electric field, solvent, counterion, etc.) in which the NLO properties are computed.

(ii) When considering molecules in complex environments, removal of the molecule from its environment may substantially modify the electronic structure even if the molecular geometry is retained. Maintaining the key features of the environment is essential to accurately assess the NLO properties.

(iii) When considering molecular geometries that are displaced from their energetic minimum, the electronic structure will not change as much as the geometric changes may seem to imply. This is consistent with the previously-observed weak correlation between BLA and NLO properties in geometries extracted from dynamics simulations.[3] In this case, changes in BOA will be a much more accurate predictor of variation in the NLO properties than are changes in BLA.

Careful design of computational studies that account for the distinction between BLA and BOA is critical to understanding the optical and NLO properties of π-conjugated molecules in complex environments.

4.5. References

(1) Marder, S. R.; Gorman, C. B.; Meyers, F.; Perry, J. W.; Bourhill, G.; Brédas, J. L.; Pierce, B. M. *Science* **1994**, *265*, 632.

(2) Meyers, F.; Marder, S. R.; Pierce, B. M.; Bredas, J. L. *J. Am. Chem. Soc.* **1994**, *116*, 10703.

(3) Murugan, N. A.; Kongsted, J.; Rinkevicius, Z.; Agren, H. *Proc. Natl. Acad. Sci. USA* **2010**, *107*, 16453.

(4) Chai, J.-D.; Head-Gordon, M. *Phys. Chem. Chem. Phys.* **2008**, *10*, 6615.

(5) Chai, J.-D.; Head-Gordon, M. *J. Chem. Phys.* **2008**, *128*, 084106.

(6) Dunning, T. H. *J. Chem. Phys.* **1989**, *90*, 1007.

(7) Due to the molecular symmetry, the sign of the electric field determines the sign of BLA but does not affect its magnitude; thus, rather than duplicate calculations, the data was mirrored to show results across the full range of BLA values.

(8) Zojer, E.; Beljonne, D.; Kogej, T.; Vogel, H.; Marder, S. R.; Perry, J. W.; Brédas, J. L. *J. Chem. Phys.* **2002**, *116*, 3646.

(9) Zojer, E.; Beljonne, D.; Pacher, P.; Bredas, J. L. *Chem. Eur. J.* **2004**, *10*, 2668.

(10) Zojer, E.; Wenseleers, W.; Halik, M.; Grasso, C.; Barlow, S.; Perry, J. W.; Marder, S. R.; Brédas, J.-L. *ChemPhysChem* **2004**, *5*, 982.

(11) Gieseking, R. L.; Mukhopadhyay, S.; Risko, C.; Brédas, J.-L. *ACS Photon.* **2014**, *1*, 261.

(12) Orr, B. J.; Ward, J. F. *Mol. Phys.* **1971**, *20*, 513.

(13) As the dipole moment of a charged system depends on the choice of origin, we have selected the molecular center of mass as the origin.

CHAPTER 5

SYMMETRY BREAKING OF POLYMETHINES

5.1. Introduction

As described in the Introduction, whereas short polymethines typically have (nearly) C_{2v}-symmetric geometries with their charge distributed symmetrically across the molecule, experimental evidence suggests that sufficiently long polymethines have symmetry-broken geometries with large BLA and their charge localized primarily on one end of the molecule.[1-10] The length at which the crossover from symmetric to symmetry-broken structures occurs is strongly dependent on the molecular structure and environment.[2,5,11] In solution, the symmetry-broken polymethine absorption peaks are broadened on the high-energy side or shifted to higher energy.[1,5,12-14] However, these absorption spectra are challenging to interpret. Although it has been proposed that the broadened absorption peaks may be due to a mixture of symmetric and symmetry-broken polymethines,[15] current experimental evidence is insufficient to test this hypothesis.

Computational studies can provide insight into polymethine symmetry-breaking that is not readily accessible experimentally; however, accurate modeling of symmetry-breaking in π-conjugated systems is challenging.[16,17] The symmetry-breaking behavior of polymethines depends on a delicate energetic balance of the forces that favor delocalization of the wavefunction (i.e. delocalization of charge; resonance) and those that favor localization of the wavefunction (i.e. higher stability of localizing charge on an end group vs. a bridge carbon; Peierls-type distortion).[4,17,18] Determining the crossover

point from a single-well potential energy surface to a double-well potential energy surface requires computing the geometries and vibrational frequencies of large molecules, which limits the use of high-level approaches due to the large computational costs. Although the C_{2v}-symmetric geometries of streptocyanines with $–NH_2$ end groups have previously been computed at the CCSD(T)/6-31G* level up to a bridge length of 13 carbons,[19] the lack of vibrational frequencies and restriction of these calculations to isolated moderate-length molecules limits the usefulness of these calculations for understanding symmetry-breaking.

Lower-level computational methods provide upper and lower limits for the crossover point. Calculations based on the Hartree-Fock (HF) approach, known to over-localize the wavefunction and thus over-estimate BLA values[20-22] and consequently to over-predict symmetry-breaking,[23,24] indicate that the crossover point for streptocyanines occurs at a bridge length of 19 carbons in the gas phase.[16] On the other hand, typical Density Functional Theory (DFT) approaches over-delocalize the wavefunction and predict overly small BLA[20-22] and symmetric structures;[25,26] the commonly-used functional B3LYP maintains symmetric streptocyanine structures to a bridge length of at least 39 carbons.[16,17] The length at which the crossover point occurs can be tuned by varying the % HF exchange in hybrid functionals.[21] However, in the structurally related polyenes, typical hybrid functionals poorly reproduce the evolution of BLA with molecular length.[27] Long-range corrected (LRC) functionals, which include short-range DFT exchange and long-range HF exchange,[28,29] provide much more accurate evolution of the polyene BLA with molecular length if an appropriate constant range-separation

parameter ω is selected; we note, however, that using IP-tuned ω values at each molecular length yields little improvement in BLA over hybrid functionals.[27] To date, the accuracy of LRC functionals for polymethine BLA has not been investigated.

Here, we evaluate the accuracy of the CC2/TZVP and ωPBEh/6-31G* computational approaches relative to a CCSD(T)/6-31G* standard[19] for the streptocyanines (Figure 5.1; D = 1), focusing on the molecular geometries and charge distributions. We then consider the effect of implicit solvation on the molecular structures, the infrared (IR) spectra, and the lengths at which the streptocyanines symmetry-break. We consider the effect of the end group chemical structure on the length of symmetry-breaking and show that the lengths of symmetry-breaking at the ωPBEh/6-31G* in implicit solvent are in reasonable agreement with experimental evidence. Finally, we present preliminary results for the ground- and excited-state potential energy surfaces of polymethines displaced along key vibrational modes.

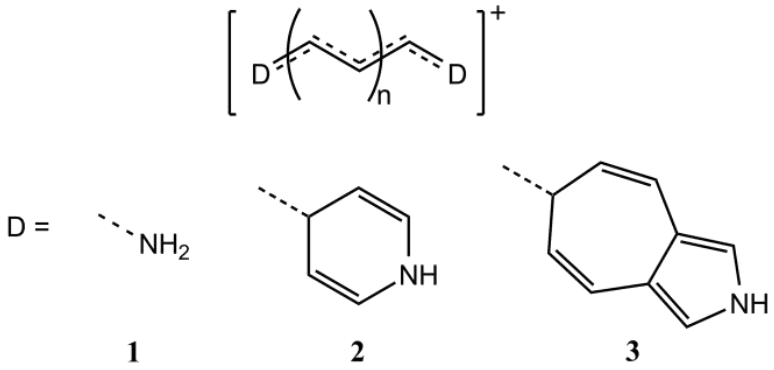

Figure 5.1. Chemical structures of polymethines studied here. The number of carbon atoms in the polymethine bridge N = 2n + 1.

5.2. Computational Methodology

Geometry optimizations and frequency calculations for the streptocyanines were performed using a CC2 approach.[30] The TZVP basis set[31] was selected for use because previous calculations[32] show that a triple-zeta basis set is required to properly model the excited-state energetic spacing; this allows for computation of the excited-state energies at the same level of theory used for the ground-state optimizations. The first three excited states were computed for the optimized ground-state geometries and for geometries displaced along several normal modes of b_2 symmetry. These calculations were performed using the TURBOMOLE V6.1 program.

Geometry optimizations and frequency calculations were also performed with a DFT approach using the long-range corrected ωPBEh functional[33] and the 6-31G* basis set. The range-separation parameter ω was fixed to the default value of 0.200 $bohr^{-1}$ since this value has previously yielded good agreement with the CCSD(T) BLA in polyenes;[27] as will be shown later, this value likewise provides good agreement with the CCSD(T) streptocyanine BLA. Geometry optimizations were performed for C_{2v}-symmetric structures and (for polymethines with imaginary frequencies) for symmetry-broken structures with C_s symmetry. Calculations were performed both in the gas phase and using the SM8 model of implicit solvation.[34] These calculations were performed using Q-Chem 4.0.1. Computations of the polymethines with azaazulene end groups were provided by Mahesh Kumar.

Atomic charges were computed via the natural bond order (NBO) population analysis for all optimized geometries at the CC2/TZVP and ωPBEh/6-31G* levels. As the relaxed density matrix at the CCSD(T) level is not generally available, NBO charges were also computed at the CCSD/6-31G* level for geometries optimized at the CCSD(T)/6-31G* level from the literature.[19]

5.3. Results and Discussion

5.3.1. Geometric structures and charge distributions

As the molecular charge distributions and bond lengths in the polymethine bridge reflect the factors that determine symmetry-breaking, we first assess the accuracy of the CC2/TZVP and ωPBEh/6-31G* approaches by comparing the charge distributions and molecular geometries of streptocyanines (Figure 5.1; D = 1) with lengths of 3-13 carbons to high-level computational standards (CCSD(T)/6-31G* geometries;[19] CCSD/6-31G* charges). At this length range, the C_{2v}-symmetric structures are the energetic minima; the trends provide understanding of the evolution of the C_{2v}-symmetric structures whether this structure is the energetic minimum or a transition state between symmetry-broken minima.

Polymethines inherently have significant charge alternation along the molecular backbone.[19,35-37] As shown in the resonance forms in Figure 5.2, the odd-numbered carbon atoms along the polymethine backbone should bear more positive charge than do the even-numbered carbon atoms. The charge on each $–NH_2$ end group reflects the energetic stabilization provided by those groups. To simplify comparison of the

molecules, we consider the NBO atomic charges with the hydrogen charges summed into the corresponding heavy atoms.

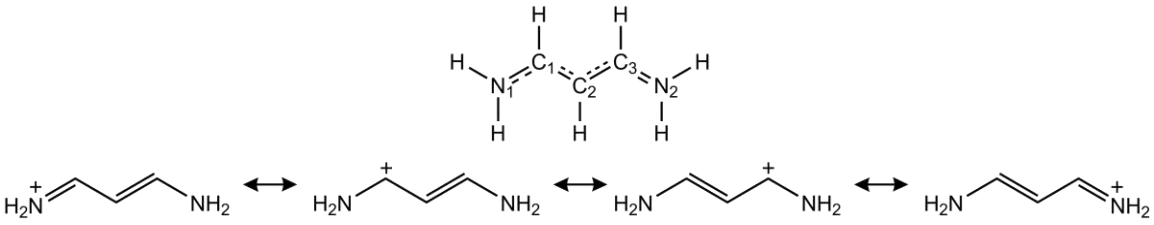

Figure 5.2. (Top) General chemical structure showing atom numbering and (bottom) resonance forms for the 3-carbon streptocyanine.

The atomic charges at all three levels of theory reflect the picture described by these resonance forms (Figure 5.3 and Table 5.1), with positive charges on the end groups and odd-numbered carbons and slight negative charges on the even-numbered carbons. As the charge distributions are symmetric, only charges on one half of each molecule are listed. The majority of the positive charge (> 0.4 electron per polymethine end) is localized on the end groups and the terminal carbon atoms; on the central atoms, there is significant charge alternation but relatively little net charge. As the molecular length increases (while maintaining C_{2v} symmetry), there are more atoms over which to delocalize the charge, and the charges on the end groups and terminal carbon atoms become smaller.

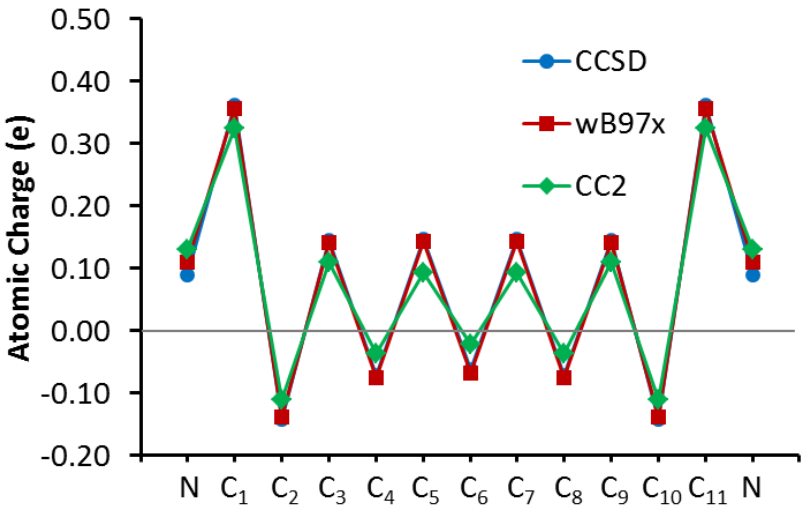

Figure 5.3. NBO atomic charges of the 11-carbon streptocyanine; the charges of the hydrogens are summed into the heavy atoms.

Table 5.1. NBO atomic charges of streptocyanines; the charges of the hydrogens are summed into the heavy atoms.

Level	**N**	**Atomic Charge (*e*)**							
		N_1	**C_1**	**C_2**	**C_3**	**C_4**	**C_5**	**C_6**	**C_7**
CCSD/ 6-31G*	3	0.166	0.430	-0.192					
	5	0.143	0.408	-0.144	0.186				
	7	0.122	0.390	-0.140	0.170	-0.085			
	9	0.105	0.375	-0.140	0.157	-0.075	0.157		
	11	0.090	0.362	-0.141	0.146	-0.072	0.148	-0.063	
	13	0.077	0.350	-0.143	0.135	-0.070	0.139	-0.058	0.141
CC2/ TZVP	3	0.191	0.393	-0.170					
	5	0.172	0.367	-0.120	0.163				
	7	0.155	0.349	-0.112	0.137	-0.058			
	9	0.141	0.335	-0.110	0.121	-0.043	0.111		
	11	0.130	0.325	-0.111	0.110	-0.036	0.094	-0.023	
	13	0.121	0.317	-0.112	0.102	-0.034	0.082	-0.014	0.077
ωPBEh/ 6-31G*	3	0.174	0.415	-0.180					
	5	0.153	0.396	-0.137	0.176				
	7	0.135	0.379	-0.135	0.162	-0.083			
	9	0.121	0.366	-0.137	0.151	-0.077	0.152		
	11	0.109	0.356	-0.139	0.141	-0.076	0.143	-0.068	
	13	0.099	0.346	-0.141	0.133	-0.075	0.135	-0.066	0.136

Comparison of the atomic charges across the three levels of theory reveals some minor differences. At each atomic position, the deviation of the CC2 and ωPBEh charges from the CCSD charges is less than 0.04 electrons; ωPBEh gives atomic charges that are somewhat closer to those computed at the CCSD level. Both CC2 and ωPBEh yield slightly more positive charge on the end groups than does CCSD, by 0.025-0.044 and 0.008-0.022 electrons, respectively. The localization of excess charge on the end groups is accompanied by a similar reduction of the charge on the terminal carbons, particularly at the CC2 level. The charge alternation across the central part of the molecular backbone is slightly muted at the CC2 level.

The carbon-carbon bond lengths are highly sensitive to bond order. The most commonly used definition of BLA in linear conjugated systems is the *average BLA* as was discussed in the Introduction and in Chapter 4, defined as

$$\text{Average BLA} = \frac{(b_{1-2} + b_{3-4} + \cdots) - (b_{2-3} + b_{4-5} + \cdots)}{(N-1)/2} \qquad 5.1$$

where b_{x-y} is the bond length between the atoms C_x and C_y and N is the number of carbon atoms in the polymethine backbone. As described in the Introduction, polyenes with alternating single and double bonds have average BLAs of around 0.1 Å, whereas C_{2v}-symmetric polymethines have average BLAs of exactly zero by symmetry. Since the average BLA is not useful here to compare symmetric polymethines, we focus on two BLA parameters: the *absolute average BLA*, defined as the average of the absolute differences between adjacent carbon-carbon bond lengths along the polymethine backbone,

$$\text{Absolute Average BLA} = \frac{|b_{1-2} - b_{2-3}| + |b_{2-3} - b_{3-4}| + \cdots}{(N-2)} \qquad 5.2$$

and the *terminal BLA*, defined as the difference between the bond lengths of the two adjacent carbon-carbon bonds nearest one end group of the polymethine (as long as C_{2v} symmetry is retained, the terminal BLA near each end group will be identical).

$$\text{Terminal BLA} = (b_{1-2} - b_{2-3}) \qquad 5.3$$

The overall pattern of bond length alternation is qualitatively similar at all three levels of theory (Figure 5.4 and Table 5.2): when C_{2v} symmetry is maintained, the central two C-C bonds are identical in length, and the absolute difference between adjacent C-C bond lengths increases as the distance from the center of the molecule increases via a pattern of alternating shorter and longer bonds. As for the atomic charges, bond lengths on only one half of the molecule are tabulated. The terminal C-C bonds are consistently short, bearing more double-bond character.

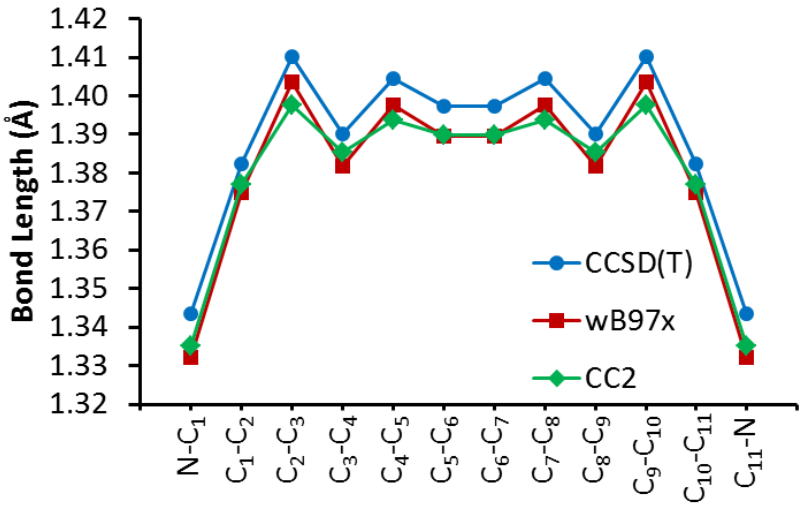

Figure 5.4. Bond lengths and BLA of the 11-carbon streptocyanine.

Table 5.2. Bond lengths and BLA of streptocyanines.

Level	N	Abs Avg BLA (Å)	Terminal BLA (Å)	Bond Lengths (Å)						
				b_{N-1}	b_{1-2}	b_{2-3}	b_{3-4}	b_{4-5}	b_{5-6}	b_{6-7}
CCSD(T)/ 6-31G*	3	0.000	0.000	1.326	1.393					
	5	0.004	0.006	1.332	1.392	1.398				
	7	0.008	0.015	1.336	1.388	1.403	1.396			
	9	0.012	0.022	1.340	1.385	1.407	1.393	1.401		
	11	0.015	0.028	1.344	1.382	1.410	1.390	1.405	1.397	
	13	0.018	0.034	1.347	1.380	1.414	1.388	1.408	1.394	1.401
CC2/ TZVP	3	0.000	0.000	1.318	1.381					
	5	0.004	0.006	1.325	1.383	1.390				
	7	0.007	0.012	1.329	1.381	1.393	1.389			
	9	0.009	0.017	1.332	1.379	1.395	1.387	1.392		
	11	0.010	0.021	1.335	1.377	1.398	1.385	1.394	1.390	
	13	0.011	0.024	1.337	1.376	1.399	1.384	1.395	1.389	1.392
ωPBEh/ 6-31G*	3	0.000	0.000	1.316	1.387					
	5	0.005	0.007	1.322	1.385	1.391				
	7	0.009	0.015	1.326	1.381	1.396	1.389			
	9	0.013	0.023	1.329	1.377	1.400	1.385	1.394		
	11	0.017	0.029	1.332	1.375	1.404	1.382	1.398	1.389	
	13	0.020	0.034	1.334	1.372	1.407	1.379	1.401	1.386	1.393

Although the overall evolution of the bond lengths is qualitatively similar across all three levels of theory, several key differences emerge. The C-C bond lengths are an average of 0.008 Å shorter at both the CC2 and ωPBEh levels than at the CCSD(T) level. At the CC2 level, the decrease in the N-C bond length is comparable to the average contraction of the C-C bonds, but BLA is reduced in the longer polymethines relative to the CCSD(T) structures. In contrast, the ωPBEh geometries show a slightly greater reduction in the N-C bond lengths, particularly for longer polymethines, but much better agreement with the CCSD(T) BLA.

In summary, comparison of atomic charges and bond lengths suggests that both CC2 and ωPBEh are in reasonable agreement with the high-level standards and should provide

useful information about symmetry-breaking in polymethines. The CC2 results deviate slightly more from the high-level standards, and as CC2 is substantially more computationally expensive, it is more limited in its applicability; however, it has the advantage that (in principle) it provides a route toward systematic improvement through the use of higher-level coupled-cluster approaches. The ωPBEh results show particularly good agreement with the CCSD(T) BLA; however, as the selection of the functional is empirical, there is not a clear systematic route toward a more accurate DFT-based approach.

5.3.2. Effect of Implicit Solvation

As the solvent dielectric constant affects the length at which symmetry-breaking occurs experimentally,[1,2] we also consider the effect of implicit solvation on the molecular charge distributions and geometries. We focus on the structures at the ωPBEh level using the SM8 solvent model; implicit solvation at the CC2 level is not currently implemented in Turbomole. Here, we highlight the 7-carbon and 11-carbon streptocyanines to show the effect of molecular length on the extent of changes due to solvation.

Consideration of implicit solvation increases the positive charge on the nitrogen and terminal carbon atoms by up to 0.08 electrons (Figure 5.5). This is unsurprising, since solvent typically stabilizes the localization of charge. The impact of solvent on the molecular charges increases with increasing molecular length; in simulations of DMSO and water, the charge on the end groups is nearly independent of molecular length. Although the effect of the solvent generally increases as the dielectric constant increases,

DMSO (ε = 46.8) has a larger effect on the molecular charge distribution than does water (ε = 78.4). The SM8 solvent model depends on parameters such as the refractive index and acidity/basicity in addition to the dielectric constant; the differences in these parameters may have a larger effect in this case than does the difference between the dielectric constants of these solvents.

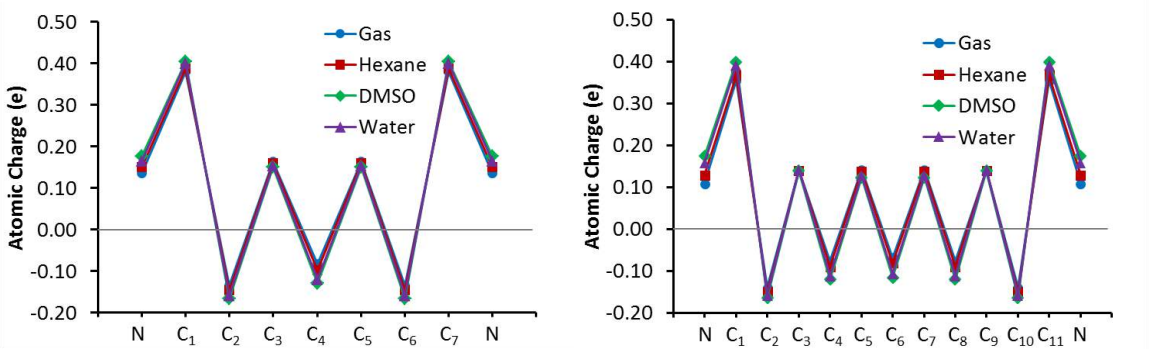

Figure 5.5. Atomic charges of the (left) 7-carbon and (right) 11-carbon streptocyanines in the gas phase and in hexane (ε = 1.88), dimethyl sulfoxide (DMSO; ε = 46.8), and water (ε = 78.4) at the ωPBEh/6-31G* level.

The consideration of solvent similarly affects the bond lengths. The N-C bond lengths decrease in implicit solvent, suggesting that the resonance forms with the charge on the nitrogen atoms and N=C double bonds have more significant contributions to the overall electronic structure. The terminal C-C bonds are correspondingly lengthened, and the absolute average BLA decreases to < 0.002 Å in DMSO for bridge lengths up to 11 carbons. These geometric changes are consistent with the changes in the atomic charges. As with the atomic charges, the implicit solvent has a larger effect on the geometries of longer polymethines.

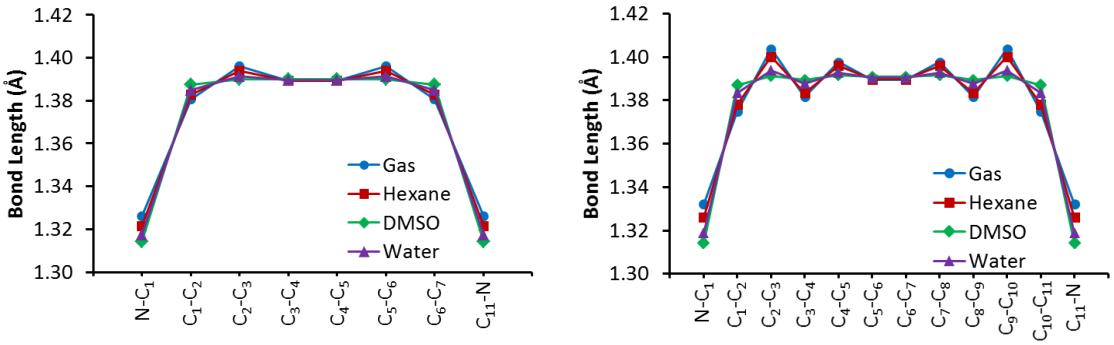

Figure 5.6. Bond lengths of the (left) 7-carbon and (right) 11-carbon streptocyanines in implicit solvent at the ωPBEh/6-31G* level of theory.

5.3.3. Vibrational Frequencies and Symmetry-Breaking

To this point, we have focused solely on polymethine structures with C_{2v} symmetry. As symmetry-breaking is associated with an increase in BLA and localization of charge on one molecular end, this process is associated with distortion of the C_{2v}-symmetric structure along a coordinate of b_2 symmetry. Since stretching of C-C bonds is required to change BLA, we focus on vibrational modes with frequencies < 2000 cm^{-1}. To determine whether the C_{2v}-symmetric structures are energetic minima or transition states between two symmetry-broken minima, we examine the vibrational frequencies: transition structures are expected to have one imaginary frequency with b_2 symmetry corresponding to a large change in BLA, whereas energetic minima are expected to have all real frequencies.[38] We also analyze the IR spectra of the molecules; because symmetry-breaking involves a large change in the molecular dipole moment, the IR intensities (directly proportional to the derivative of the dipole moment with respect to displacement) of the modes most strongly associated with symmetry-breaking should be large.

In the gas phase, the polymethines retain C_{2v} symmetry up to very long bridge lengths. At the CC2/TZVP level, no symmetry-breaking is observed at bridge length up to 17 carbons, the largest molecule considered. At the ωPBEh/6-31G* level, the crossover point occurs at a bridge length of 35 carbons; at this length, a vibrational mode of b_2 symmetry with an imaginary frequency of 131.3 cm^{-1} is observed.

The streptocyanines, particularly the longer molecules, have many carbon-carbon stretching modes; however, only a few modes of b_2 symmetry have large IR intensities. In the short polymethines, two vibrational modes have particularly large IR intensities: one around 1250 cm^{-1} and one around 1600 cm^{-1}. These modes both involve large changes in BLA; the lower-frequency mode involves synchronous motion of each methine unit, whereas the higher-frequency mode involves bending of each methine unit (Figure 5.7).

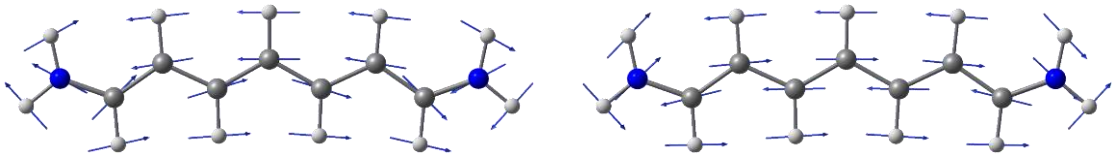

Figure 5.7. Vibrational modes for the 7-carbon streptocyanine at the ωPBEh/6-31G* level with frequencies of (left) 1248.6 cm^{-1} and (right) 1615.5 cm^{-1}.

The frequencies and IR intensities of these two modes change with streptocyanine length. At the CC2 level, the frequencies of the two modes are relatively constant; at the molecular length increases from 7 to 17 carbons, the frequency of each mode varies by less than 20 cm^{-1}. In contrast, at the ωPBEh level, the frequencies of both modes decrease with increasing molecular length (Figure 5.8); within the same range of lengths, the

frequencies of the two modes decrease by 140-190 cm^{-1}. For the shortest streptocyanines, the IR intensities are very similar at the CC2 and ωPBEh levels. As the molecular length increases, the IR intensities of these two modes greatly increase. At the CC2 level, the higher-frequency mode maintains an IR intensity more than double that of the lower-frequency mode at all molecular lengths. In contrast, at the ωPBEh level, the IR intensities show a more dramatic increase with increasing molecular length: in the 15- and 17-carbon streptocyanines, the IR intensities of the lower-frequency and higher-frequency modes are larger than those of the equivalent modes at the CC2 level by factors of more than 2 and more than 10, respectively.

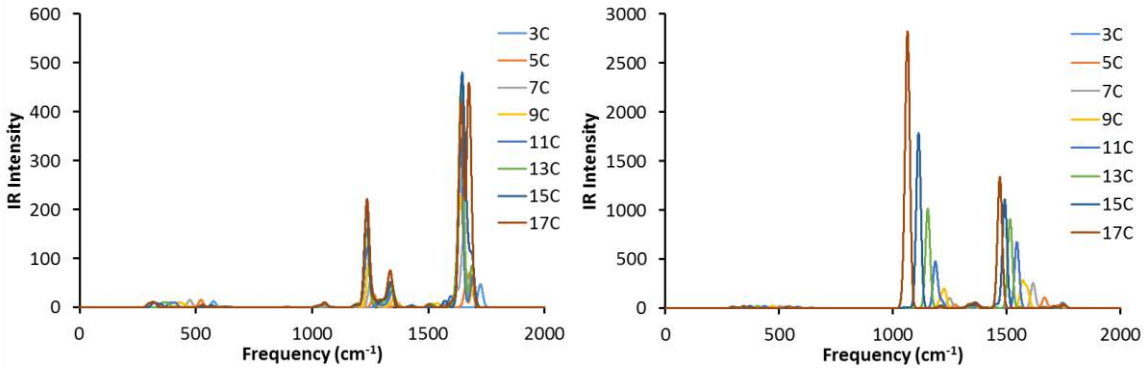

Figure 5.8. Infrared spectra at the (left) CC2/TZVP and (right) ωPBEh/6-31G* levels.

In the longer polymethines (at the ωPBEh level), the lower-frequency mode shifts to lower frequencies as molecular length increases until the point of symmetry-breaking is reached, and the higher-frequency mode shifts to about 1400 cm^{-1}. The IR intensities, particularly that of the lower-frequency mode, continue to increase with increasing molecular length. In some of the longer polymethines, mixing of several vibrational modes yields several modes with large intensities within a small frequency range. The

shift of the vibrational modes to lower frequencies is not observed from the current CC2 computations; it is unclear to this point whether this is due to the limited size of the molecules that have been studied or to differences between the computational approaches.

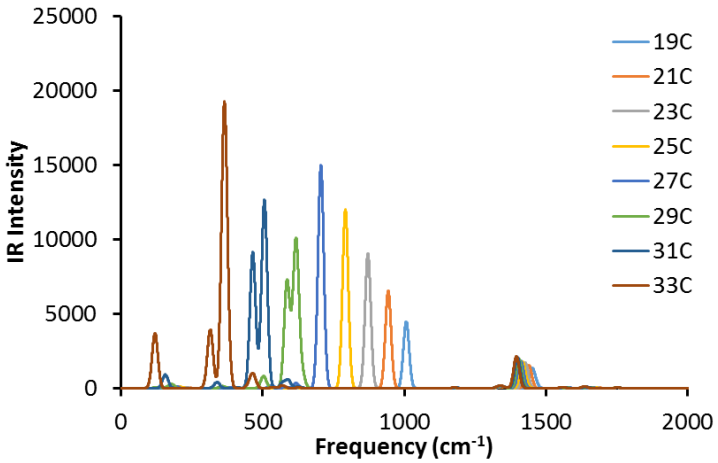

Figure 5.9. Infrared spectra of long streptocyanines at the ωPBEh/6-31G* level.

Consideration of implicit solvation dramatically affects the length at which the molecular symmetry breaks. Computation of the IR intensities in solvent at the ωPBEh level is not currently implemented in Q-Chem, so we focus on the imaginary frequencies obtained in these calculations. The crossover points occur at 13 carbons in both DMSO and water and 23 carbons in hexane (Table 5.3). As the molecular length increases beyond the crossover point, the imaginary frequency of the mode associated with symmetry-breaking becomes larger.

Table 5.3. Streptocyanine imaginary frequencies, energetic difference ΔE between the C_{2v} and C_s structures, and BLA at the ωPBEh/6-31G* level.

N	**Solvent**	**Imaginary Freq. (cm^{-1})**	**ΔE (kcal/mol)**	**BLA (Å)**		
				C_{2v} Abs. Avg.	**C_s Abs. Avg.**	**C_s Avg.**
35	-	131.3	-0.001	0.050	0.053	0.003
23	Hexane	311.1	-0.006	0.026	0.029	0.002
25	Hexane	530.8	-0.426	0.027	0.067	0.044
13	DMSO	607.0	-0.294	0.002	0.047	0.046
15	DMSO	1011.8	-1.194	0.002	0.062	0.061
13	Water	505.5	-0.173	0.006	0.041	0.040
15	Water	934.5	-0.982	0.007	0.060	0.059

For the streptocyanines with imaginary frequencies, we also compare the C_{2v}-symmetric transition states to the C_s-symmetric energetic minima. For the 35-carbon streptocyanine in the gas phase, the energetic stabilization upon symmetry-breaking is extremely small, more than two orders of magnitude smaller than thermal energy at room temperature (0.6 kcal/mol). The C_{2v}-symmetric structure has a fairly large absolute average BLA owing to symmetrically-distributed alternation far from the molecular center. Upon symmetry-breaking, the change in the molecular geometry is small, as evidenced by the small average BLA and small increase in the absolute average BLA. In implicit solvent, the energetic stabilization upon symmetry-breaking is more significant and is larger for molecules further beyond the crossover point; in fact, for the 15-carbon streptocyanines in DMSO and water, the stabilization upon symmetry-breaking is greater than thermal energy. The changes in geometry upon symmetry-breaking are also more significant, transitioning from structures where all carbon-carbon bond lengths are nearly equal in length to structures with substantial alternation across the entire molecule.

5.3.4. Effect of End Groups

To compare the computed length of symmetry-breaking to that observed experimentally, we now turn to polymethines with end groups that extend the effective conjugation length (Figure 5.1). As mentioned previously, it is challenging to directly compare the computed crossover point to the experimental absorption spectra; however, it is possible to at least check whether the computed crossover point is at a bridge length similar to that at which broadening of the experimental absorption spectrum is observed. Because of the size of the molecules required to reach the crossover point with larger end groups, only results at the ωPBEh level are considered here.

The extended conjugation in the larger end groups substantially decreases the length at which the polymethines symmetry-break. For polar solvents, these results seem reasonable when compared with experimental evidence. The pyridinium polymethines in DMSO experimentally show substantial broadening of their absorption peak at 9 carbons and a shift of the absorption peak to higher energy at 13 carbons,[5] which agrees well with our computed results (Table 5.4). The azaazulene polymethines show noticeable broadening of their absorption peaks at 9 carbons in dichloromethane (DCM) and 7 carbons in acetonitrile (ACN),[12] slightly longer than the computed lengths of symmetry-breaking. This discrepancy may be due to simplifications to the end group used computationally; several alkyl groups, which may somewhat shield the solvent from the end groups, were not considered in our calculations. The overall consistency with experiment demonstrates that our approach is reliable enough to provide insight into the symmetry-breaking process in polymethines.

Table 5.4. Bridge lengths (*N*) at which polymethines symmetry-break at the ωPBEh/6-31G* level.

D	Vacuum (ε=1)	Hexane (ε=1.88)	DCM (ε=8.93)	ACN (ε=35.68)	DMSO (ε=46.82)
Amino (1)	35	23	-	-	13
Pyridinium (2)	23	15	-	-	9
Azaazulene (3)	23	15	7	5	-

5.3.5. Excited States

An appropriate model for the vibronic couplings between diabatic states could provide significant insight into the factors that affect polymethine symmetry-breaking. Although few-state models parameterized to fit experimental data can yield broadened absorption peaks similar to those seen experimentally,[39-42] it is unclear whether the models used to date consider a set of states and vibrational modes that provides chemically-relevant understanding; the empirical fitting also limits the applicability of these models to systems for which experimental data are unavailable. High-level computational modeling is required to determine which states and modes are critical to describe the vibronic interactions that lead to polymethine symmetry-breaking.

We first consider the first few excited-state energies for the C_{2v}-symmetric streptocyanines at the CC2/TZVP level (Figure 5.10). As is typical of polymethines, the first excited state *e* has B_2 symmetry and consists primarily of a HOMO → LUMO excitation. The first two excited states of A_1 symmetry, *e'* and *e"*, are composed largely of HOMO-1 → LUMO and HOMO → LUMO+1 excitations, respectively, with significant contributions from double excitations. For streptocyanines five carbons and longer, states *e'* and *e"* are the second and third excited states. However, for the 3-carbon streptocyanine, several states of A_2 and B_1 symmetry that do not involve excitations

within the π system fall between states *e'* and *e"*; in addition, the primary excitations contributing to states *e'* and *e"* are reversed in the 3-carbon streptocyanine relative to the longer polymethines. The excited-state energies decrease with increasing molecular length. The ratio of the first and second excited-state energies $E_{ge'}/E_{ge}$ is close to 1.7 for the streptocyanines of at least five carbons, much closer to the experimentally expected ratio[43] than is provided by most other computational approaches.[44-47]

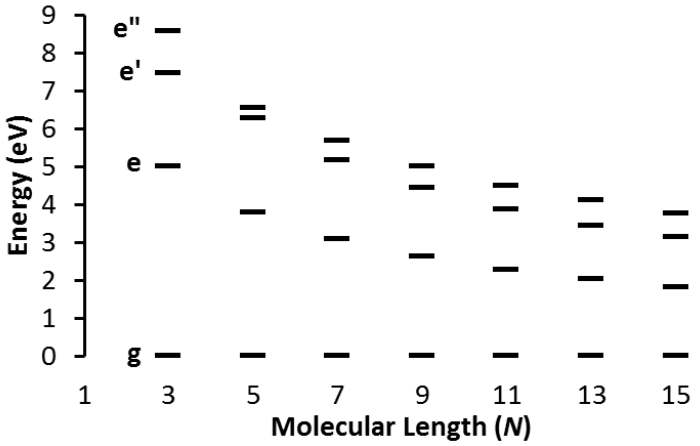

Figure 5.10. Excited-state energies of streptocyanines at the CC2/TZVP level.

Since the polymethines have many vibrational modes, we first consider the state symmetries to understand what couplings are possible among the first several states. As described in the previous section, the geometric change upon symmetry-breaking primarily involves displacement along modes of b_2 symmetry with frequencies < 2000 cm^{-1}; displacement along the totally-symmetric a_1 coordinates may also occur, whereas no displacement is expected along modes of b_1 and a_2 symmetry (which involve out-of-plane bending). Among the first few polymethine states, modes with a_1 symmetry can displace the energetic minima of the excited-states relative to the ground-state minimum

and can couple pairs of states of the same symmetry (in our case, states *g*, *e'*, and *e"*), whereas modes of b_2 symmetry can couple one state of A_1 symmetry with a state of B_2 symmetry (state *e*).

As a first step toward understanding the vibronic couplings between the first several polymethine states, we compute the adiabatic potential energy surfaces of the ground state and first several excited states for molecular geometries displaced along vibrational modes of b_2 symmetry; analysis of the potential energy surfaces along modes of a_1 symmetry is still in progress. The fitting of the computed adiabatic potentials to an appropriate diabatic model also remains to be performed. In vibronic coupling theory, it is generally assumed that, since the wavefunctions of the diabatic states are unchanged upon geometric displacement, the potential energy surfaces of the diabatic states have the same curvature to a first approximation. Thus, a large difference between the curvatures of the adiabatic potential energy surfaces suggests significant vibronic couplings involving the mode under consideration. The geometric displacements are scaled in terms of the dimensionless normal coordinate *q*. The state energies were computed for geometries displaced up to 2*q* from the energetic minimum; the trend lines in the following figures showing a harmonic fit to the adiabatic potentials are extended to larger values of *q* to more clearly show the differences in curvature between the states.

We focus first on the 3-carbon streptocyanine; as this molecule has only seven modes of b_2 symmetry with frequencies less than 2000 cm^{-1}, we consider the potential energy surfaces along all of these modes (Figure 5.11). The state vibrational frequencies along

select modes were fit to a harmonic potential (Table 5.5; the labeling of the modes corresponds to that in Figure 5.11). For many of the modes considered (a, b, e, f), the adiabatic potential energy surfaces for all states are very similar, implying that these modes do not provide significant vibronic coupling. In Figure 5.11d, state *e"* has a distinctly flatter potential energy surface than do the lower-energy states; however, preliminary calculations using a Hamiltonian where only one mode couples these four states show that this model is insufficient to explain this change.

Table 5.5. Harmonic fits for the vibrational frequencies of the first several 3-carbon streptocyanine states along select normal modes. Since the ground-state frequencies listed here are fit to the adiabatic potential, the values differ slightly from the frequencies in Figure 5.11.

Mode	**Frequencies (cm^{-1})**			
	g	***e***	***e'***	***e"***
(b)	1079.3	1055.3	1048.1	1007.3
(c)	1288.4	1160.4	1347.3	1175.0
(d)	1335.3	1269.8	1366.3	824.4
(g)	1718.1	1480.1	1635.7	1068.1

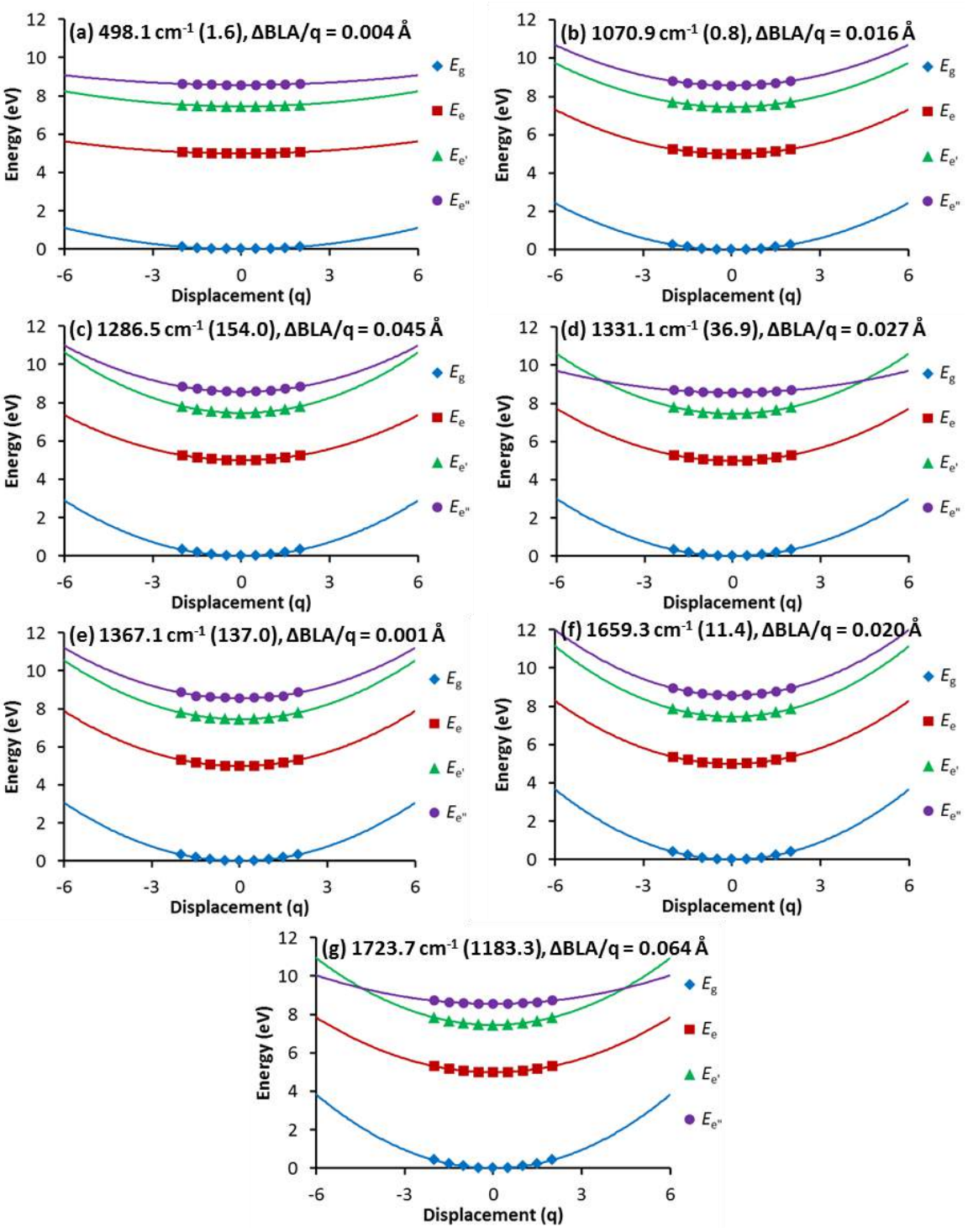

Figure 5.11. Potential energy surfaces of the ground state and first several excited states for displacement along the 3-carbon streptocyanine normal modes. For each mode, the frequency (IR intensity) and change in average BLA upon displacement by q are indicated.

The two b_2 modes with the largest IR intensities and changes in BLA (Figure 5.11c and g) have significant differences in curvature between the state adiabatic potential energy surfaces, suggesting large vibronic couplings involving these modes. In particular, states *e* and *e"* have significantly flattened potential energy surfaces as compared to states *g* and *e'*. This causes E_{ge} to somewhat decrease as the molecule is displaced along the vibrational mode and BLA increases. As described in Chapter 4, although symmetry-breaking of the polymethine electronic structure results in a significant increase in E_{ge}, displacement of the geometric structure away from the C_{2v}-symmetric minimum typically results in substantially smaller changes in the molecular electronic structure. The flattening of the state *e* potential suggests that the coupling between this state and the higher-lying states may be larger than the coupling between state *e* and the ground state; further analysis will be required to confirm this hypothesis.

For the longer polymethines, we focus on the two modes of b_2 symmetry with the largest IR intensities, which are associated with large changes in BLA. As in the 3-carbon polymethine, the adiabatic potential energy surfaces of states *e* and *e"* are somewhat flattened relative to those of the other states, particularly for the higher-frequency mode (Figure 5.12). As the polymethine length increases, the states become more closely spaced, but the curvatures of the adiabatic potential energy surfaces for each state do not change significantly.

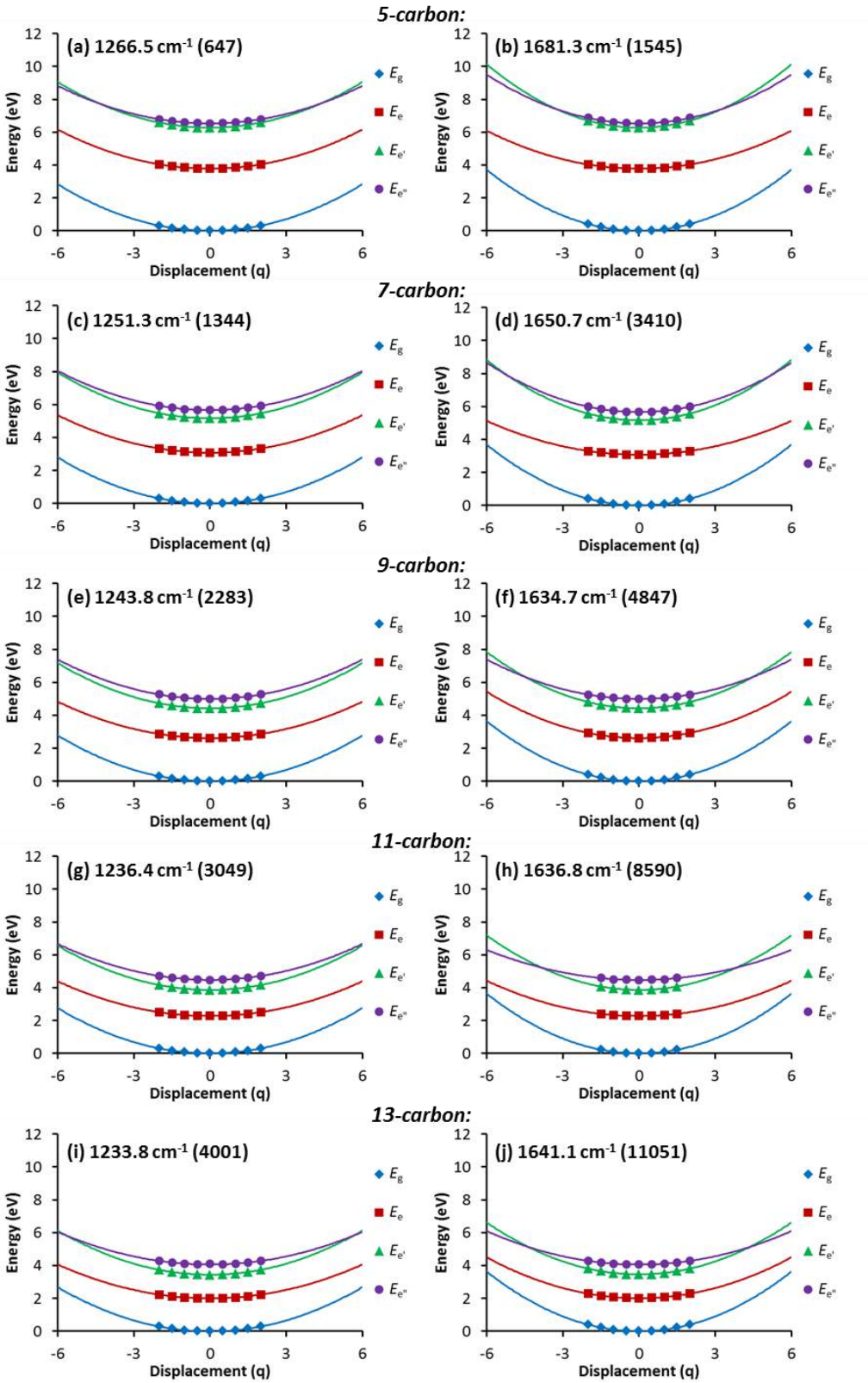

Figure 5.12. Potential energy surfaces of the ground state and first several excited states for displacement along the normal modes of streptocyanines of 5-13 carbons. For each mode, the frequency and IR intensity are indicated.

As these molecules have C_{2v} symmetry and do not show any significant flattening of the ground-state potential energy surface along the modes considered, it is challenging to relate these results to symmetry-broken polymethines at this stage. Analysis of molecules with flatter or double-well ground-state potential energy surfaces will be required to develop a diabatic model that includes the key vibronic couplings contributing to symmetry-breaking and understand how the chemical structure affects those couplings.

5.4. Conclusions

A computational understanding of the symmetry-breaking process in polymethines is needed to understand how molecular structure and environment affect the length at which polymethines symmetry-break. Here, we have shown that the streptocyanine structures at the CC2/TZVP and ωPBEh/6-31G* levels are in good agreement with the CCSD(T)/6-31G* structures.[19] Comparison of the ωPBEh/6-31G* results to experimental absorption spectra for polymethines with conjugated end groups provides further evidence that this computational approach can be used to provide insight into symmetry-breaking.

Our calculations have also provided insight into the molecular structures of the polymethines and the changes upon symmetry-breaking. In the gas phase, polymethines retain C_{2v} symmetry to very long bridge lengths but acquire significant alternation in the carbon-carbon bond lengths far from the molecular center; little change in this geometric pattern is observed upon symmetry-breaking. In contrast, in polar solvents, short polymethines have more charge localized in their end groups and very small BLA while symmetry is retained. However, symmetry-breaking occurs at much shorter bridge

lengths and a much larger change in BLA occurs upon symmetry-breaking because of the stabilization of charge on one of the end groups.

These initial results can be further expanded to provide insight into the factors affecting symmetry-breaking in polymethines. In particular, CC2/TZVP calculations of polymethines near and beyond the crossover point would be useful to understand how the polymethine potential energy surfaces change around the point of symmetry-breaking; the DFT results suggest that this may be possible by considering implicit solvent for the streptocyanines. Evaluation of these potential energy surfaces could lead to an appropriate diabatic representation for the polymethine states and a better understanding of the absorption spectra of polymethines near the point of symmetry-breaking.

5.5. References

(1) Lepkowicz, R. S.; Przhonska, O. V.; Hales, J. M.; Fu, J.; Hagan, D. J.; Van Stryland, E. W.; Bondar, M. V.; Slominsky, Y. L.; Kachkovski, A. D. *Chem. Phys.* **2004**, *305*, 259.

(2) Bouit, P.-A.; Aronica, C.; Toupet, L.; Guennic, B. L.; Andraud, C.; Maury, O. *J. Am. Chem. Soc.* **2010**, *132*, 4328.

(3) Yu, A.; Tolbert, C. A.; Farrow, D. A.; Jonas, D. M. *J. Phys. Chem. A* **2002**, *106*, 9407.

(4) Tolbert, L. M.; Ogle, M. E. *J. Am. Chem. Soc.* **1990**, *112*, 9519.

(5) Tolbert, L. M.; Zhao, X. *J. Am. Chem. Soc.* **1997**, *119*, 3253.

(6) Wernke, W.; Pfeiffer, M.; Johr, T.; Lau, A.; Grahn, W.; Johannes, H.-H.; Dahne, L. *Chem. Phys.* **1997**, *216*, 337.

(7) Fuyura, K.; Inagaki, Y.; Torii, H.; Furukawa, Y. T., Mitsuo *J. Phys. Chem. A* **1998**, *102*, 8413.

(8) Fuyura, K.; Torii, H.; Furukawa, Y.; Tasumi, M. *J. Phys. Chem. A* **2000**, *104*, 11203.

(9) Marks, A. F.; Noah, A. K.; Sahyun, M. R. V. *J. Photochem. Photobiol., A* **2001**, *139*, 143.

(10) Zoueu, J. T.; Fiorini-Debuisschert, C.; Charra, F.; Nunzi, J.-M. *Chem. Phys. Lett.* **2006**, *419*, 454.

(11) Barlow, S.; Henling, L. M.; Day, M. W.; Marder, S. R. *Chem. Commun.* **1999**, 1567.

(12) Przhonska, O. V.; Hu, H.; Webster, S.; Bricks, J. L.; Viniychuk, A. A.; Kachkovski, A. D.; Slominsky, Y. L. *Chem. Phys.* **2013**, *411*, 17.

(13) Kachkovski, O. D.; Tolmachov, O. I.; Slominskii, Y. L.; Kudinova, M. O.; Derevyanko, N. O.; Zhukova, O. O. *Dyes Pigm.* **2005**, *64*, 207.

(14) Vasyluk, S. V.; Viniychuk, O. O.; Poronik, Y. M.; Kovtun, Y. P.; Shandura, M. P.; Yashchuk, V. M.; Kachkovsky, O. D. *J. Mol. Struct.* **2011**, *990*, 6.

(15) Hu, H.; Przhonska, O. V.; Terenziani, F.; Painelli, A.; Fishman, D.; Ensley, T. R.; Reichert, M.; Webster, S.; Bricks, J. L.; Kachkovski, A. D.; Hagan, D. J.; Van Stryland, E. W. *Phys. Chem. Chem. Phys.* **2013**, *15*, 7666.

(16) Fabian, J. *J. Mol. Struct.: THEOCHEM* **2006**, *766*, 49.

(17) Iordanov, T. D.; Davis, J. L.; Masunov, A. E.; Levenson, A.; Przhonska, O. V.; Kachkovski, A. D. *Int. J. Quantum Chem.* **2009**, *109*, 3592.

(18) Tolbert, L. M. *Acc. Chem. Res.* **1992**, *25*, 561.

(19) Jacquemin, D. *J. Phys. Chem. A* **2011**, *115*, 2442.

(20) Jacquemin, D.; Femenias, A.; Chermette, H.; Ciofini, I.; Adamo, C.; Andre, J.-M.; Perpète, E. A. *J. Phys. Chem. A* **2006**, *110*, 5952.

(21) Jacquemin, D.; Adamo, C. *J. Chem. Theory Comput.* **2011**, *7*, 369.

(22) Ho Choi, C.; Kertesz, M.; Karpfen, A. *J. Chem. Phys.* **1997**, *107*, 6712.

(23) Lambert, C.; Noll, G. *J. Am. Chem. Soc.* **1999**, *121*, 8434.

(24) Nelsen, S. F.; Blomgren, F. *J. Org. Chem.* **2001**, *66*, 6551.

(25) Coropceanu, V.; Malagoli, M.; Andre, J. M.; Brédas, J. L. *J. Am. Chem. Soc.* **2002**, *124*, 10519.

(26) Coropceanu, V.; Lambert, C.; Nöll, G.; Brédas, J. L. *Chem. Phys. Lett.* **2003**, *373*, 153.

(27) Korzdorfer, T.; Parrish, R. M.; Sears, J. S.; Sherrill, C. D.; Bredas, J. L. *J. Chem. Phys.* **2012**, *137*, 124305.

(28) Chai, J.-D.; Head-Gordon, M. *Phys. Chem. Chem. Phys.* **2008**, *10*, 6615.

(29) Chai, J.-D.; Head-Gordon, M. *J. Chem. Phys.* **2008**, *128*, 084106.

(30) Christiansen, O.; Koch, H.; Jorgensen, P. *Chem. Phys. Lett.* **1995**, *243*, 409.

(31) Weigend, F. *Phys. Chem. Chem. Phys.* **2006**, *8*, 1057.

(32) Send, R.; Valsson, O.; Filippi, C. *J. Chem. Theory Comput.* **2011**, *7*, 444.

(33) Rohrdanz, M. A.; Martins, K. M.; Herbert, J. M. *J. Chem. Phys.* **2009**, *130*, 054112.

(34) Cramer, C. J.; Truhlar, D. G. *Acc. Chem. Res.* **2008**, *41*, 760.

(35) Dahne, S.; Kulpe, S. *Abh. Akad. Wiss. DDR, Abt. Math. Naturwiss., Tech.* **1977**, *8*, 1.

(36) Dahne, S.; Ranft, J. Z. *Z. Phys. Chem.* **1963**, *224*, 65.

(37) Kachkovski, A. D.; Dekhtyar, M. L. *Dyes Pigm.* **1996**, *30*, 43.

(38) At the wPBEh/6-31G* level, some long polymethines (15-carbon or longer in the gas phase; 19-carbon or longer in hexane) have small imaginary frequencies (< 100 cm-1) of b1 symmetry corresponding to bending of the polymethine away from planarity. As there is no energetic stabilization upon displacement along these modes, these modes are assumed to be due to numerical error and have been neglected.

(39) Sissa, C.; Jahani, P. M.; Soos, Z. G.; Painelli, A. *ChemPhysChem* **2012**, *13*, 2795.

(40) Terenziani, F.; Przhonska, O. V.; Webster, S.; Padilha, L. A.; Slominskii, Y. L.; Davydenko, I. G.; Gerasov, A. O.; Kovtun, Y. P.; Shandura, M. P.; Kachkovski, A. D.; Hagan, D. J.; Van Stryland, E. W.; Painelli, A. *J. Phys. Chem. Lett.* **2010**, *1*, 1800.

(41) Olsen, S. *J. Phys. Chem. A* **2012**, *116*, 1486.

(42) Olsen, S.; McKenzie, R. H. *J. Chem. Phys.* **2009**, *131*, 234306.

(43) Fu, J.; Padilha, L. A.; Hagan, D. J.; Van Stryland, E. W.; Przhonska, O. V.; Bondar, M. V.; Slominsky, Y. L.; Kachkovskii, A. *J. Opt. Soc. Am. B* **2007**, *24*, 56.

(44) Schreiber, M.; Buß, V.; Fülscher, M. P. *Phys. Chem. Chem. Phys.* **2001**, *3*, 3906.

(45) Mukhopadhyay, S.; Risko, C.; Marder, S. R.; Brédas, J.-L. *Chem. Sci.* **2012**, *3*, 3103.

(46) Karaca, S.; Elmacı, N. *J. Mol. Struct.: THEOCHEM* **2009**, *915*, 149.

(47) Gieseking, R. L.; Mukhopadhyay, S.; Risko, C.; Brédas, J.-L. *ACS Photon.* **2014**, *1*, 261.

CHAPTER 6

NEGATIVE THIRD-ORDER POLARIZABILITY OF XPH_4

($X = B^-, C, N^+, P^+$)

6.1. Introduction

Although AOS devices can in principle be made using materials with either a positive or negative value of $Re(\chi^{(3)})$, in practice a negative $Re(\chi^{(3)})$ can provide important benefits. Since materials with positive $Re(\chi^{(3)})$ are self-focusing,[1-3] the peak intensity of each light signal increases as the pulse travels through the material. This limits the laser intensity that can be used without risking dielectric breakdown of the NLO material.[4] As the change in the refractive index is linearly dependent on the intensity of light, reducing the light intensity would require a larger $Re(\chi^{(3)})$ or a longer interaction length for a functional device. Materials with negative $Re(\chi^{(3)})$ are self-defocusing, which may alleviate these challenges.

Although molecules and materials possessing negative $Re(\gamma)$, and hence a negative nonlinear refractive index n_2, could provide substantial benefits for device applications, to date relatively few classes of materials have been shown to have negative $Re(\gamma)$.[5-14] Without exception, inorganic materials show positive n_2 in the long wavelength limit,[15,16] leaving organic materials as the sole route to materials with negative n_2. Developing new classes of molecules with negative $Re(\gamma)$ requires understanding the molecular processes that affect the sign and magnitude of γ.

To this point, we have focused on the molecular design principles describing the sign and magnitude of Re(γ) in linear π-conjugated systems such as polymethines [6,17-19] and donor-acceptor-substituted polyenes,[5,6,17] which have been developed through understanding the relationship between the first several excited state properties and geometric parameters related to bond-length alternation (BLA) along the π backbone. However, this molecular understanding of Re(γ) has not yet been extended to higher-dimensional systems where the essential-state model (Equation 1.17) is not applicable and the third-order NLO properties can only be understood in terms of the full SOS expression (Equation 1.14).

Here, we present a new class of molecules with negative Re(γ): tetraphenyl compounds $X(C_6H_5)_4$, where X = B^-, C, N^+, and P^+ (Figure 6.1). We first describe the geometric and electronic structures of these molecules, which have three-dimensional π systems and do not correspond with the geometric parameters typically used to understand the sign of Re(γ) in linear conjugated systems. We then describe the excited-state properties and NLO properties, showing that the sign and magnitude of Re(γ) can be understood only in terms of the properties of a band of excited states in the context of the full SOS model.

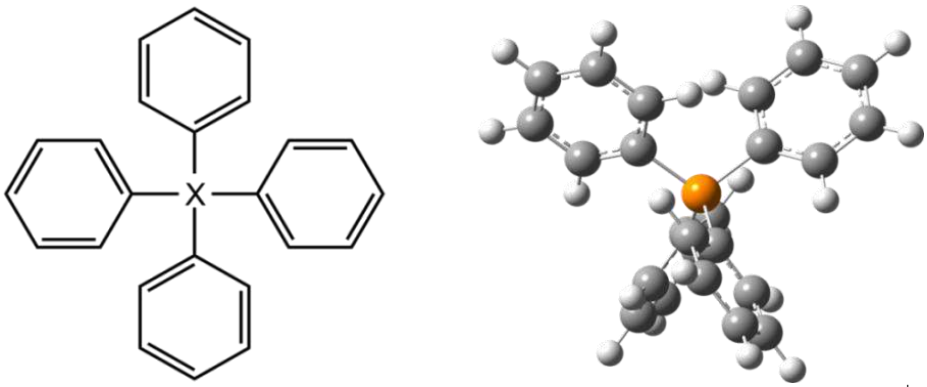

Figure 6.1. General chemical structure of the XPh4 series (X = B^-, C, N^+, P^+) and geometric structure of PPh_4^+.

6.2. Methods

The geometric structures were optimized via density functional theory (DFT) using the ωB97XD functional[20,21] and cc-pVDZ basis set[22] as implemented in the Gaussian 09 (Rev. B.01) suite of programs.[23] All minima were confirmed by the absence of imaginary frequencies. As the molecules have S_4 symmetry, the *z* axis was defined as the axis of symmetry. The excited-state properties were then evaluated using the INDO/SCI approach. The CI active space included all single-electron excitations within the 25 highest-lying occupied molecular orbitals (MOs) and 25 lowest-lying unoccupied MOs. Although double-electron excitations are usually critical to accurately compute the low-lying excited state properties of π-conjugated systems,[24-28] test calculations incorporating double-electron excitations through SDCI or MRDCI schemes show that the first 40-60 excited states in these systems contain negligible double-excitation character; hence, excitations with such character are neglected through use of the SCI approach.

The NLO properties were computed using the SOS approach (power series expansion). The total static Re(γ) and Im(γ) were computed by summing over 100 states. The decomposition of contributions by excited state was computed by calculating the static γ separately for each state *u* in the full SOS expression. The static γ was also decomposed into contributions from the **D**, **T**, and **N** terms; in decomposing the full SOS expression (Equation 1.14), the first summation comprises the **D** term ($u=v=w$) and the **T** term ($u\neq v$ and/or $v\neq w$), and the second summation comprises the **N** term. The orientationally averaged Re(γ) is computed from the tensor components as

$$\gamma_{\text{avg}} = \frac{1}{5}\left(\gamma_{\text{xxxx}} + \gamma_{\text{yyyy}} + \gamma_{\text{zzzz}}\right) + \frac{1}{15}\left(\gamma_{\text{xxyy}} + \gamma_{\text{yyxx}} + \gamma_{\text{xyyx}} + \gamma_{\text{xyxy}} + \gamma_{\text{yxyx}} + \gamma_{\text{yxxy}} + \gamma_{\text{xxzz}} + \gamma_{\text{zzxx}} + \gamma_{\text{xzzx}} + \gamma_{\text{xzxz}} + \gamma_{\text{zxzx}} + \gamma_{\text{zxxz}} + \gamma_{\text{zzyy}} + \gamma_{\text{yyzz}} + \gamma_{\text{zyyz}} + \gamma_{\text{zyzy}} + \gamma_{\text{yzyz}} + \gamma_{\text{yzzy}}\right) \quad 6.1$$

6.3. Results and Discussion

6.3.1. Ground-state properties

We start by discussing the geometric and electronic structures of the series of tetraphenyl compounds $X(C_6H_5)_4$, where X = B^-, C, N^+, and P^+. All of these systems have energetic minima in geometries with S_4 symmetry. The bond lengths in the phenyl rings are similar across the series, and the rings maintain the aromatic character associated with isolated benzene rings. This can be seen through analysis of the quinoidal-benzene character (QBC), defined as $\sum_i\left(\left|r_i - 1.4\ \text{Å}\right|\right)$ where r_i is the length of each C-C bond i in the phenyl ring.[29] The QBC values for these compounds are all very small (< 0.05 Å; we note that for squaraines, the crossover point from aromatic-like structures with positive Re(γ) to quinoid-like structures with negative Re(γ) was computed to be on the order of 0.17 Å).[7] This indicates that the phenyl rings largely retain their aromatic character; the quinoidal form has a minimal contribution to the ring conjugation pattern. The negative Re(γ) in polymethines and squaraines can be attributed to the molecule being in a transitional geometry between two resonance forms, where the ground state is highly polarizable. In the XPh_4 series, the molecular geometries suggest that the negative Re(γ) cannot be attributed to the same cause.

The frontier molecular orbitals (MOs) in the XPh_4 series are π-orbitals. The eight highest occupied MOs are composed of linear combinations of the two highest occupied orbitals of each of the four phenyl rings, and similarly the eight lowest unoccupied MOs are composed of linear combinations of the two lowest unoccupied orbitals of each phenyl ring (Figure 6.2). In all members of the series, the HOMO is doubly degenerate, whereas the LUMO is non-degenerate. The non-degenerate MOs are fully delocalized across all four phenyl rings; in the degenerate MO pairs, the total electron density of the two orbitals is distributed evenly across all four phenyl rings but each individual orbital may be localized primarily on two of the four rings.

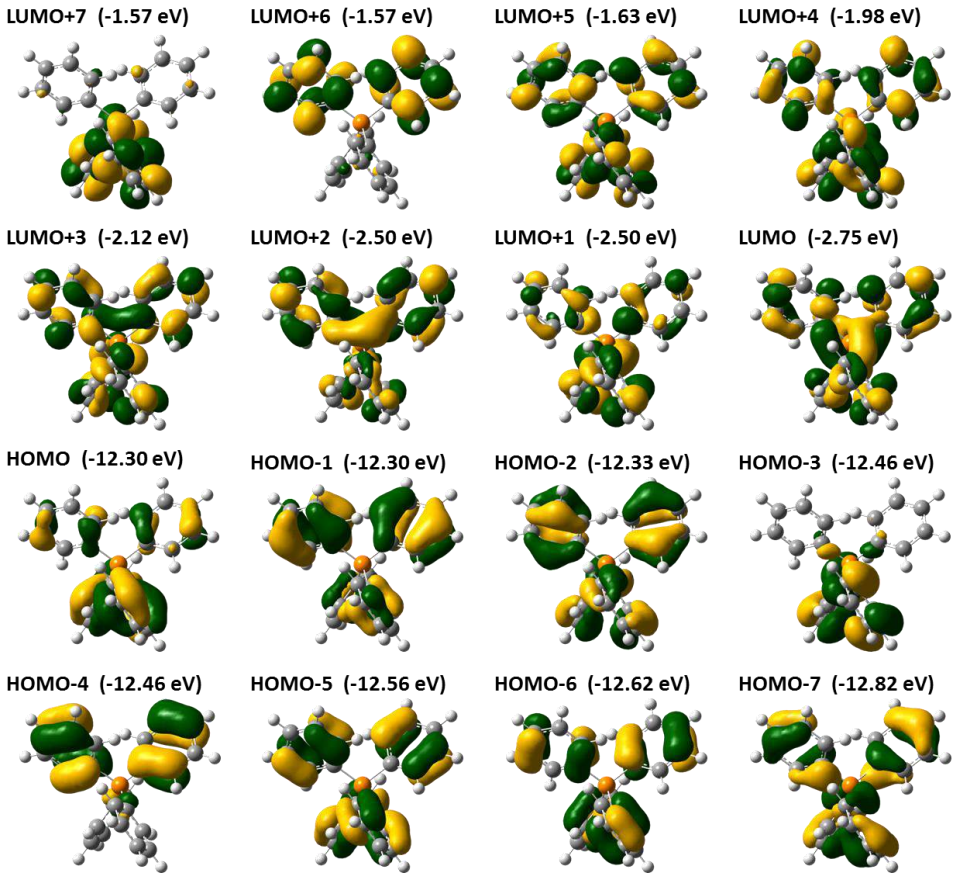

Figure 6.2. First several frontier molecular orbitals and energies of PPh_4^+ at the ωB97XD/cc-pVDZ level.

Because the couplings between the orbitals on different phenyl rings are small, the energetic spacing within each of these sets of eight MOs is small enough to effectively form bands of occupied and unoccupied π-orbitals, as shown in Figure 6.3. This energetic spacing is substantially different from that seen in most linear conjugated systems, which (as detailed in the Introduction) typically have significant energetic gaps separating the first several occupied and unoccupied MOs. Since the central atom has little contribution to the frontier MOs, the HOMO-LUMO gap is relatively unaffected by changes to the central atom and varies only between 9.44 eV (B^-) and 9.61 eV (N^+) within the series.

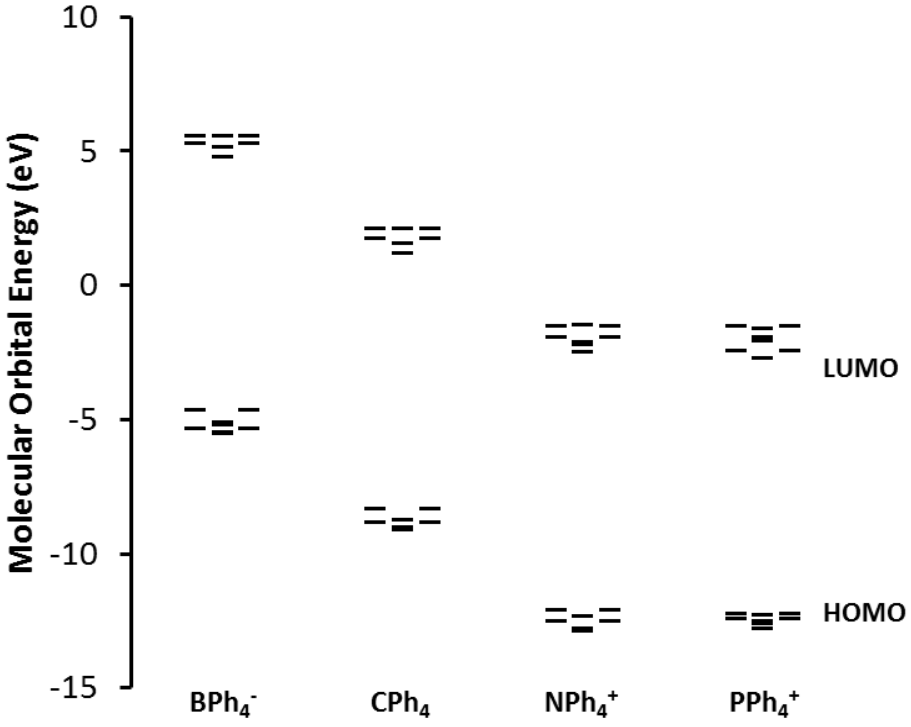

Figure 6.3. Molecular orbital energies (HOMO-7 through LUMO+7) in the XPh_4 series.

6.3.2. Excited-state properties

We turn now to the excited-state energies, CI compositions, and state-dipole and transition-dipole moments. This discussion will center on how the first several frontier MOs determine the low-lying excited state properties. As the MOs and excited-state properties do not change substantially among the members of this series, we will focus on PPh_4^+. Because the frontier MOs have band-like energetic spacing as discussed in the previous section, the compositions of the XPh_4 excited states are much more complex than those of typical linear conjugated systems. The first several excited states have little one-photon or two-photon activity; instead, the optical and NLO properties are dependent on many higher-lying states, as will be discussed in detail in the following paragraphs. Evaluating the general trends in the energies and transition dipole moments among many excited states is critical to understanding the molecular optical and NLO properties.

Because of the relatively small energetic gaps among the first eight HOMOs and the first eight LUMOs, the single-electron excitations within this range of molecular orbitals are all relatively similar in energy (a total of 64 single excitations) and are energetically well-separated from any other excitations within the π-system. The first 40-60 excited states are composed of linear combinations of these low-lying single excitations, with negligibly small contributions from higher-energy excitations (Table 6.1). Each excited state is composed of a linear combination of many single excitations; in only a few excited states does any one excitation compose more than 30% of the state electronic configuration (CI coefficient = 0.55).

Table 6.1. State energies, key dipole moment parameters, and CI composition of excited states of PPh_4^+; all excited states within the first 100 states with $\mu_{ge} > 4$ Debye are listed, and *x*, *y*, and *z* denote the molecular axes, where *z* is the axis of symmetry.

State	Energy (eV)	$\Delta\mu_{eg}$ (Debye)	μ_{ge} (Debye)	CI composition
17	6.44	-0.57 *z*	-5.47 *x* – 0.28 *y*	$-0.32\|H-4\rightarrow L+4\rangle - 0.32\|H-4\rightarrow L+5\rangle + 0.43\|H-1\rightarrow L\rangle - 0.32\|H\rightarrow L+1\rangle$
18	6.44	0.57 *z*	0.28 *x* – 5.47 *y*	$-0.32\|H-4\rightarrow L+4\rangle - 0.32\|H-4\rightarrow L+5\rangle + 0.32\|H-1\rightarrow L+1\rangle + 0.43\|H\rightarrow L\rangle$
19	6.45	0	-6.80 *z*	$+0.34\|H-6\rightarrow L+5\rangle - 0.33\|H-4\rightarrow L+7\rangle + 0.33\|H-3\rightarrow L+6\rangle - 0.34\|H-2\rightarrow L+4\rangle$
20	6.47	-6.27 *z*	-5.94 *x* – 3.93 *y*	$-0.53\|H-1\rightarrow L\rangle - 0.42\|H-1\rightarrow L+1\rangle$
21	6.47	6.27 *z*	-3.93 *x* + 5.94 *y*	$+0.53\|H\rightarrow L\rangle - 0.42\|H\rightarrow L+1\rangle$
31	6.82	0	-5.40 *z*	$+0.50\|H-5\rightarrow L\rangle - 0.36\|H-4\rightarrow L+3\rangle + 0.36\|H-3\rightarrow L+2\rangle$

We note that the excited states exhibit symmetry-breaking if their geometries are allowed to relax. In particular, at the CIS level, the C_1-optimized structure of the first excited state is stabilized by 0.1 eV as compared to the S_4-optimized geometry. The geometric changes in the C_1 geometry suggest that the excitation becomes localized primarily on one phenyl ring; one P-C bond is shortened by 0.04 Å and the C-C bonds in that phenyl ring are lengthened by 0.03 Å relative to the other three phenyl rings. However, the electronic NLO processes occur substantially faster than geometric relaxation and involve the excited states as virtual states. Thus, here we will focus solely on the excited-state properties in the S_4 ground-state geometry.

To understand the state dipole moments and the transition dipole moments, we first consider the contributions of the pure single-electron excitations, then consider the effect of the linear combinations of excitations in the excited states. We turn first to the state dipole moments. In the ground state, the S_4 molecular symmetry implies that the dipole

moment μ_g is zero;[30] thus, the difference $\Delta\mu_{eg}$ between the excited-state and ground-state dipole moments is equal to the excited-state dipole moment μ_e. The excited-state dipole moments depend on the electron distribution, related to the molecular orbital spatial distributions. Since most of the molecular orbitals are symmetrically distributed across the molecule, the single excitations between these orbitals do not change the molecular dipole moment. However, in transitions involving molecular orbitals in degenerate pairs, the two transitions involving each orbital in the pair will have state dipole moments along the molecular *z* axis that are equal in magnitude but opposite in sign.

The excited-state dipole moments μ_e can be considered as weighted sums of the changes in the state dipole moment due to each component electron configuration. In the excited states with no contribution from excitations involving degenerate orbitals, all excitations have contributions of zero to μ_e, so $\mu_e = 0$. If the contributions from pairs of degenerate excitations are equal in magnitude, the contributions to the state dipole moment cancel and $\mu_e = 0$. However, if the contributions from degenerate excitations are not equal, as occurs in pairs of degenerate excited states, μ_e can be as large as 6 Debye; within each pair of degenerate states, the two μ_e values are equal in magnitude but opposite in sign.

For each excited state *e*, the transition dipole moment μ_{ge} to the ground state is likewise composed of a linear combination of contributions from each component excitation. As was discussed previously, the first 8 HOMOs are composed of linear combinations of the phenyl orbitals that have one node within each phenyl ring, whereas the first 8 LUMOs are composed of linear combinations of the phenyl orbitals that have two nodes within

each phenyl ring. In each excitation from one of the first 8 HOMOs to one of the first 8 LUMOs, the differing number of nodes within each phenyl ring implies that each ring has some atoms where the transition density has a positive sign and some where the transition density has a negative sign. The cancellation of positive and negative transition densities within each phenyl ring limits the magnitude of the orbital transition dipole moments. The orbital components of the transition dipole moments are therefore relatively small, ranging from 0-4 Debye,[31] and may be aligned either along the molecular *z* axis or in the *xy* plane.

Since the low-lying excited states are composed of single excitations, the transitions from the ground state to each CI component in each excited state all involve electron configurations that are different by one orbital. Thus, the transition dipole moments μ_{ge} can be computed as linear combinations of the transition dipole moments of all component excitations. Depending on the signs of the CI coefficients and the orbital transition dipole moments, the components can combine additively or subtractively. Several excited states have significant μ_{ge} (Table 6.1); as will be detailed later, these states have the most significant contributions to the optical and NLO properties. Notably, there are states with large μ_{ge} both along the molecular *z* axis and in the *xy* plane. This is different from typical linear conjugated molecules, which commonly have only one low-lying excited state that is significantly coupled to the ground state.[6]

The transition dipole moments $\mu_{ee'}$ between excited states involve linear combinations of transitions between singly-excited electron configurations. Since only transitions between

configurations that differ by no more than one orbital can have non-zero contributions to the transition dipole moment, only configuration pairs in which the excitations involve either the same occupied orbital or the same unoccupied orbital can contribute to $\mu_{ee'}$. An allowed transition between two singly excited configurations therefore involves a one-electron transition either within the occupied manifold or within the unoccupied manifold. The transitions between two HOMOs or between two LUMOs can have much larger orbital transition dipole moments than the transitions between one HOMO and one LUMO because the transition densities within each ring can all contribute with the same sign to the transition dipole moment. The orbital components of the transition dipole moments range from 0 to 9 Debye, up to a factor of two larger than for the HOMO-LUMO transitions; as discussed previously, these components can be aligned either along the *z* axis or in the *xy* plane.

Even though the orbital contributions to $\mu_{ee'}$ are large, the significant mixing of excitations in each excited state limits the magnitude of $\mu_{ee'}$. Most pairs of excitations differ by two orbitals and have no contribution to $\mu_{ee'}$. In configuration pairs that do contribute to $\mu_{ee'}$, the orbital component is multiplied by two relatively small CI coefficients (as noted previously, typically < 0.55), so only infrequently does any one configuration pair contribute more than 1 Debye to $\mu_{ee'}$. In transitions with multiple configuration pairs contributing to $\mu_{ee'}$, the terms may contribute additively or subtractively. Critically, the excited states that are strongly coupled to the ground state have few large transition dipole moments to other excited states (Table 6.2). This weak coupling between excited states implies that there is relatively little TPA in these

systems; as will be described in the following section, this also has important implications in determining the sign of Re(γ).

Table 6.2. Transition dipole moments between excited states in PPh_4^+; all transition dipole moments greater than 4 Debye from the states listed in Table 6.1 to other excited states are listed.

Transition	$\mu_{ee'}$ (Debye)
19 → 25	4.94 *z*
20 → 23	5.50 *z*
20 → 25	2.76 *x* + 3.44 *y*
21 → 24	5.50 *z*
21 → 25	3.44 *x* – 2.76 *y*

6.3.3. Nonlinear optical properties

We can understand the negative sign of Re(γ) in terms of the excited state energies, state dipole moments, and transition dipole moments. Here, we focus on Re(γ) at the static (zero-frequency) limit. As mentioned previously, since there are several excited states with large coupling to the ground state along different molecular axes, the commonly-used essential-state model cannot be applied to these systems. Instead, we discuss the NLO properties in terms of the full SOS expression (Equation 1.14). Although the expression appears complicated, we recall that each term consists of a product of four transition dipole moment or state dipole moment terms in the numerator and a product of three state energy terms in the denominator.

To provide insight into the origins of the NLO properties, we decompose γ into contributions from each one-photon state in the SOS expression. As Im(γ) is negligibly small at the static limit, we focus solely on Re(γ). The Re(γ) values presented here are orientationally averaged as described in Eqn. 6.1; unlike in linear conjugated systems, the

total Re(γ) is nearly isotropic in these systems because there are large μ_{ge} terms along all three molecular axes. As shown in Table 6.3, Re(γ) contains significant contributions from a number of excited states, particularly those that are strongly coupled to the ground state.

Table 6.3. Re(γ) and its major state components and term decomposition of PPh_4^+ (power series expansion; x 10^{-36} esu). All states with total contributions > 2 x 10^{-36} esu are included.

State	Total	D	T	N
17	-3.3	0.0	0.7	-4.0
18	-3.3	0.0	0.7	-4.0
19	-5.4	0.0	0.7	-6.1
20	-5.9	0.5	0.2	-6.6
21	-5.9	0.5	0.2	-6.6
31	-3.2	0.0	0.3	-3.5
Total	-39.8	1.1	2.1	-43.0

We also consider the contributions to Re(γ) from each of the three terms as decomposed in the essential-state model. Because the excited states with significant contributions to Re(γ) all fall within a relatively narrow energy window, the denominators of all terms are similar in magnitude and we focus on the numerators. The second summation in the full SOS expression (corresponding to the **N** term in the essential-state model) contains a product of four μ_{ge} terms in the numerator. Although the essential-state model simplifies this term to the form $-\mu_{ge}^4/E_{ge}^3$, the full SOS expression also includes terms of the form $-(\mu_{gu}^2\,\mu_{gw}^2)/(E_{gu}^2\,E_{gw})$, where *u* and *w* are both excited states. When multiple excited states are significantly coupled to the ground state, these cross-terms substantially increase the magnitude of the **N** term. Because the XPh_4 systems have several excited states that are coupled to the ground state, these terms have a significant negative contribution to Re(γ).

The first summation in the SOS expression has an additional dependence on the transition dipole moments $\mu_{ee'}$ between excited states (**T** term) and the state dipole moments $\Delta\mu_{eg}$ (**D** term). Since the states with significant coupling to the ground state have small $\Delta\mu_{eg}$ and few large couplings to other excited states, these terms are at least an order of magnitude smaller than the **N** term. Because the **N** term has the dominant contribution in the SOS expression, Re(γ) is negative. This behavior is substantially different from that commonly seen in π-conjugated systems, where large couplings between the excited states generally cause the **T** term to dominate and Re(γ) to be positive.[32-35]

Although this discussion has focused on PPh_4^+, the optical and NLO properties of all four members of the XPh_4 series are largely similar. The energetic spacing of the first several frontier MOs is largely unaffected by the identity of the central atom, so a similar mixing of many excitations in the low-lying excited states is observed. The four systems have very similar NLO properties, with many states contributing significantly to Re(γ). The NLO properties are dependent on the spatial distribution and band-like energetic spacing of the first several frontier MOs, not on the identity of the central atom.

Table 6.4. Re(γ) and its term decomposition for the XPh_4 series

Central Atom	**Re(γ) (x 10^{-36} esu)**			
	Total	**D**	**T**	**N**
B^-	-44.2	0.7	5.8	-50.6
C	-42.0	1.0	6.8	-49.8
N^+	-39.3	1.7	6.2	-47.2
P^+	-39.8	1.1	2.1	-43.0

6.4. Conclusions

Although a negative Re(γ) is advantageous for device applications, very few classes of molecules studied to date have negative Re(γ). Here, we provide a theoretical understanding of the negative Re(γ) in molecules of the form XPh_4 in terms of the molecular orbitals and excited states. Unlike in typical linear conjugated systems, the NLO properties of the XPh_4 series depend on a band of several tens of low-lying excited states, of which several excited states are significantly coupled to the ground state. Since the π-systems are inherently three-dimensional, Re(γ) is nearly isotropic, in contrast with typical linear conjugated systems that have significant nonlinearity primarily along one molecular axis. Because of the complexity of the excited-state properties, the NLO properties must be understood in terms of the full SOS expression and cannot be simplified in terms of the commonly-used essential-state model, which only considers one excited state coupled to the ground state and dipole moment terms along one molecular axis. Although the magnitude of Re(γ) is relatively small, the discovery of a new molecular architecture offering the potential for a negative Re(γ) provides new molecular design approaches to achieve a large negative Re(γ) for device applications.

6.5. References

(1) Chiao, R.; Garmire, E.; Townes, C. *Phys. Rev. Lett.* **1964**, *13*, 479.

(2) Kelley, P. *Phys. Rev. Lett.* **1965**, *15*, 1005.

(3) Lallemand, P.; Bloembergen, N. *Phys. Rev. Lett.* **1965**, *15*, 1010.

(4) Kashyap, R.; Blow, K. J. *Electron. Lett.* **1988**, *24*, 47.

(5) Marder, S. R.; Gorman, C. B.; Meyers, F.; Perry, J. W.; Bourhill, G.; Brédas, J. L.; Pierce, B. M. *Science* **1994**, *265*, 632.

(6) Meyers, F.; Marder, S. R.; Pierce, B. M.; Bredas, J. L. *J. Am. Chem. Soc.* **1994**, *116*, 10703.

(7) Yang, M.; Jiang, Y. *Chem. Phys.* **2001**, *274*, 121.

(8) Yang, M.; Jiang, Y. *Phys. Chem. Chem. Phys.* **2001**, *3*, 4213.

(9) Guo, S.-L.; Li, T.-P.; Wang, T.-B.; Liu, Z.-S.; Cao, T.-D. *Opt. Mater.* **2007**, *29*, 494.

(10) Prabhakar, C.; Yesudas, K.; Bhanuprakash, K.; Jayathirtha Rao, V.; Sai Santosh Kumar, R.; Narayana Rao, D. *J. Phys. Chem. C* **2008**, *112*, 13272.

(11) Dirk, C. W.; Herndon, W. C.; Cervantes-Lee, F.; Selnau, H.; Martinez, S.; Kalamegham, P.; Tan, A.; Campos, G.; Velez, M.; Zyss, J.; Ledoux, I.; Cheng, L.-T. *J. Am. Chem. Soc.* **1995**, *117*, 2214.

(12) Whittall, I. R.; Humphrey, M. G. *Organometallics* **1995**, *14*, 5493.

(13) Letard, J.-F.; Montant, S.; Guionneau, P.; Martin, P.; Le Calvez, A.; Freysz, E.; Chasseau, D.; Lapouyade, R.; Kahn, O. *Chem. Commun.* **1997**, *1997*, 745.

(14) Diaz-Garcia, M. A.; Ledoux, I.; Duro, J. A.; Torres, T.; Agullo-Lopez, F.; Zyss, J. *J. Phys. Chem.* **1994**, *98*, 8761.

(15) DeSalvo, R.; Said, A. A.; Hagan, D. J.; VanStryland, E. W.; SheikBahae, M. *IEEE J. Quant. Electron.* **1996**, *32*, 1324.

(16) Tanaka, K. *J. Mater. Sci. - Mater. Electron.* **2005**, *16*, 633.

(17) Marder, S. R.; Perry, J. W.; Bourhill, G.; Gorman, C. B.; Tiemann, B. G.; Mansour, K. *Science* **1993**, *261*, 186.

(18) Wernke, W.; Pfeiffer, M.; Johr, T.; Lau, A.; Grahn, W.; Johannes, H.-H.; Dahne, L. *Chem. Phys.* **1997**, *216*, 337.

(19) Mukhopadhyay, S.; Risko, C.; Marder, S. R.; Brédas, J.-L. *Chem. Sci.* **2012**, *3*, 3103.

(20) Chai, J.-D.; Head-Gordon, M. *Phys. Chem. Chem. Phys.* **2008**, *10*, 6615.

(21) Chai, J.-D.; Head-Gordon, M. *J. Chem. Phys.* **2008**, *128*, 084106.

(22) Dunning, T. H. *The Journal of Chemical Physics* **1989**, *90*, 1007.

(23) Gaussian 09, Revision B.01, M. J. Frisch, G. W. Trucks, H. B. Schlegel, G. E. Scuseria, M. A. Robb, J. R. Cheeseman, G. Scalmani, V. Barone, B. Mennucci, G. A. Petersson, H. Nakatsuji, M. Caricato, X. Li, H. P. Hratchian, A. F. Izmaylov, J. Bloino, G. Zheng, J. L. Sonnenberg, M. Hada, M. Ehara, K. Toyota, R. Fukuda, J. Hasegawa, M. Ishida, T. Nakajima, Y. Honda, O. Kitao, H. Nakai, T. Vreven, J. A. Montgomery, Jr., J. E. Peralta, F. Ogliaro, M. Bearpark, J. J. Heyd, E. Brothers, K. N. Kudin, V. N. Staroverov, T. Keith, R. Kobayashi, J. Normand, K. Raghavachari, A. Rendell, J. C. Burant, S. S. Iyengar, J. Tomasi, M. Cossi, N. Rega, J. M. Millam, M. Klene, J. E. Knox, J. B. Cross, V. Bakken, C. Adamo, J. Jaramillo, R. Gomperts, R. E. Stratmann, O. Yazyev, A. J. Austin, R. Cammi, C. Pomelli, J. W. Ochterski, R. L. Martin, K. Morokuma, V. G. Zakrzewski, G. A. Voth, P. Salvador, J. J. Dannenberg, S. Dapprich, A. D. Daniels, O. Farkas, J. B. Foresman, J. V. Ortiz, J. Cioslowski, and D. J. Fox, Gaussian, Inc., Wallingford CT, 2010.

(24) Gieseking, R. L.; Mukhopadhyay, S.; Risko, C.; Brédas, J.-L. *ACS Photonics* **2014**, *1*, 261.

(25) Zojer, E.; Beljonne, D.; Kogej, T.; Vogel, H.; Marder, S. R.; Perry, J. W.; Brédas, J. L. *J. Chem. Phys.* **2002**, *116*, 3646.

(26) Zojer, E.; Beljonne, D.; Pacher, P.; Bredas, J. L. *Chem. Eur. J.* **2004**, *10*, 2668.

(27) Cave, R. J.; Davidson, E. R. *J. Phys. Chem.* **1988**, *92*, 614.

(28) Cave, R. J.; Davidson, E. R. *J. Phys. Chem.* **1987**, *91*, 4481.

(29) Yang, M.; Jiang, Y. *Chemical Physics* **2001**, *274*, 121.

(30) In charged systems, the state dipole moments depend on the choice of the origin; however, the differences between state dipole moments do not so long as the same origin is used for both state dipole moments. We select the location of the central atom X as the origin; since the molecules have S4 symmetry, this is also the center of charge.

(31) The orbital components of the transition dipole moments discussed here include a quantum prefactor of sqrt(2) because the INDO/CI approach uses singlet-adapted states.

(32) Nalwa, H. S. *Adv. Mater.* **1993**, *5*, 341.

(33) Tykwinski, R. R.; Gubler, U.; Martin, R. E.; Diederich, F.; Bosshard, C.; Gunter, P. *J. Phys. Chem. B* **1998**, *102*, 4451.

(34) Gubler, U.; Bosshard, C. *Adv. Polym. Sci.* **2002**, *158*, 123.

(35) Bredas, J. L.; Adant, C.; Tackx, P.; Persoons, A.; Pierce, B. M. *Chem. Rev.* **1994**, *94*, 243.

CHAPTER 7

MOLECULAR DYNAMICS STUDIES OF POLYMETHINE AGGREGATION IN THE SOLID STATE

7.1. Introduction

Although some polymethines have very large |Re(γ)| values and figures-of-merit in dilute solution,[1] these properties are typically lost at large concentrations due to both polymethine-counterion and polymethine-polymethine interactions.[2] Thus, to develop polymethine-based materials for AOS applications, polymethine aggregation must be minimized at large chromophore concentrations. To achieve this aim, understanding the geometric and electronic structures of polymethine-counterion and polymethine-polymethine interactions in the bulk is critical. However, little is known, in particular from a theoretical perspective, as to how polymethine aggregation influences the optical properties;[2-6] *e.g.*, electronic-structure calculations have generally been limited to small aggregates[2] and as such do not include the packing effects related to having many polymethines and counterions in close proximity. Although two-level and minimum-state models have shown size-enhancement of $\chi^{(3)}$ and two-photon absorption in ordered molecular aggregates,[7,8] these models neglect the disorder effects typical of polymethine thin films.

Here, we introduce a theoretical approach that makes use of molecular dynamics (MD) simulations to investigate the aggregate structures of simple streptocyanines[2,9-13] (Figure

7.1) and of thiopyrylium polymethines with bulky substituents[1,14] (Figure 7.2) in thin-film-like, amorphous morphologies. We focus in particular on the distribution of geometric structures of polymethine-counterion and polymethine-polymethine pair interactions. The results of the MD simulations are then combined with electronic-structure calculations to examine the impact of the packing motifs on intermolecular electronic couplings. Since aggregation dramatically affects the thin-film NLO properties, understanding and controlling aggregation is critical to develop materials with bulk NLO properties suitable for AOS applications.

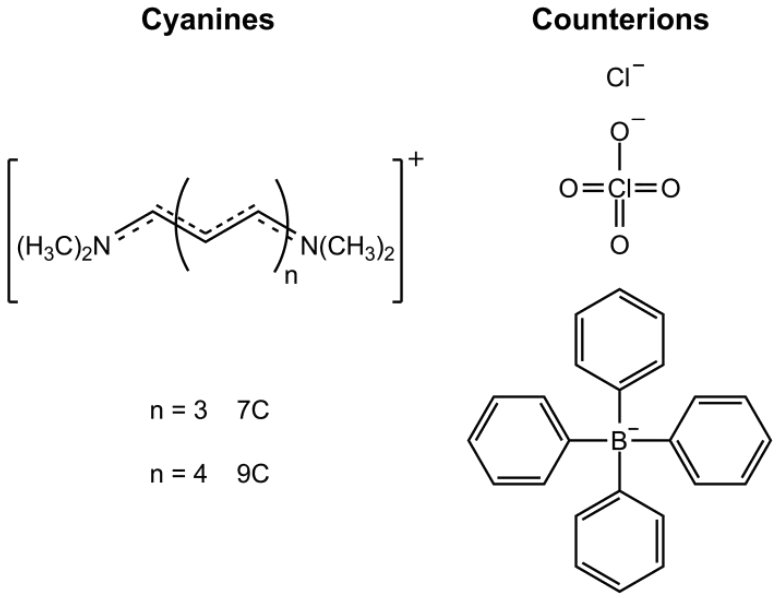

Figure 7.1. Molecular structures of the 7-carbon (7C) and 9-carbon (9C) streptocyanines and the Cl^-, ClO_4^-, and BPh_4^- counterions studied here.

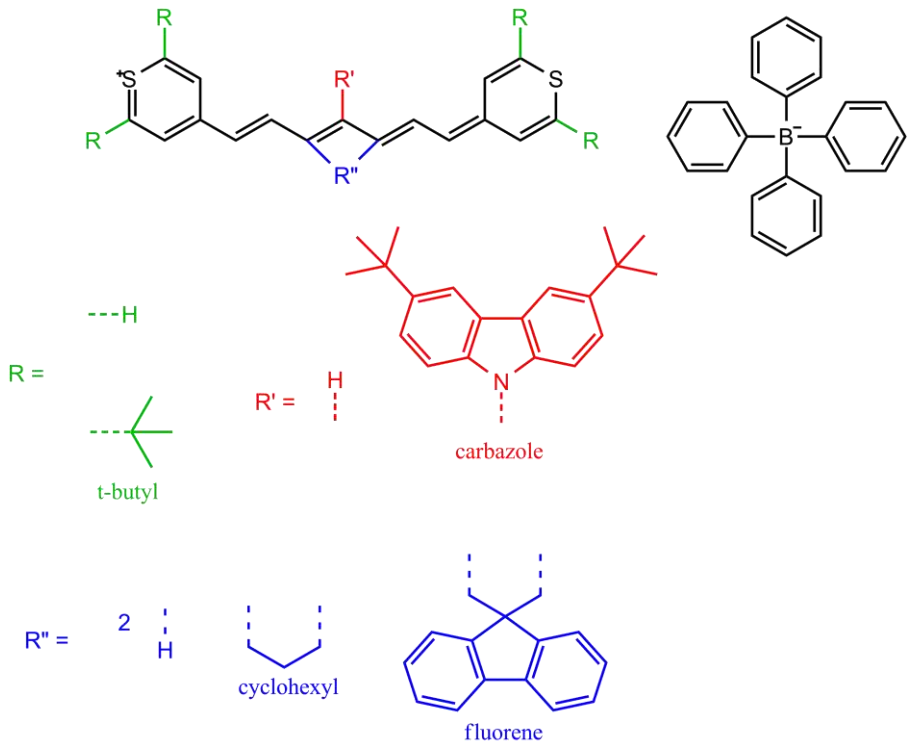

Compd.	R	R'	R"	Conc. (M)	# pairs/ simulation	Box size (nm^3)	# simus
1	-H	-H	2 -H	1.83	500	453	3
2	-H	carbazole	cyclohexyl	1.15	300	432	4
3	-H	-H	fluorene	1.40	400	473	3
4	-H	carbazole	fluorene	1.00	275	455	5
5	t-butyl	-H	cyclohexyl	1.14	300	436	4
6	t-butyl	carbazole	cyclohexyl	0.87	225	430	5
7	t-butyl	-H	fluorene	0.99	250	419	5
8	t-butyl	carbazole	fluorene	0.78	200	427	6

Figure 7.2. Chemical structures and bulk concentrations of the polymethine dyes and BPh_4^- counterion studied here. R denotes the substituents on the polymethine ends; R', on the center front; and R", on the center back.

7.2. Theoretical Methodology

7.2.1. Force field

Atomistic molecular dynamics (MD) simulations were performed using the OPLS-AA force field[15] in the GROMACS 4.5.4 package,[16] which has previously shown good

agreement with experiment for polymethine aggregates.[3] Initial polymethine and counterion geometries were obtained via geometry optimization using a density functional theory (DFT) approach with the ωB97XD functional[17,18] and cc-pVDZ basis set,[19] as implemented in the Gaussian 09 (Rev. B.01) suite of programs.[20] We note that torsions about all C-C bonds in the polymethine backbone were restrained to within 10° of planarity during the MD simulations so as to prevent *trans-cis* isomerization during high-temperature annealing; although this isomerization can occur through a photoisomerization process,[21] the energetic barrier to rotation is large in the ground state.[22]

The atomic charges used in the MD simulations were obtained from natural bond order (NBO) calculations at the ωB97XD/cc-pVDZ level. The charges for the counterions and symmetric polymethine were obtained for isolated molecules. To obtain an asymmetric streptocyanine charge distribution, the geometry of a streptocyanine/Cl^- complex with the counterion localized near one end of the polymethine was first optimized at the ωB97XD/cc-pVDZ level, followed by an NBO calculation at the same level of theory; the electric field of the counterion partially localizes the polymethine charge near one end of the molecular structure. Since this calculation provides a charge of +0.85 |e| on the polymethine, the charge on the polymethine was normalized to +1 by distributing the remaining +0.15 |e| positive charge equally among all atoms in the π system so that both the polymethine and the counterion bear unit charges in the MD simulations.

7.2.2. Crystal molecular dynamics simulations

Crystal structures obtained from the Cambridge Structural Database (CSD; identification codes noted within parentheses) were used to generate initial geometries without any modification. For the seven-carbon (7C) streptocyanine with the BPh_4^- counterion (YOHRES)[23] and two polymethine-counterion pairs per unit cell, a supercell consisting of 6x6x6 unit cells was constructed; for the 9C streptocyanine with the ClO_4^- counterion (NEQHUN) and the 9C streptocyanine with the BPh_4^- counterion (NEQHEX), both with four polymethine-counterion pairs per unit cell, a supercell of size 5x5x5 was constructed. The number of polymethine-counterion pairs were 432 (6x6x6) and 500 (5x5x5), respectively. Atomic charges were derived from NBO calculations at the ωB97XD/cc-pVDZ level for a symmetric charge distribution as discussed previously.

An initial energy minimization was performed and followed by simulation over 1.5 ns at 300 K under the NPT ensemble. The box parameters were averaged over the final 1 ns. For all simulations, periodic boundary conditions, the Parrinello-Rahman barostat under an isotropic pressure of 1 bar, and the Nose-Hoover thermostat were used. For van der Waals interactions, a spherical cutoff of 0.9 nm was used, and the Ewald summation was used for Coulomb interactions. These simulations were provided by Stephen Shiring.

7.2.3. Single-complex calculations

Several energetic local minima for the 9C streptocyanine/Cl^- complex were obtained at the ωB97XD/cc-pVDZ level, using the basis set superposition error (BSSE) correction; the minima were confirmed by the absence of imaginary frequencies. Several C_{2v}

structures were also optimized using symmetry constraints; these stationary points had imaginary frequencies corresponding to displacement of the counterion along the long axis of the polymethine.

Several local minima were also obtained at the MM level using the modified OPLS-AA force field. The minima were found by minimizing the energy of the polymethine-counterion complex starting from a series of geometries with the counterion displaced by various distances along the length of the polymethine backbone. Periodic boundary conditions were used, and the polymethine-counterion complex was placed in a cubic box with side lengths of 5 nm to prevent spurious interactions between the complex and its images in other unit cells. A spherical cutoff of 0.9 nm was used for the summation of van der Waals interactions, and the Ewald summation was used for Coulomb interactions. Both symmetric and asymmetric polymethine charge distributions were considered. To obtain the minima with the counterion near the center of the polymethine backbone, the motion of the central carbon and hydrogen atoms of the polymethine and of the chloride counterion were restrained in the directions of the polymethine long axis and π plane such that only the distances between the atoms were free to change.

7.2.4. Molecular dynamics simulations on amorphous structures

Initial configurations were constructed by randomly placing the polymethines and counterions in a cubic periodic box; the total number of polymethine/counterion pairs was 500 for the streptocyanines and was varied to maintain a total number of atoms on the order of 40,000 for the substituted thiopyrylium polymethines (the complete list of

number of polymethines/counterion pairs per simulation, equilibrated system volume, and number of simulations is provided in Figure 7.2). The energy was then minimized at constant volume, followed by an initial run of 10 ps at 50 K under the NVT ensemble using a time step of 0.5 fs to avoid atomic overlap. The simulation box was then equilibrated above the glass transition temperature (at 900 K for the streptocyanines and 800 K for the thiopyrylium polymethines; initial simulations suggest that the glass transition temperature for the 9C streptocyanine/Cl^- system is around 760 K) under the NPT ensemble until the volume equilibrated and for several additional ns using the Berendsen barostat under an isotropic pressure of 1 bar. Three or more configurations at 1 ns intervals were extracted from this simulation to obtain a series of independent amorphous morphologies. These configurations were then equilibrated for 1 ns at the aforementioned high temperature using the Parrinello-Rahman barostat under an isotropic pressure of 1 bar, cooled over 2 ns to 300 K, and simulated for 1 ns at 300 K. The final 1 ns of this simulation was used for analysis. For all simulations, the Nose-Hoover thermostat and periodic boundary conditions were used, and the time step was 1 fs unless otherwise specified. A spherical cutoff of 0.9 nm was used for the summation of van der Waals interactions, and the Ewald summation was used for Coulomb interactions. For all polymethines, the results were averaged over enough simulations to obtain a total of at least 1200 polymethine-counterion complexes. The bulk concentration of polymethines was computed as:

[(# polymethines) / (average box volume at 300 K)]

and then converted to molarity. Some of the simulations for thiopyrylium polymethines **2**-**4** were provided by Sukrit Mukhopadhyay.

7.2.4.1. Analysis of polymethine-counterion geometries

The polymethine-counterion geometries were analyzed by defining an internal coordinate system based on the positions of two terminal atoms and one central atom of the polymethine (for streptocyanines, the two nitrogens and the hydrogen bonded to the central carbon; for thiopyrylium polymethines, the two sulfurs and the central carbon). The geometric center of the two terminal atoms was defined as the origin C, and vector **X** was defined as the normalized vector from C to the first terminal atom (see Figure 7.3). Vector **Y** was defined as the normalized component of the vector from C to the location of the central hydrogen atom orthogonal to **X**, and vector **Z** was defined as the cross-product of **X** and **Y**. For each counterion, vector **D** was defined as the vector from C to the central atom of the counterion. The dot products of **D** with vectors **X**, **Y**, and **Z** were calculated to give the displacements D_x, D_y, and D_z, respectively, along each of the three internal axes.

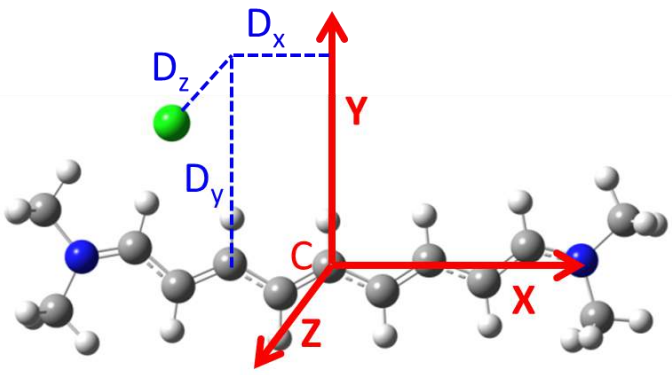

Figure 7.3. Depiction of the analysis of polymethine-counterion interaction geometries.

All polymethine-counterion pairs within the distance cutoffs of -15 Å < D_i < 15 Å (i = x, y, z) were considered and counted in bins with a width of 1 Å in each of the three

dimensions. This analysis was performed for 501 frames at 2 ps intervals throughout each simulation run and averaged over all simulations for each polymethine/counterion system. The bulk number density of polymethine-counterion pairs was calculated as:

[(# polymethines/frame) x (# counterions/frame)] / (average frame volume).

The count in each bin was normalized by dividing the count by the bin volume and by the bulk density of polymethine-counterion pairs. In the figures shown in Section 3, the values in the long-axis plots show the x and y displacements averaged over a depth ranging from –5 Å to +5 Å along the z axis; the values in the short-axis plots show the y and z displacements averaged over a depth ranging from –12 Å to +12 Å along the x axis. The plots of the probabilities show a color corresponding to the counterion position probability within each 1 Å x 1 Å square; an image of the polymethine is superimposed on the plot to provide a size scale and the orientation of the polymethine.

In the next two subsections, we detail how we analyzed the results of the MD simulations to provide insight into the characteristics of the polymethine / counterion structures in the bulk.

7.2.4.2. Analysis of polymethine aggregate structures

The polymethine-polymethine interaction geometries were analyzed by considering the positions of the terminal atoms (nitrogens in streptocyanines; terminal carbons of the polymethine bridge in thiopyrylium polymethines), as shown in Figure 7.4. For each polymethine pair A and B, vectors **A** and **B** between the two terminal atoms of each polymethine were defined, and the geometric centers C_A and C_B were set as the average

positions of the two terminal atoms of polymethines A and B, respectively. Vector **E** was taken as the vector between C_A and C_B. The offset vector **F** was defined as the projection of **E** onto **A**, and the radial distance vector **R** was defined as the projection of **E** into the plane perpendicular to **A**. The offset and the radial distance were taken as the magnitudes of vectors **F** and **R**, respectively. To determine the torsion angle θ between the two polymethines, the vector **B'** was first calculated as the projection of **B** into the plane perpendicular to **R**;[24] θ was then defined as the angle between vectors **A** and **B'**. Because the two ends of the polymethines are identical, if the angle between vectors **A** and **B'** was greater than 90°, θ was defined as (180° – the angle between **A** and **B'**). Since the offset, radial distance, and torsion angle depend on whether polymethine A or polymethine B is selected first, all ordered pairs of polymethines were considered.

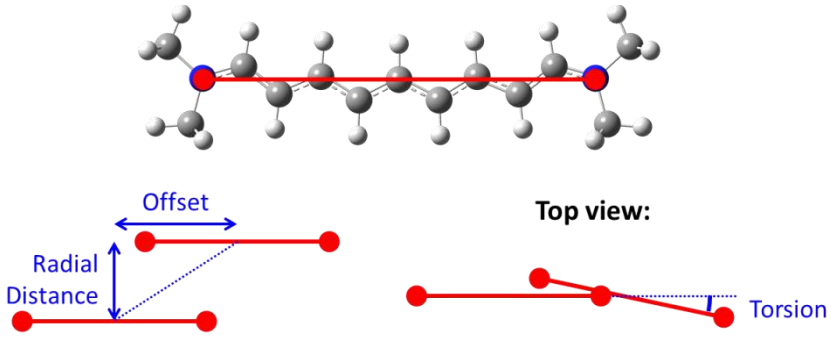

Figure 7.4. Depiction of the analysis of polymethine-polymethine interaction geometries.

All polymethine pairs with a radial distance less than 6 Å and an offset less than 10 Å (streptocyanines) or 12 Å (thiopyrylium polymethines) were considered and counted in bins with a width of 1 Å by offset and 10° by torsion angle. This analysis was performed for 501 frames at 2 ps intervals during each simulation run and averaged over all

simulation runs for each polymethine-counterion system. The bulk number density of ordered polymethine pairs was computed as:

[(# polymethines / frame) x (# polymethines / frame – 1)] / (average frame volume).

The count in each bin was normalized by dividing the count by the bin volume and by the bulk density of the polymethine pairs. The plots of probabilities show a color corresponding to the pair probability for each bin defined by a specified range of offset distances and torsion angles.

7.2.5. Electronic coupling calculations based on MD geometries

All polymethine pairs within a radial distance of 6 Å and an offset distance of 10 Å for the streptocyanines or 12 Å for the thiopyrylium polymethines (as defined in the previous section) were extracted from five frames of each simulation at an interval of 250 ps. For each pair, the electronic coupling (transfer integral) was computed using the INDO Hamiltonian[25] in the Mataga-Nishimoto parameterization.[26] The electronic couplings between the HOMOs and LUMOs were considered. The electronic coupling values were counted in bins of 10 meV width. Two separate normalization schemes were considered: (1) the count was normalized relative to the bulk density of polymethine pairs by dividing the count by the bin volume and by the bulk density of the polymethine pairs as described above, and (2) the count was normalized to the average number (expectation value) of neighbors for each polymethine by dividing the count by:

[(# of frames) x (# of polymethines / frame)] / 2.

To evaluate the time-dependence of the electronic coupling, several pairs of polymethines were selected, and the electronic coupling calculations were performed for the geometries of each pair extracted from 501 frames at a 2 ps interval throughout the simulation.

7.3. Results and Discussion

7.3.1. Streptocyanine crystals

To establish the reliability of the modified OPLS-AA force field, in particular of the charge distributions on the polymethines and counterions, NPT (constant number of molecules *N*, pressure *P*, and temperature *T*) simulations were run for a series of known streptocyanine/counterion crystal structures (Table 7.1). The experimental unit-cell parameters for streptocyanines with lengths of 7 and 9 carbon atoms (7C and 9C, respectively) are well reproduced, though the deviation with respect to experiment for one unit-cell axis in each of the 9C crystals is approximately 8%. In view of the necessary simplifications that were made for the charge distributions – e.g., the charges are taken from calculations on isolated polymethines and counterions (*i.e.*, the surrounding medium and intermolecular interactions are not taken into account) and the charges are distributed such that each unit in the complex bears unit charge – the fact that the results are comparable with experiment provide general confidence in the methodology and indicates that practical insight into aggregate structures can be obtained.

Table 7.1. Comparison of experimental unit cell parameters to MD simulation unit cell parameters; a, b, and c are in Å; α, β, γ are in degrees.

	7C			**9C**					
	BPh_4^-			**BPh_4^-**			**ClO_4^-**		
	Exp.	**MD**	**Deviation**	**Exp.**	**MD**	**Deviation**	**Exp.**	**MD**	**Deviation**
a	9.04	9.03	-0.13%	11.12	10.77	-3.10%	8.02	8.14	1.50%
b	11.69	12.12	3.65%	23.77	23.02	-3.16%	13.00	11.97	-7.88%
c	14.89	14.32	-3.81%	11.97	12.98	8.48%	15.63	15.51	-0.79%
α	73.97	72.26	-1.71°	90.00	90.01	0.01°	90.00	90.00	--
β	85.02	84.40	-0.62°	95.72	101.9	6.14°	101.4	100.3	-1.11°
γ	81.35	83.72	2.37°	90.00	90.00	--	90.00	90.00	--

At this stage, it is useful to note that, since polymethines have extremely large linear polarizabilities, the molecular charge distributions are particularly sensitive to the charges and polarizabilities of the surrounding medium. It is this sensitivity that makes polymethines particularly challenging to model using MM/MD techniques with fixed charge distributions. Because of these challenges, care should be taken in the evaluation and use of the procedure. The polymethines in the crystals considered here have bond-length alternation (BLA) patterns (defined as the average of the absolute difference in bond lengths between adjacent carbon atoms in the polymethine chain) near zero: the BLA of the 7C/BPh_4^- system is 0.014 Å, while those for the 9C/BPh_4^- and 9C/ClO_4^- systems are 0.013 Å and 0.011 Å, respectively. This implies indeed that the charge is delocalized along the whole polymethine backbone[9,27,28] and justifies the use in the present case of symmetric charge distributions on the streptocyanines.

7.3.2. Isolated streptocyanine-counterion minima

To further test the modified OPLS-AA force field, we have also compared the geometries and relative energies of the MM energetic minima for the single 9C streptocyanine/Cl^-

complexes to those obtained using density functional theory (DFT) at the ωB97XD/cc-pVDZ level. Our previous DFT calculations point out that in polymethine-counterion complexes, the charge on the polymethine does not remain symmetrically distributed but instead becomes partially localized near the end of the polymethine where the counterion is found.[2] To address the limitation of fixed charges in the OPLS-AA force field, we have considered two limiting cases: one where the polymethines have symmetric charge distributions and one where they have asymmetric charge distributions obtained from the energetic minimum of the DFT-based streptocyanine/Cl^- complex.

The DFT and MM approaches both give two distinct local minima, in each case with the counterion in the lateral plane ($D_z = 0$) of the polymethine (Table 7.2); one minimum corresponds to a positive displacement D_y of the counterion along the polymethine short axis while the other has a negative D_y. Importantly, there is good overall agreement between the DFT and MM results in terms of both geometries and relative energies. The differences seen in the D_y values are primarily due to differences in the bond angles along the polymethine backbone: the DFT structures show alternation of larger (125-127°) and smaller (115-121°) angles along the π backbone and a significant change in the angles along the polymethine backbone in response to the counterion position, subtle features that are not captured in the OPLS-AA structures. The distances from the counterion to the nearest atoms of the polymethine are very similar in the DFT and OPLS-AA structures (deviations ~ ±0.2 Å). Along the polymethine long axis, the D_x values of the local minima are somewhat smaller for OPLS-AA than for DFT, particularly in the case of the symmetric charge distribution and for the higher-energy local minimum in the case of the

asymmetric charge distribution.[29] The very large polymethine linear polarizabilities make the DFT charge distributions along the long axis highly dependent on the counterion position. Since the MM charge distribution is fixed, this may limit the extent to which the counterion is attracted toward one end of the polymethine.

Table 7.2. (Top) General geometric structures of the 9-carbon streptocyanine/Cl- system and (bottom) geometries and relative energies of the energetic minima for the streptocyanine/Cl- system.

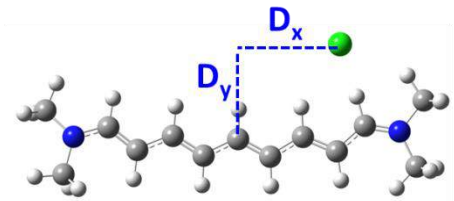

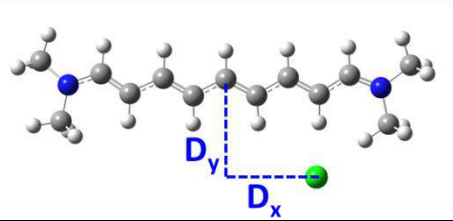

		D_x (Å)	D_y (Å)	Energy (kcal/mol)	D_x (Å)	D_y (Å)	Energy (kcal/mol)
DFT	C_{2v}	0.00	2.36	+6.1	0.00	-3.52	+14.2
	Min	3.92	3.27	0.0	3.62	-3.29	+6.7
MM (symm)	C_{2v}	0.00	3.34	+3.0	0.00	-4.00	+14.8
	Min	3.05	3.49	0.0	2.83	-3.19	+6.6
MM (asymm)	C_{2v}	0.02	3.32	+12.4	0.01	-4.03	+30.9
	Min (1)	-3.35	3.59	0.0	-3.09	-3.24	+16.1
	Min (2)	-	-	-	+2.36	-3.01	+26.2

The relative energies of the structures can be essentially understood in terms of the electrostatic polymethine-counterion interactions. The structures with positive D_y values are more stable than those with negative D_x values due to the inherent charge alternation that is present along the polymethine backbone;[30-32] indeed, the odd-numbered carbon atoms along the polymethine backbone bear a larger positive charge than the even-numbered carbon atoms. The minima with large D_x values are stabilized relative to the C_{2v} structures because the positive charge on the polymethine is then localized primarily near an end; it appears that the extent of stabilization is somewhat underestimated in the

case of the symmetric charge distribution but somewhat overestimated in the asymmetric case as compared to the DFT results. The overall agreement between the MM and DFT structures confirms that our methodology is adequate to investigate the bulk aggregation of polymethines.

7.3.3. Streptocyanine Amorphous Bulk Structures

To gain insight into aggregation in amorphous thin films, MD simulations of the amorphous bulk structures of the 9C streptocyanine were performed with Cl^- and BPh_4^- counterions. We first discuss the polymethine-counterion structures and polymethine-polymethine structures and then analyze the electronic couplings between neighboring polymethines.

7.3.3.1. Polymethine-counterion structures

In looking at the packing between the polymethines and counterions, we are especially interested in the effects of the counterion size/hardness and polymethine charge distribution. For each polymethine, the positions of all nearby counterions are considered.

In the streptocyanine/Cl^- bulk system, see Figure 7.5, the most probable positions of the counterions are close to the local minima for the streptocyanine/Cl^- complex described in the previous section (a darker color in the grid corresponds to a higher counterion probability). The counterion probability is higher near the global minimum with positive D_y values than near the higher-energy local minimum with negative D_y values. We note that since the counterion probability is averaged over a depth range roughly

corresponding to the first shell of counterions surrounding the polymethine (± 5Å for the long-axis images; ± 12Å for the short-axis images), the probability is not quite zero in the bins near the centers of the figures directly on top of the polymethine; if the depth range is decreased such that only counterions that are within 1Å of the polymethine plane are considered, the probability is exactly zero for the bins directly on top of the polymethine (Figure 7.6); however, the locations of highest counterion probability are unaffected.

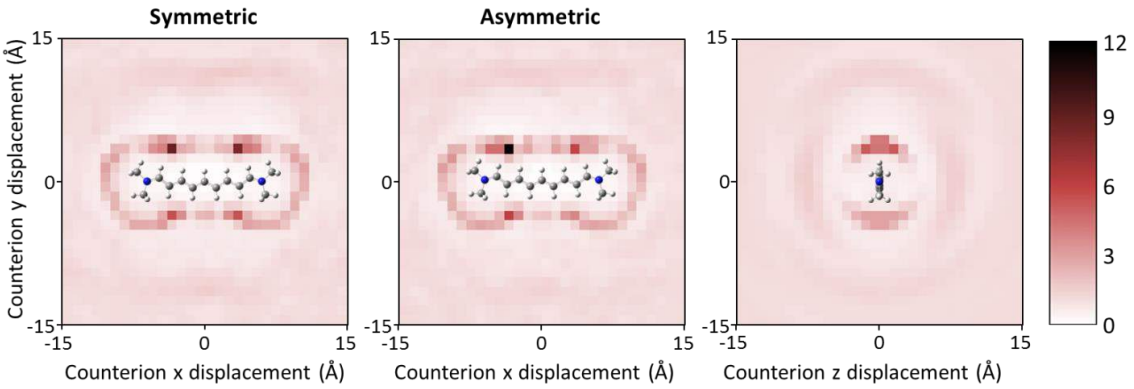

Figure 7.5. Counterion probability distribution in bulk MD simulations of the streptocyanine/Cl^- complexes. The color scale, given on the far right, corresponds to the probability of finding polymethine-Cl complexes, with a probability of one corresponding to the average bulk density of polymethine-counterion pairs.

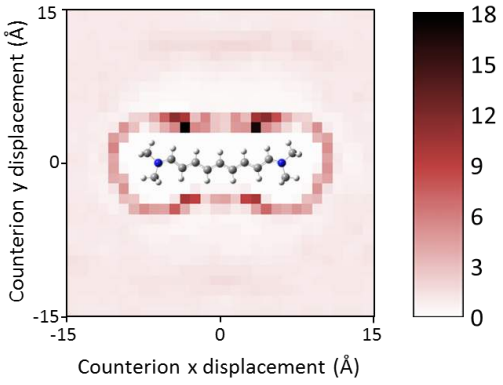

Figure 7.6. Counterion probability distribution in bulk MD simulations of the streptocyanine/Cl^- complexes. The counterion probability in each 1 Å x 1 Å square is averaged over a depth ranging from –1 Å to +1 Å.

As expected, when a symmetric polymethine charge distribution is used, the counterion probability distribution is also essentially symmetric. In the case of an asymmetric charge distribution, counterions are found twice as often near the more positively charged ($D_x < 0$) ends of the polymethines as near the opposite ends. However, the most probable positions of the counterions relative to the polymethines are essentially unchanged. Relative to the polymethine short axes, the counterions are substantially more likely to sit in or near the plane of the polymethines than to interact with the polymethine π systems, which is consistent with the local minima for the single polymethine-counterion complexes.

As the regions of highest counterion probability have geometries comparable to the DFT minima of the single streptocyanine/Cl^- complexes, such structures suggest at first sight that the counterion positions could lead to significant symmetry breaking of the polymethines. However, it must be borne in mind that in the bulk there are several counterions in close proximity to each polymethine. Thus, without taking account of the full charge environment around each polymethine, it is challenging to draw firm conclusions about the extent to which the polymethines symmetry-break in the bulk.

When the Cl^- counterions are replaced with the bulkier, chemically softer BPh_4^- counterions, several important changes in the geometries of the polymethine-counterion structures occur, see Figure 7.7. First, due to steric effects, the centers of the BPh_4^- counterions are typically about 2 Å further from the polymethine backbone than are the Cl^- counterions, though their most probable displacements along the long axis of the

polymethine are essentially unchanged. Even though the polymethine backbone is able to fit between two of the phenyl rings of the counterions, the increased steric bulk of the counterions limits aggregation. In addition, the larger counterions have a much broader distribution of positions with similar probabilities, both along the length of the polymethine (x axis) and around the polymethine short axis (yz plane). When an asymmetric polymethine charge distribution is considered, the BPh_4^- counterions are somewhat more likely to be found near the more positively charged end of the polymethine, but the probability difference is smaller than in the case of the Cl^- counterion. This is consistent with the chemically softer nature of the BPh_4^- counterion, as the charge on the counterion is distributed equally among all four phenyl rings. Thus, the polymethine-counterion proximity and broadness of the counterion probability distribution are significantly affected by the choice of the counterion.

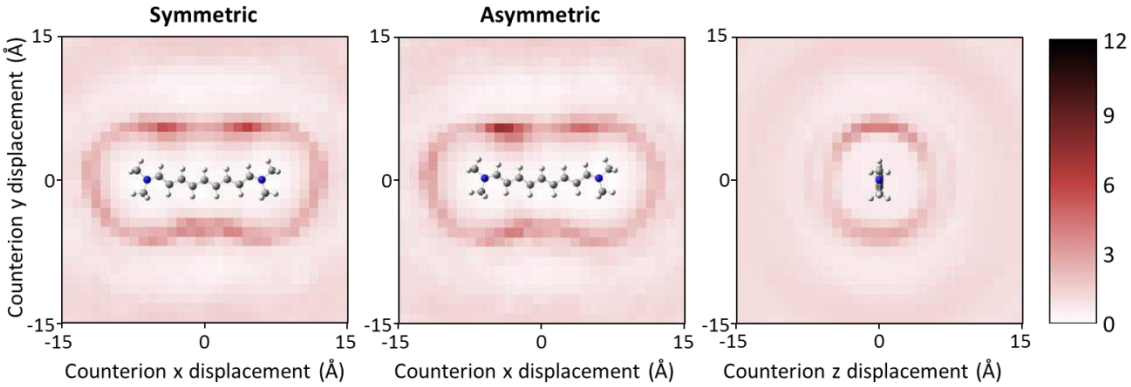

Figure 7.7. Counterion probability distribution in bulk MD simulations of the streptocyanine/BPh_4^- complexes. The color scale, given on the far right, corresponds to the probability of finding complexes, with a probability of one corresponding to the average bulk density of polymethine-counterion pairs.

7.3.3.2. Polymethine-polymethine structures

Here, we focus on the relative positions and orientations of the polymethine long axes to evaluate whether neighboring molecules are in geometries where the optical properties

are likely to be affected. According to the definitions presented in the Methodology section, polymethine neighbors with large torsion angles between their long axes correspond to perpendicular aggregates, while those with small torsion angles correspond to either H-aggregates (small longitudinal offset) or J-aggregates (large offset).

In the streptocyanine/Cl^- system, a broad distribution of aggregation geometries is seen with only slight differences in how frequently the various aggregate geometries are observed, as evidenced by the minimal differences (in color) across the full range of offset distances and torsion angles shown in Figure 7.8; the probabilities of the most and least common aggregates differ only by a factor of 2.5. The weak energetic preference observed here for any one aggregate geometry is consistent with the small energetic differences we computed at the DFT level between these structures.[2] Within the radial distance and offset cutoffs used, each polymethine has an average of 5.8 neighbors.

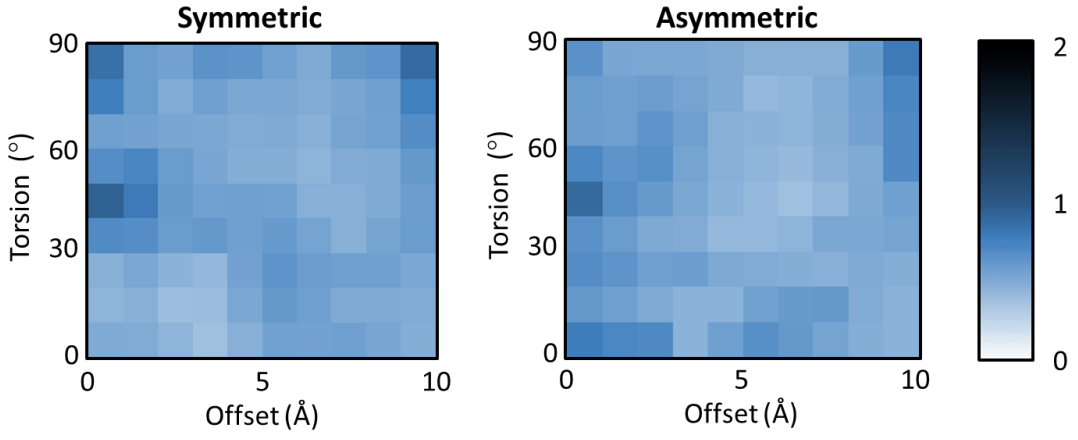

Figure 7.8. Probability distribution of aggregate geometries for the 9C streptocyanine/Cl^- complex using (left) the symmetric charge distribution and (right) the asymmetric charge distribution. The color scale, given on the far right, corresponds to the probability of finding aggregates, with a probability of one corresponding to the average bulk density of polymethine pairs.

Within the small differences in aggregate probabilities, a few trends can be observed. For both symmetric and asymmetric polymethine charge distributions, relatively large aggregate probabilities are observed in J-aggregate geometries and in structures with small offsets and torsion angles near 45°, as evidenced by the darker colors in these regions of the probability plots. Consideration of an asymmetric charge distribution slightly increases the probability of forming H-aggregates and decreases the probability of perpendicular aggregates. In such instances, the polymethine pairs in H-aggregate geometries with their dipole moments pointing in opposite directions are stabilized relative to the polymethine H-aggregates with symmetric charge distributions.

In the streptocyanine/BPh_4^- system, the polymethine aggregates also show a similar probability for aggregation in a variety of geometries, see Figure 7.8. The larger counterions effectively reduce the polymethine density, decreasing the average number of neighboring polymethines within the cutoffs from 5.8 to 2.2. In addition, the concentration of close-packed pairs relative to the bulk density of polymethine pairs is slightly smaller, as evidenced by the slightly lighter color throughout the probability plots. The most common aggregate geometries are similar to those with the Cl^- counterion: H-aggregate, J-aggregate, and perpendicular aggregate geometries all have relatively large probabilities. Unlike the aggregates with Cl^-, there is no peak in aggregate probability at torsion angles near 45°. Again, the differences between the distributions of aggregates with symmetric and asymmetric charge distributions are minor. While not easily apparent from the figures due to the amorphous nature of these systems, our

structural analysis provides an efficient way of assessing the relative probabilities of H-aggregates, J-aggregates, and perpendicular aggregates.

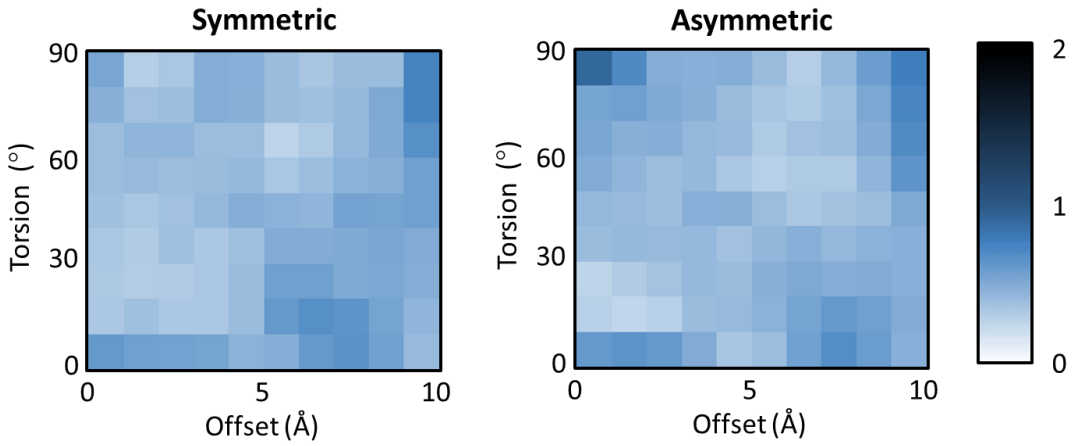

Figure 7.9. Probability distribution of aggregate geometries for the 9C streptocyanine/BPh_4^- complex using (left) the symmetric charge distribution and (right) the asymmetric charge distribution. The color scale, given on the far right, corresponds to the probability of finding aggregates, with a probability of one corresponding to the average bulk density of polymethine pairs.

The results obtained here, in terms of both polymethine-counterion and polymethine-polymethine structures, suggest that a symmetric or asymmetric character of the charge distribution on the polymethine dyes is not the dominant contribution in determining aggregate geometries. This result can be understood by the fact that the change in charge distribution creates a relatively small perturbation of the overall electrostatic interactions within the system. Even in the asymmetric charge distribution, the positive charge is not fully localized on one end of the molecule; in fact, the more positively charged half of the molecule bears roughly a +0.6 |e| charge, while the other half bears roughly a +0.4 |e| charge. Although the difference between the charge distributions is large enough to substantially change the molecular excited-state properties,[2,9] it appears to have a much smaller effect on the aggregation behavior.

7.3.3.3. Electronic couplings among polymethines

While the analysis of the polymethine aggregate structures presented above is a first step toward understanding how aggregation can affect the bulk optical properties, it neglects a key factor. By focusing solely on the polymethine long-axis orientations and relative positions, this geometric analysis does not distinguish (for example) between polymethines that are π-stacked and those that are side-by-side in the same plane. Such differences in short-axis orientations can in fact determine whether the impact of aggregation on the optical properties is large or negligibly small. Since the interactions between polymethines that lead to changes in their optical properties are inherently quantum-mechanical in nature, we now turn to a discussion of the electronic couplings among neighboring polymethine dyes, which will tell us at least qualitatively whether the transparency window between the lowest one-photon and two-photon excited states can be preserved or not.

Here, we have evaluated the electronic couplings for all polymethine pairs with an intermolecular backbone-to-center distance less than 6 Å and a longitudinal offset less than 10 Å. Since the lowest polymethine excited states primarily involve excitations within the first few frontier molecular orbitals,[2,9,13,32] large electronic couplings between these orbitals imply that the one-photon and two-photon absorption properties will be significantly affected by aggregation. By extension, since the third-order molecular polarizability γ can be described in terms of the energies and transition dipole moments among the lowest polymethine excited states via the sum-over-states (SOS) expression,[33] such large electronic couplings mean large changes in the thin-film vs. dilute-solution

NLO properties, which we have shown earlier to be detrimental for AOS applications.[2] Since the analysis we presented above suggests that there is little difference between aggregate geometries of streptocyanines with symmetric and asymmetric charge distributions, only the results for symmetric distributions are discussed here; also, since the electronic couplings between LUMOs in these polymethines are comparable to those between HOMOs, we will focus here primarily on the HOMO electronic couplings.

In the streptocyanine/Cl^- system, there are many polymethine pairs within the distance cutoffs used, as pointed out previously. This includes many pairs with essentially no electronic coupling, as well as a significant number of pairs with very large electronic couplings. The distributions of electronic couplings between HOMOs are shown in Figure 7.10 and Figure 7.11 within two normalization schemes: (1) normalization relative to the bulk density of polymethine pairs, as was used in the previous section; and (2) normalization by counting the average number (expectation value) of neighbors in the electronic-coupling range for each polymethine. The distribution of electronic couplings between LUMOs (Figure 7.10 bottom) is very similar to the distribution of HOMO couplings (Figure 7.10 top). Since individual polymethine dyes have very sharp absorption bands (full-width at half-maximum on the order of 100-150 meV),[12,34,35] even a small broadening of the absorption peak due to aggregation will be noticeable. As the band broadening for an ordered stack of molecules is four times the electronic coupling between adjacent molecules,[36] for the sake of the present discussion, we take as a first approximation that electronic couplings smaller than 10 meV will have a negligible effect on the optical properties. On average, it is found that each polymethine has 1.9 neighbors

with electronic couplings > 10 meV. Thus, this substantial number of pairs with large electronic couplings suggests that the thin-film absorption spectra will be substantially broadened relative to the sharp absorption peaks characteristic of polymethines in dilute solution.

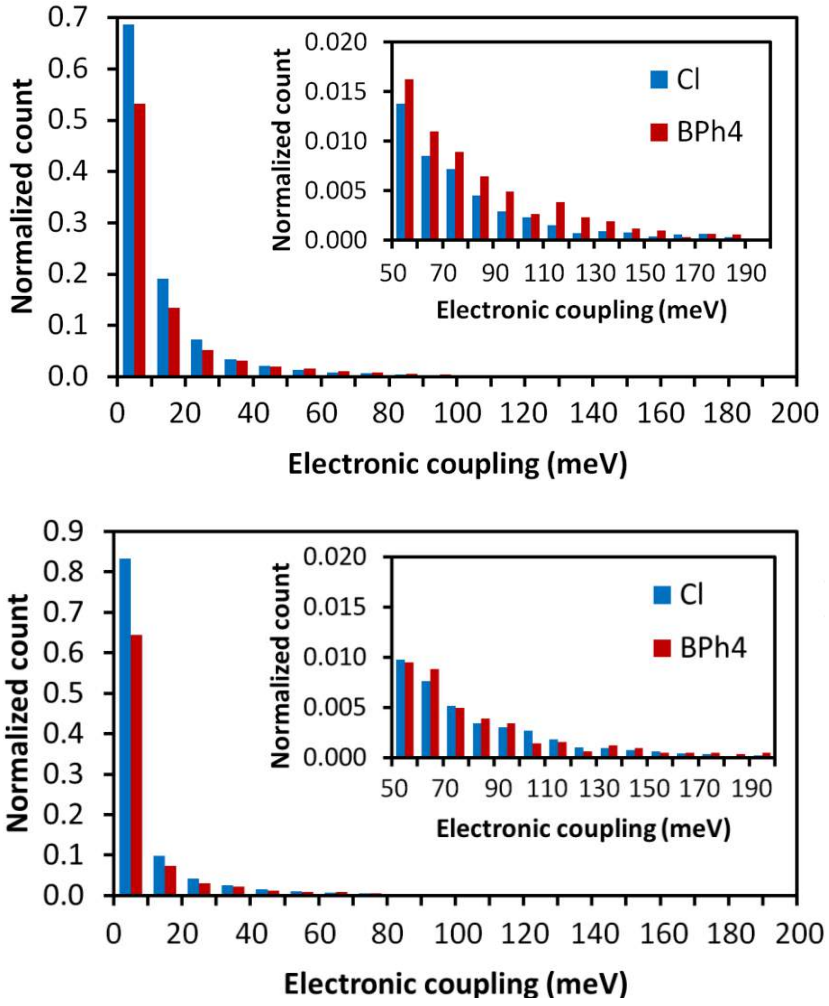

Figure 7.10. Distribution of the absolute electronic coupling between polymethine (top) HOMOs and (bottom) LUMOs. The insets show the absolute electronic coupling distribution with the vertical and horizontal axes expanded. The number of pairs in each range is normalized relative to the bulk density of polymethine pairs as in the previous polymethine-polymethine analysis. A small number of pairs (approx. 1 pair per frame of 500 polymethines) have electronic couplings > 200 meV.

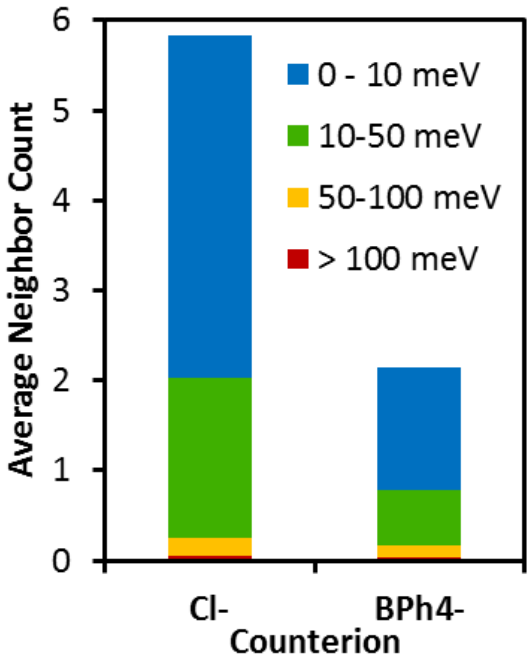

Figure 7.11. Distribution of the absolute electronic couplings between polymethines, normalized in terms of the average number (expectation value) of neighbors each polymethine has within each electronic coupling range.

For polymethine pairs that occur in π-stacked geometries, the electronic couplings fluctuate strongly over the course of the MD simulations. Figure 7.12 displays the evolution of the electronic couplings with time for two representative polymethine pairs. There is little correlation in the electronic couplings between two consecutive time steps at a 2 ps interval. Since the electronic couplings depend on the details of the molecular orbital overlap, and not on the general spatial overlap of the molecules, the absolute values of electronic coupling in pair **I** range from > 250 meV to < 1 meV even though the relative orientations of the molecules stay within a narrow range over the course of the simulation. In pair **II** that has much smaller electronic couplings, the electronic couplings similarly fluctuate but within a much narrower range.

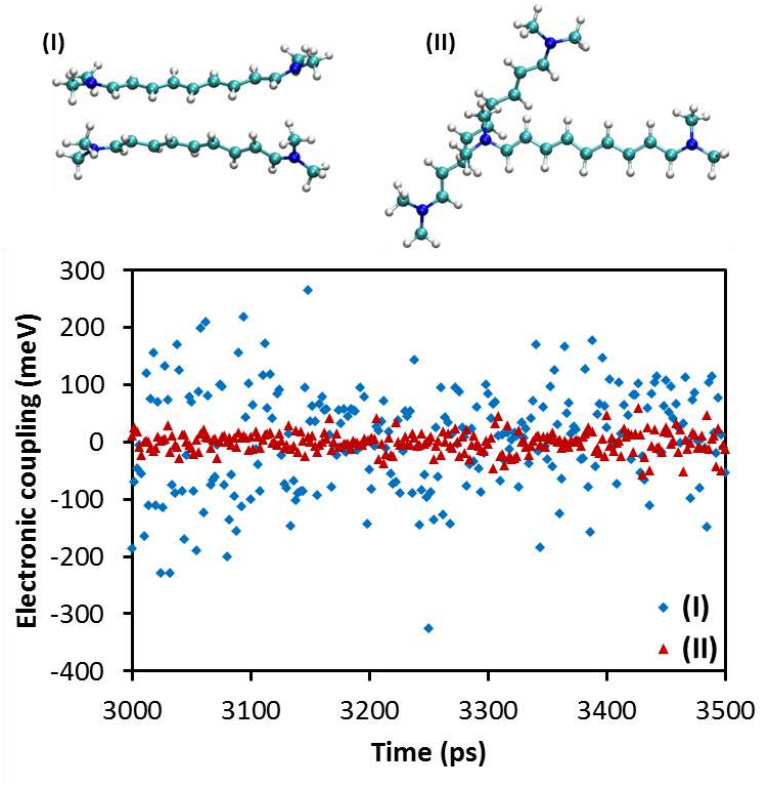

Figure 7.12. (Top) Geometries of polymethine pairs selected from the bulk streptocyanine/Cl^- MD simulations and (bottom) time evolution of the electronic coupling between the polymethines in each pair.

In contrast, in the streptocyanine/BPh_4^- system, the increased bulk of the counterion effectively reduces the polymethine concentration by a factor of 2.1, reducing the number of neighbors within the cutoffs. However, the number of pairs with large electronic couplings is still substantial (average of 0.8 neighbors with > 10 meV electronic couplings). The number of neighbors for each polymethine decreases within all electronic-coupling ranges when switching to BPh_4^- (Figure 7.11); however, when considering the normalization in terms of the bulk density, there is an increase in the number of pairs with electronic couplings > 30 meV (Figure 7.10). These results indicate that while there are fewer polymethine pairs at close distances in the streptocyanine/BPh_4^- system, the pairs that are in close proximity are more likely to be in geometries with large

electronic couplings. Thus, in this case as well, the thin-film absorption spectra are expected to be substantially broadened.

Overall, in the case of simple streptocyanines, the large number of polymethine pairs with significant electronic couplings implies that the optical properties will markedly change in going from dilute solutions to thin films. Such large electronic couplings will typically result in a substantial decrease of the transparency window between the lowest one-photon and two-photon excited states and thus in an increase in Im(γ). Although augmenting the size and softness of the counterion by going from Cl^- to BPh_4^- slightly reduces the number of polymethine pairs with large electronic couplings, such a counterion size increase is not sufficient to sterically prevent polymethine aggregation.

7.3.4. Thiopyrylium Polymethine Amorphous Bulk Structures

To investigate the effect of the substitution pattern on polymethine aggregation, a series of thiopyrylium polymethines **1**-**8** were investigated, see Figure 7.2. These have varying substituents on three parts of the polymethine structure: (i) on the thiopyrylium end groups (**R**); (ii) on the center of the polymethine bridge in the "front" of the molecule (**R'**); and (iii) on the center "back" (**R"**). In each case, one bulky substituent and one less bulky alternative were considered. At this stage, it is useful to stress that our present focus is on the location of the bulky substituents and not on the substituent shape or size. We note that the carbazole (**R'**) and fluorene (**R"**) substituents are rigid and maintain large torsion angles relative to the polymethine backbone, which implies that they have a large projection above and below the polymethine π plane. Because of the steric bulk of

the substituents, the concentration of the neat polymethine/counterion systems varies by a factor of 2.3 across the series. We underline that the series of molecules **1**-**8** has been chosen because their chemical structures are (nearly) identical to molecules that have recently been synthesized and characterized in terms of their linear and nonlinear optical behavior.[14]

As was described for the streptocyanines, the polymethine-counterion and polymethine-polymethine packing configurations and the subsequent impact on polymethine intermolecular electronic couplings were considered for each polymethine. In each of the following sections, we first discuss the limiting cases of the unsubstituted (**1**) and fully substituted (**8**) polymethines to highlight the extent to which bulky substituents can limit polymethine aggregation and then describe the specific impact of each substituent location by considering polymethines **2-7**.

7.3.4.1. Polymethine-counterion interactions

As for the streptocyanines, we first consider the geometries of polymethine-counterion interactions. For each polymethine, the positions of all nearby counterions are considered.

For polymethine **1**, the counterions have a broad range of positions with similar probabilities, as indicated by the ring of higher probability (darker color) around the polymethine in Figure 7.13. The counterion probability is slightly larger near the center of the polymethine with a small positive displacement along the polymethine short axis (the reason being that this structure allows a stronger electrostatic attraction between the

polymethine and counterion because of the inherent charge alternation along the polymethine backbone[26]). The broad distribution of counterion probability found here is similar to that observed for the streptocyanine/BPh_4^- system.[37]

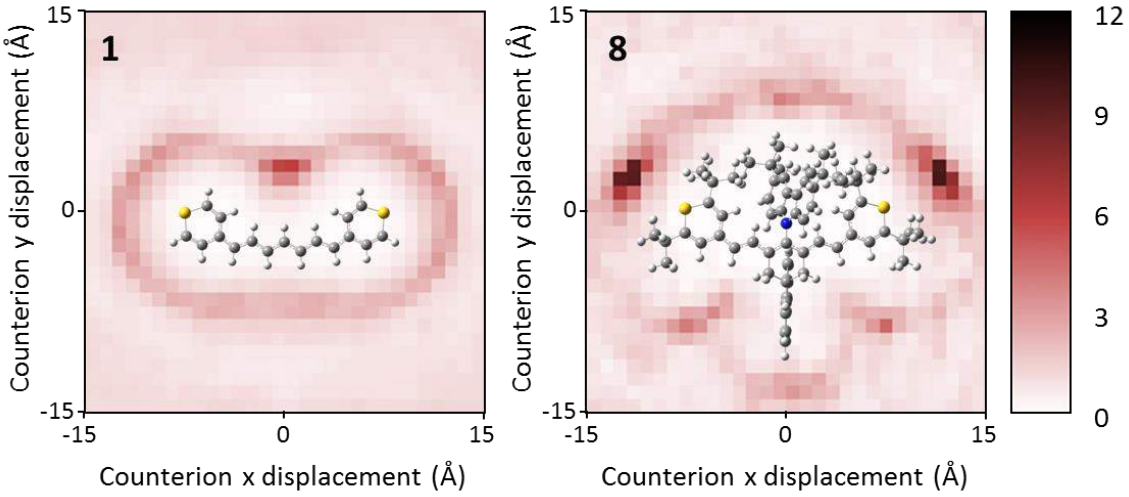

Figure 7.13. Counterion probability distribution in bulk MD simulations of the complexes of polymethines **1** and **8** with BPh_4^-. The color scale corresponds to the probability of finding aggregates, with a probability of one corresponding to the average bulk density of polymethine-counterion pairs.

For the fully substituted polymethine **8**, the bulky substituents cause the counterion to sit much farther from the polymethine backbone than for **1**, as shown by the comparison of the two plots in Figure 7.13. Indeed, most of the polymethine backbone is shielded from the counterion by the substituents. In particular, the counterion cannot approach the back of the polymethine backbone due to the blocking induced by the fluorene and *t*-butyl substituents; although there would appear in the figure to be some counterion probability in this area, it is due to counterions that are several angstroms above or below of the plane of the polymethine.

The most probable counterion position is near the sulfur atoms in the thiopyrylium rings; this is in fact the only area where the counterions are is sterically able to be close to the positively charged polymethine core. Analysis of the radial distribution functions (RDFs, see Figure 7.14) for the sulfur-boron distances shows an increase in the onset from 4.4 Å in **1** to 4.8 Å in **8**. It is useful to note that, although the probability of finding a counterion near the sulfur atom is much larger relative to the bulk counterion concentration for **8** than for **1** as seen in Figure 5, this difference is primarily due to the factor of 2.3 difference in polymethine concentrations (see Figure 7.2); when taking the concentration difference into account, the peak probability is larger by only a factor of 1.2 for polymethine **8** than for **1** in absolute terms.

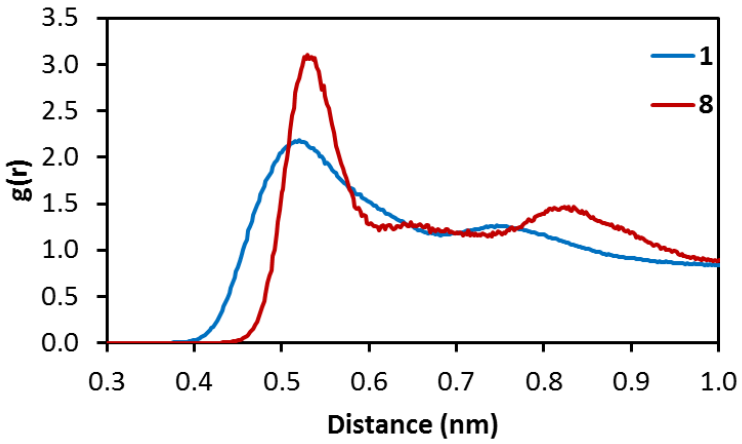

Figure 7.14. Sulfur-boron radial distribution function for polymethines **1** and **8**.

When bulky substituents are added only to the center of the polymethine backbone (**2-4**), the counterion has expectedly a high probability of being near the thiopyrylium rings where there is no steric hindrance to ion pairing (Figure 7.15). In contrast, in the polymethines with bulky end substituents (**5-7**), the counterion can only approach the terminal thiopyrylium rings in positions near the sulfur atoms as in the case of **8**. Taking

into account the variations in polymethine concentrations, the peak probabilities of finding the counterions near the sulfur atoms are larger by only a factor of 1.2-1.4 for polymethines **5-7** with respect to **1**.

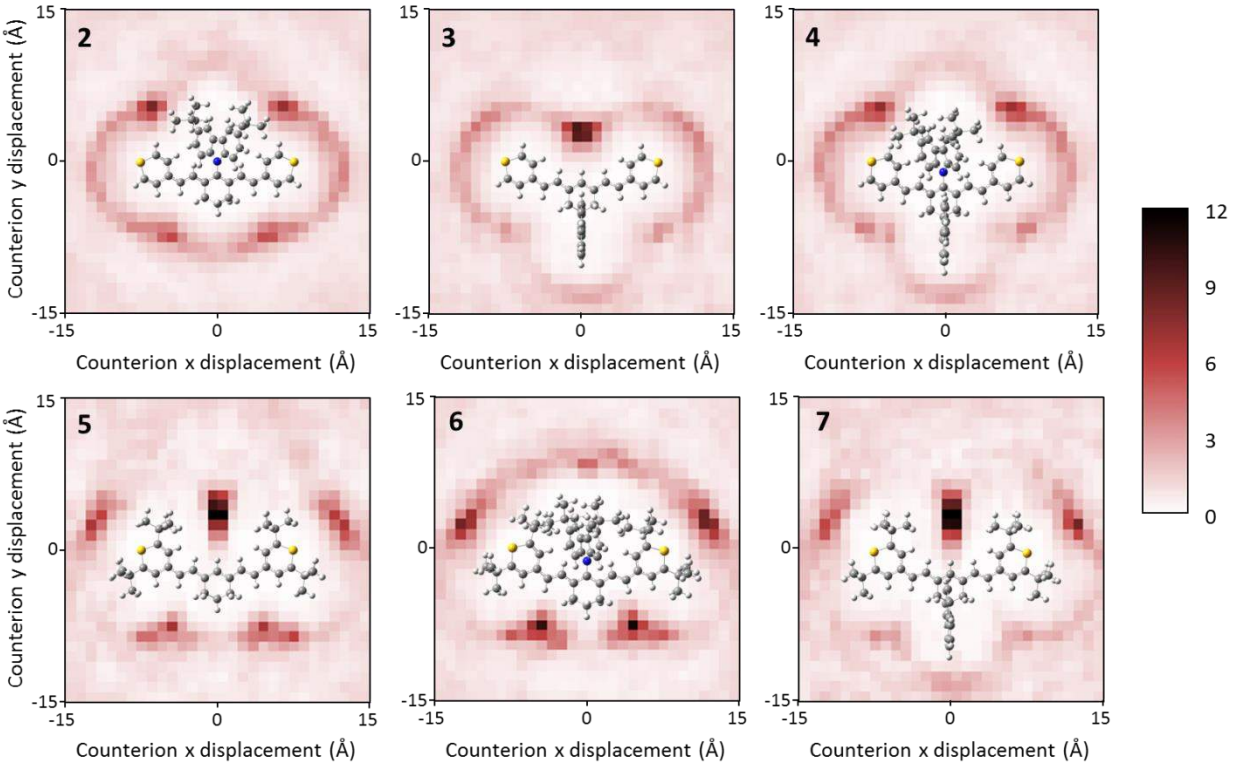

Figure 7.15. Counterion probability distribution in bulk MD simulations of the complexes of polymethines **2-7** with BPh_4^-. The color scale corresponds to the probability of finding aggregates, with a probability of one corresponding to the average bulk density of polymethine-counterion pairs.

The substitution pattern also influences the counterion probability distribution near the polymethine backbone. In some of the polymethines, a cyclohexyl ring is added on the back of the bridge (**R"**) to increase thermal and photo-stability.[35] This ring also aids in partially shielding the counterion from interacting with the back of the polymethine. In polymethines **7**-**8**, the *t*-butyl and fluorene substituents completely prevent the counterion from approaching the back of the polymethine.

In polymethines **5** and **7** with no substituents on the center front, the counterion is able to fit between the end *t*-butyl substituents and approach the front of the polymethine backbone, as evidenced by the dark areas just above the centers of the plots in Figure 7.15. When normalizing to consider concentration differences, the absolute probability of finding a counterion in the areas with the largest counterion probabilities is about 1.5 times larger for **5** and **7** than it is for **1**.

Since polymethine symmetry-breaking is related to the combined electrostatic interactions derived from all counterions and polymethines, it is challenging to directly evaluate the extent of symmetry breaking in these systems. However, since symmetry breaking is essentially induced by the electric field felt along the polymethine long axis, counterions positioned near one end of the polymethine can have a much more significant contribution to symmetry breaking than counterions either near the center of the polymethine or far from the polymethine core. In polymethines **1-4** without bulky substituents near the end groups, the large probability of counterions near the end groups underline the potential for significant symmetry breaking. Although the bulky substituents near the end groups in **5-8** slightly increase the counterion probability in a small area near the sulfur atoms, they greatly reduce the counterion probability in all other geometries near the thiopyrylium end groups. This suggests that these bulky substituents may be sufficient to reduce (but not necessarily entirely eliminate) symmetry breaking of the polymethines. Further efforts to understand the role of the counterion positions on polymethine symmetry breaking are currently in progress.

7.3.4.2. Polymethine-polymethine interactions

As for the streptocyanines, we now turn to the interaction geometries in polymethine pairs. Polymethine **1** forms many aggregates, each dye having an average of 2.6 neighbors within the distance cutoffs used (6 Å radial distance; 12 Å longitudinal offset). The most probable pair geometries for **1** are H-aggregates with relatively small offsets of 1-4 Å, as shown by the darker region near the bottom left corner in Figure 7.16.[38] While H-aggregates are more common than J-aggregates or perpendicular aggregates by roughly a factor of four, it should be emphasized that a broad distribution of aggregate geometries is observed.

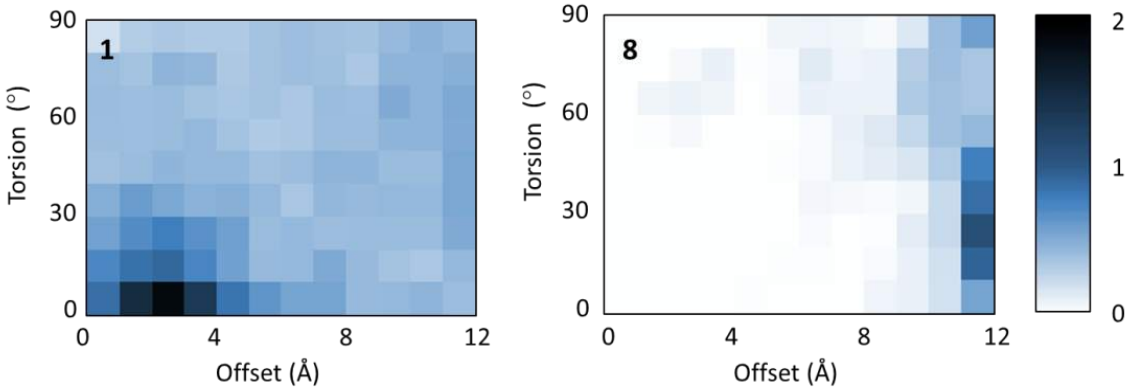

Figure 7.16. Probability distribution of aggregate geometries for the complexes of polymethines **1** and **8** with BPh_4^-. The color scale corresponds to the probability of finding aggregates; a probability of one corresponds to the average bulk density of polymethine pairs.

Very importantly and in strong contrast to **1**, polymethine **8** has almost no geometries in which the polymethines can aggregate such that the π-backbones are near each other, as indicated by the nearly white areas throughout most of the probability distribution plot on the right of Figure 7.16. The probability of finding any pairs within a radial distance of 6

Å only becomes significant at offset distances greater than 11 Å. Within the cutoffs, each polymethine has an average of only 0.32 neighbors. The differences between the aggregate probabilities in these systems highlight that the bulky substituents eliminate nearly all polymethine aggregation by sterically hindering interactions between the polymethine cores.

The specific locations of the substituents greatly impact the polymethine aggregate structures. The addition of bulky substituents to the center of the polymethine (**2-4**; see Figure 7.17) hinders H-aggregation, though stacking of the terminal thiopyrylium rings is still possible. Since the thiopyrylium rings can stack within a wide distribution of torsion angles, these structures range from J-aggregates with offsets > 9 Å to perpendicular aggregates with offsets on the order of 4-5 Å. A detailed analysis shows that some of the pairs at large torsion angles instead have interactions between one thiopyrylium ring of the first polymethine and the π-system of the carbazole or fluorene substituent of the second polymethine. The presence of substituents both in the center front and the center back of the polymethine backbone hinders H-aggregation to a greater extent than having only one such substituent present.

Interestingly, substituents on the terminal groups tend to reduce polymethine aggregation in all geometries. This is the case even in polymethine **5** where no bulky substituents are added to the center of the polymethine. However, while aggregation is substantially reduced, there are still more polymethine pairs in close proximity than in **8**. Analysis of these pairs shows that **5** forms aggregates in both parallel and perpendicular geometries.

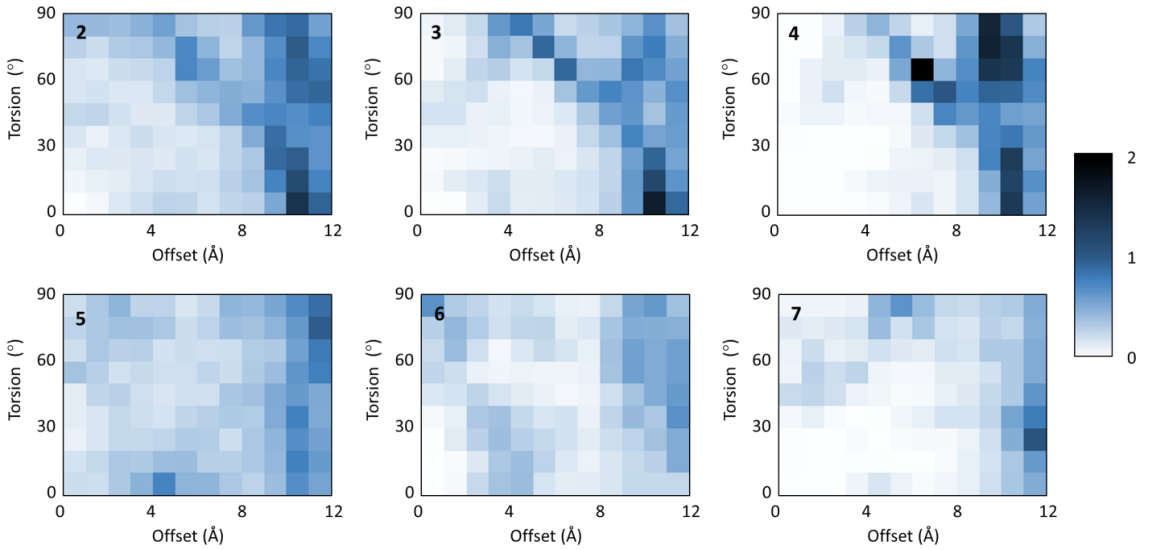

Figure 7.17. Probability distribution of aggregate geometries for the complexes of polymethines **2-7** with BPh_4^-. The color scale corresponds to the probability of finding aggregates; a probability of one corresponds to the average bulk density of polymethine pairs.

In contrast, in **6** and **7**, the polymethine pairs within the distance cutoffs typically have a significant tilt or short-axis offset between the π-systems, which reduces the stacking efficacy. This distinction between π-stacked and non-π-stacked aggregate geometries points to the need for further analysis to fully understand the effect of substituents on the material optical properties.

7.3.4.3. Electronic couplings between polymethine molecules

We have shown earlier[21,26] that electronic couplings between adjacent polymethines larger than ~10 meV alters the characteristics of the lowest-lying excited states and adversely affects the nonlinear optical properties relevant for AOS applications. Thus, it is important to evaluate the impact of substitution on the electronic couplings between the HOMO and LUMO levels of neighboring molecules (as these are the electronic levels essentially involved in the lowest excited states. Here, we focus on the HOMO electronic

couplings as the streptocyanine results described previously show that the LUMO electronic couplings are comparable to the HOMO electronic couplings. We recall that electronic couplings are a direct function of wavefunction overlap (and not of spatial overlap)[39] and thus strongly depend on aggregate geometries.

As indicated in the previous section, polymethine **1** forms a substantial number of polymethine pairs in close proximity. The electronic-coupling calculations were performed for all of these polymethine pairs extracted at several time steps from the MD simulations; there occurs a mixture of stacked pairs and pairs in orientations with no significant electronic interaction between the dye molecules. Here, there are many polymethine pairs with substantial electronic couplings; on average, each polymethine has 1.4 neighbors with electronic couplings greater than 10 meV. The distribution of electronic couplings extends to very large values, significantly beyond the 100 meV limit chosen in Figure 7.18.

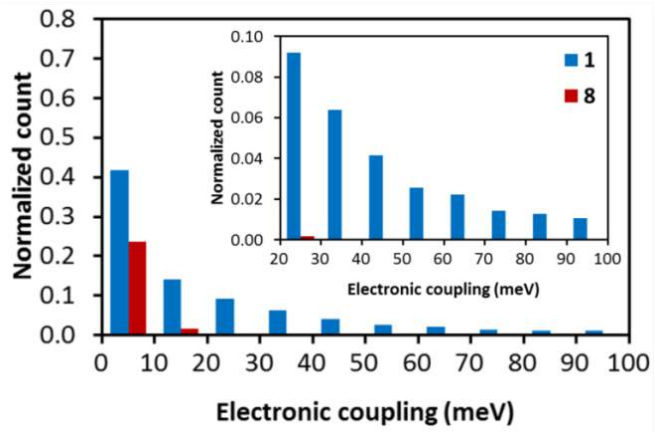

Figure 7.18. Distribution of the absolute electronic couplings between adjacent dye molecules for polymethines 1 and 8. The number of pairs in each range is normalized relative to the bulk density of polymethine pairs as in the previous polymethine-polymethine analysis. For polymethine 1, some polymethine pairs (approximately 23 pairs per frame of 500 polymethines) have an electronic coupling > 100 meV.

The large number of polymethine pairs with strong electronic couplings points to large modifications of the linear and nonlinear optical properties upon aggregation, which is typical of traditional polymethines.[2,4,40-42] H-aggregates tend to have the largest electronic couplings, with the electronic coupling generally decreasing as a function of increasing offset and torsion angle (the distributions of electronic couplings as a function of aggregate geometry is shown in Figure 7.19). Because of the nodal pattern in the orbitals, in pairs with nearly parallel long axes, the electronic coupling strongly fluctuates as the offset increases.

In polymethine **8**, there are substantially fewer polymethine pairs in close proximity, out of which only a small number have any significant electronic coupling: less than 3% of the polymethines have a neighbor with an electronic coupling > 10 meV. This marked reduction in the number of closely-packed polymethine pairs combined with the generally weak electronic couplings underline that polymethine **8** should largely retain dilute solution-like absorption spectra and NLO properties in the bulk, which is fully consistent with very recent experimental observations.[14]

In polymethines with bulky substituents exclusively in the molecular center, the number of polymethine pairs with electronic couplings greater than 100 meV is strongly reduced relative to **1**, although there are still many pairs with electronic couplings > 10 meV (Figure 7.20). This is consistent with the elimination of H-aggregates; we note that the electronic coupling in a well-aligned J-aggregate is substantially smaller than that in a well-aligned H-aggregate, due to decreased wavefunction overlap of the π-orbitals.[39] The

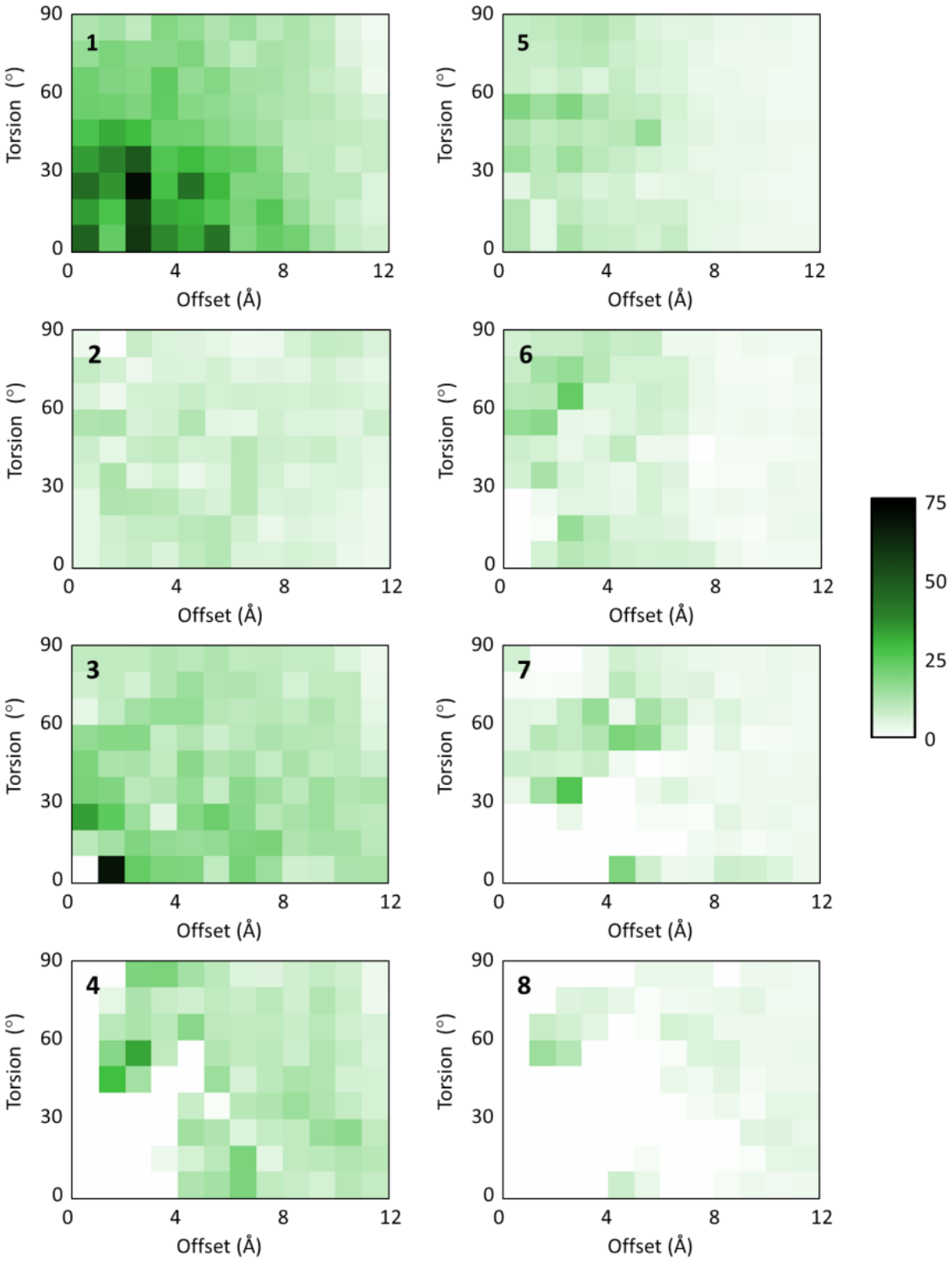

Figure 7.19. Average electronic coupling values for the complexes of polymethines 1-8 with BPh_4^-. The color scale corresponds to the average electronic coupling for polymethine pairs in each range of geometric structures.

large number of polymethine pairs with significant electronic couplings in J-aggregate geometries is consistent with a marked broadening/shift of the thin-film absorption spectra with respect to dilute solutions, as has been observed experimentally.[14]

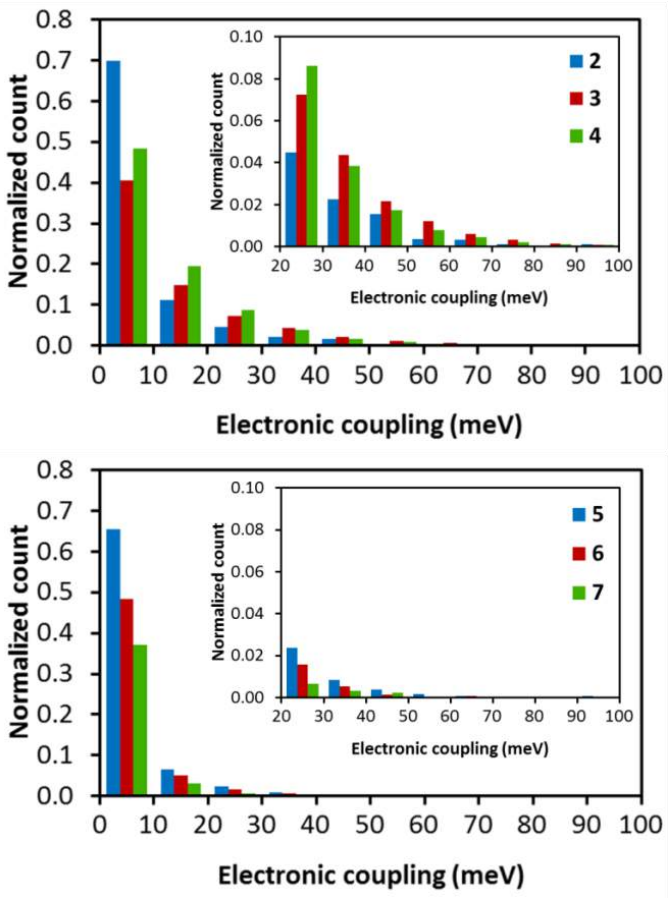

Figure 7.20. Distribution of the absolute electronic coupling between dye molecules for polymethines 2-7. The number of pairs in each range is normalized relative to the bulk density of polymethine pairs as in the previous polymethine-polymethine analysis.

Although the presence of substituents in the center of the polymethine backbone changes the bulk morphologies relative to **1**, the effect is primarily one of changing what type of aggregation occurs. The polymethines and counterions still ion-pair in geometries where the counterions are near the polymethine end groups, and J-aggregation is enhanced. While greater steric hindrance is needed to substantially reduce aggregation, a strategy of

adding steric bulk only to the center of the polymethine structure should prove a viable strategy to selectively form J-aggregates in applications where controlled aggregation is desired.

In contrast, bulky substituents on the end groups result in largely reduced electronic couplings between polymethines, as was seen for polymethine **8**. Among these polymethines, **5** has somewhat more pairs with significant electronic couplings. This is consistent with the limited steric bulk and the number of pairs that appear to have significant stacking of the conjugated backbones, though the maximum electronic couplings remain low because the pairs in π-stacked geometries have relatively large intermolecular distances and/or large torsion angles. While polymethines **6** and **7** have substantially more pairs in close proximity than does **8**, the number of pairs with significant electronic coupling is still small. These small electronic couplings are consistent with the moderate thin-film AOS figures-of-merit measured for polymethines with similar substitution patterns.[14]

Overall, our results indicate that while bulky substituents tend to reduce polymethine aggregation through steric hindrance, it is the location of the bulky substituents that plays a critical role in determining the extent of aggregation and the types of aggregates that form. In particular, the degree of electronic coupling is not directly correlated with the number of pairs in close proximity. This is especially apparent when comparing polymethines 4 and 5. These two polymethines have essentially the same number of neighbors per polymethine within the distance cutoffs (Figure 7.21); however,

polymethine **4** has nearly three times as many pairs with significant electronic couplings as does polymethine **5**. The large decrease in the number of polymethine pairs with significant electronic couplings in polymethines **5-7** suggests that increasing the steric bulk on *all* parts of the molecular structure (ends, center back, and center front) is not a necessary condition to maintain solution-like linear and nonlinear optical properties in thin films, which is consistent with experimental observations.[14]

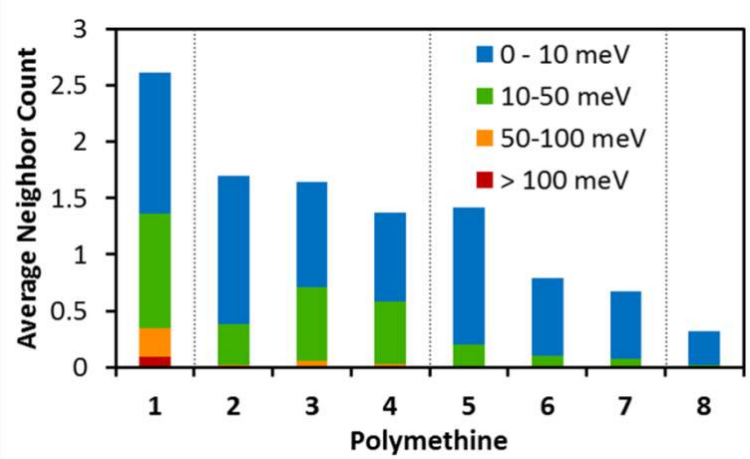

Figure 7.21. Distribution of the absolute electronic couplings between polymethines, normalized in terms of the average number (expectation value) of neighboring polymethines each polymethine will have within each electronic coupling range.

7.4. Conclusions

Understanding polymethine aggregation is an essential step in developing polymethine-based materials with a large figure-of-merit for all-optical switching. Both polymethine-counterion interactions and polymethine-polymethine interactions must be minimized to prevent symmetry-breaking of the polymethines and the appearance of low-lying two-photon excited states. Taking the examples of simple streptocyanines and thiopyrylium polymethines with bulky substituents, we have investigated the way polymethines

aggregate in the bulk to provide an understanding of their thin-film optical properties. To do so, we have developed a combined molecular-dynamics / electronic-structure methodology.

From our simulations of amorphous bulk structures for streptocyanines with either Cl^- or BPh_4^- counterions, we have found that the distribution of counterion positions relative to the polymethines is much broader in the case of the bulkier BPh_4^- counterion than in the case of the Cl^- counterion. This difference can be understood on the basis of the electrostatic / charge distribution differences between the two counterions. With either counterion, the polymethines form a broad range of aggregates with significant electronic couplings. As a result, the linear absorption spectra are expected to be substantially broadened in the bulk and the nonlinear optical properties of interest for all-optical switching applications, to be adversely affected with respect to those of isolated polymethines. Increasing the counterion size from Cl^- to BPh_4^- is not sufficient to prevent polymethine aggregation. Thus, to prevent aggregation of the polymethine dyes in the bulk and their negative impact on the NLO properties of interest for AOS applications, other strategies than a simple increase in the size and softness of the counterions need to be followed.

Our simulations of the bulk structures of substituted thiopyrylium polymethines show that a proper choice of bulky substituents can result in efficient steric hindrance for both polymethine-counterion and polymethine-polymethine interactions. However, it must be borne in mind that the presence of bulky substituents decreases the concentration of

NLO-active chromophores in the thin films, thereby reducing the maximum achievable $|Re(\chi^{(3)})|$. The number and locations of the substituents are seen to affect polymethine aggregation dramatically. The unsubstituted thiopyrylium polymethine forms aggregates in many geometries with substantial electronic couplings, particularly H-aggregates. Substituents in the center of the molecule tend to hinder H-aggregation and enhance J-aggregation, while substituents on the ends of the polymethine somewhat reduce but do not entirely prevent aggregation. When bulky substituents are present on both the molecular ends and center, aggregation is then almost entirely suppressed due to steric hindrance. Our analysis of the electronic-coupling results points out that it is possible to strategically select bulky substituents that increase the AOS figure-of-merit with minimal excess bulk in order to maximize the chromophore concentration in thin films.

To conclude, our methodology allows a deeper understanding of how chemical structure affects polymethine aggregation on the molecular scale as compared to what can be easily obtained through experimental studies. Thus, our theoretical approach provides a means of evaluating the effects of molecular structure on aggregation prior to synthesis, which will aid in providing further design guidelines for polymethine-based AOS materials.

7.5. References

(1) Hales, J. M.; Matichak, J.; Barlow, S.; Ohira, S.; Yesudas, K.; Bredas, J. L.; Perry, J. W.; Marder, S. R. *Science* **2010**, *327*, 1485.

(2) Mukhopadhyay, S.; Risko, C.; Marder, S. R.; Brédas, J.-L. *Chem. Sci.* **2012**, *3*, 3103.

(3) Das, S.; Bwambok, D.; El-Zahab, B.; Monk, J.; de Rooy, S. L.; Challa, S.; Li, M.; Hung, F. R.; Baker, G. A.; Warner, I. M. *Langmuir* **2010**, *26*, 12867.

(4) Baraldi, I.; Caselli, M.; Momicchioli, F.; Ponterini, G.; Vanossi, D. *Chem. Phys.* **2002**, *275*, 149.

(5) Haverkort, F.; Stradomska, A.; de Vries, A. H.; Knoester, J. *J. Phys. Chem. A* **2014**, *118*, 1012.

(6) Haverkort, F.; Stradomska, A.; de Vries, A. H.; Knoester, J. *J. Phys. Chem. B* **2013**, *117*, 5857.

(7) Spano, F.; Mukamel, S. *Phys. Rev. A* **1989**, *40*, 5783.

(8) D'Avino, G.; Terenziani, F.; Painelli, A. *J. Phys. Chem. B* **2006**, *110*, 25590.

(9) Meyers, F.; Marder, S. R.; Pierce, B. M.; Bredas, J. L. *J. Am. Chem. Soc.* **1994**, *116*, 10703.

(10) Wernke, W.; Pfeiffer, M.; Johr, T.; Lau, A.; Grahn, W.; Johannes, H.-H.; Dahne, L. *Chem. Phys.* **1997**, *216*, 337.

(11) Pierce, B. M. *Proc. SPIE* **1991**, *1560*, 148.

(12) Johr, T.; Wernke, W.; Pfeiffer, M.; Lau, A.; Dahne, L. *Chem. Phys. Lett.* **1995**, *246*, 521.

(13) Gieseking, R. L.; Mukhopadhyay, S.; Risko, C.; Brédas, J.-L. *ACS Photon.* **2014**, *1*, 261.

(14) Barlow, S.; Brédas, J. L.; Getmanenko, Y. A.; Gieseking, R. L.; Hales, J. M.; Kieu, K.; Kim, H.; Marder, S. R.; Norwood, R. A.; Perry, J. W.; Peyghambarian, N.; Risko, C.; Shahin, S.; Zhang, Y. *Mater. Horiz.* **2014**, DOI: 10.1039/c4mh00068d.

(15) Jorgensen, W. L.; Maxwell, D. S.; Tirado-Rives, J. *J. Am. Chem. Soc.* **1996**, *118*, 11225.

(16) Hess, B.; Kutzner, C.; van der Spoel, D.; Lindahl, E. *J. Chem. Theory Comput.* **2008**, *4*, 435.

(17) Chai, J.-D.; Head-Gordon, M. *Phys. Chem. Chem. Phys.* **2008**, *10*, 6615.

(18) Chai, J.-D.; Head-Gordon, M. *J. Chem. Phys.* **2008**, *128*, 084106.

(19) Dunning, T. H. *J. Chem. Phys.* **1989**, *90*, 1007.

(20) Gaussian 09, Revision B.01, M. J. Frisch, G. W. Trucks, H. B. Schlegel, G. E. Scuseria, M. A. Robb, J. R. Cheeseman, G. Scalmani, V. Barone, B. Mennucci, G. A. Petersson, H. Nakatsuji, M. Caricato, X. Li, H. P. Hratchian, A. F. Izmaylov, J. Bloino, G. Zheng, J. L. Sonnenberg, M. Hada, M. Ehara, K. Toyota, R. Fukuda, J. Hasegawa, M. Ishida, T. Nakajima, Y. Honda, O. Kitao, H. Nakai, T. Vreven, J. A. Montgomery, Jr., J. E. Peralta, F. Ogliaro, M. Bearpark, J. J. Heyd, E. Brothers, K. N. Kudin, V. N. Staroverov, T. Keith, R. Kobayashi, J. Normand, K. Raghavachari, A. Rendell, J. C. Burant, S. S. Iyengar, J. Tomasi, M. Cossi, N. Rega, J. M. Millam, M. Klene, J. E. Knox, J. B. Cross, V. Bakken, C. Adamo, J. Jaramillo, R. Gomperts, R. E. Stratmann, O. Yazyev, A. J. Austin, R. Cammi, C. Pomelli, J. W. Ochterski, R. L. Martin, K. Morokuma, V. G. Zakrzewski, G. A. Voth, P. Salvador, J. J. Dannenberg, S. Dapprich, A. D. Daniels, O. Farkas, J. B. Foresman, J. V. Ortiz, J. Cioslowski, and D. J. Fox, Gaussian, Inc., Wallingford CT, 2010.

(21) Huang, Z.; Ji, D.; Xia, A.; Koberling, F.; Patting, M.; Erdmann, R. *J. Am. Chem. Soc.* **2005**, *127*, 8064.

(22) Baraldi, I.; Momicchioli, F.; Ponterini, G.; Tatikolov, A. S.; Vanossi, D. *Phys. Chem. Chem. Phys.* **2003**, *5*, 979.

(23) Dahne, L.; Reck, G. *Angew. Chem. Int. Ed.* **1995**, *34*, 690.

(24) This analysis neglects a degree of freedom for the long-axis orientations: in general, polymethine B need not be perpendicular to R. Within the range of radial distances and offsets considered here, the variation in this angle is small enough that it can be neglected due to sterics.

(25) Ridley, J.; Zerner, M. *Theor. Chim. Acta* **1973**, *32*, 111.

(26) Mataga, N.; Nichimoto, K. *Z. Phys. Chem.* **1957**, *13*, 140.

(27) Gorman, C. B.; Marder, S. R. *Proc. Natl. Acad. Sci. USA* **1993**, *90*, 11297.

(28) The polymethine structure can be considered as a linear combination of two resonance forms: one with the charge localized on one terminal nitrogen and a pattern of alternating single and double bonds along the molecular backbone, and a second with the charge localized on the opposite terminal nitrogen and a reversal of the single-double

bond pattern. The BLA of each resonance structure is approximately +/- 0.1 A, and a BLA near 0 implies a near-equal mixing of the two resonance forms.

(29) The polymethine with an asymmetric charge distribution is oriented such that the end with a larger positive charge is at a negative Dx value.

(30) Dahne, S.; Kulpe, S. *Abh. Akad. Wiss. DDR, Abt. Math. Naturwiss., Tech.* **1977**, *8*, 1.

(31) Salem, L. *The molecular orbital theory of conjugated systems*; 4th print. with corrections ed.; W. A. Benjamin: Reading, Mass., 1974, c1966.

(32) Gieseking, R. L.; Mukhopadhyay, S.; Risko, C.; Marder, S. R.; Brédas, J.-L. *Adv. Mater.* **2014**, *26*, 68.

(33) Orr, B. J.; Ward, J. F. *Mol. Phys.* **1971**, *20*, 513.

(34) Tolbert, L. M.; Zhao, X. *J. Am. Chem. Soc.* **1997**, *119*, 3253.

(35) Hales, J. M.; Barlow, S.; Kim, H.; Mukhopadhyay, S.; Brédas, J.-L.; Perry, J. W.; Marder, S. R. *Chem. Mater.* **2014**, *26*, 549.

(36) Haddon, R. C.; Siegrist, T.; Fleming, R. M.; Bridenbaugh, P. M.; Laudise, R. A. *J. Mater. Chem.* **1995**, *5*, 1719.

(37) Gieseking, R. L.; Mukhopadhyay, S.; Shiring, S. B.; Risko, C.; Brédas, J.-L. *Unpublished work.*

(38) We note that in similar systems, aggregation is strongly dependent on the counterion size; see ref. 10.

(39) Brédas, J. L.; Calbert, J. P.; da Silva Filho, D. A.; Cornil, J. *Proc. Natl. Acad. Sci. USA* **2002**, *99*, 5804.

(40) von Berlepsch, H.; Böttcher, C.; Dähne, L. *J. Phys. Chem. B* **2000**, *104*, 8792.

(41) Scarpaci, A.; Nantalaksakul, A.; Hales, J. M.; Matichak, J. D.; Barlow, S.; Rumi, M.; Perry, J. W.; Marder, S. R. *Chem. Mater.* **2012**, *24*, 1606.

(42) Belfield, K. D.; Bondar, M. V.; Hernandez, F. E.; Przhonska, O. V.; Yao, S. *Chem. Phys.* **2006**, *320*, 118.

CHAPTER 8

CONCLUSIONS AND OUTLOOK

8.1. Conclusions

The ever-increasing demand for high-speed data transmission in fiber-optic cables has produced a need for devices that can process light signals via various nonlinear optical (NLO) processes. In particular, all-optical switching (AOS) devices are required to achieve faster switching speeds and remove the need for conversion of the optical signal to an electrical signal. Organic π-conjugated materials, especially those based on polymethines, have shown promise for AOS applications, but key hurdles remain in translating the dilute-solution properties to materials suitable for devices. To address these challenges, we have used a combination of quantum-chemical and molecular-dynamics approaches to investigate the molecular and material properties of polymethines and related molecules. We have focused in particular on three areas: (i) understanding the relationships among the polymethine molecular electronic structure, excited-state properties, and NLO properties; (ii) evaluating the NLO properties of more complex π-conjugated molecules that cannot be described in terms of the commonly used essential-state model; and (iii) describing the dependence of the bulk NLO properties on the polymethine and counterion chemical structures in terms of the aggregate geometric structures and electronic couplings.

As the polymethine NLO properties can be computed in terms of the first several excited-state energies, state dipole moments, and transition dipole moments, a chemical

understanding of the NLO properties can be achieved in terms of the relationships between the molecular structure and the optical properties. In particular, a small transition dipole moment $\mu_{ee'}$ between the first and second polymethine excited states can aid in achieving a large figure-of-merit for AOS by maximizing |Re(γ)| and minimizing Im(γ). We have shown that in streptocyanines and polyenes, $\mu_{ee'}$ is small owing to cancellation of opposite-sign contributions from the two single-electron excitations and one double-electron excitation that compose the second excited state. By examining the effect of substituents in the center of the streptocyanine structure on $\mu_{ee'}$, we have demonstrated the importance of maintaining large energetic spacings between the first several polymethine frontier molecular orbitals to preserve a small $\mu_{ee'}$. This decomposition scheme and understanding of the critical role of the molecular-orbital spacing can be applied as a broader range of chemical modifications are made to the polymethine structure.

Although isolated C_{2v}-symmetric polymethines inherently have favorable NLO properties for AOS applications, polymethines often do not retain these properties in complex environments. By examining several series of calculations for streptocyanines in electric fields, we have shown that it is critical to distinguish between BOA and BLA to accurately evaluate the effect of the environment on the polymethine molecular properties: whereas BOA directly assesses the electronic structure, BLA is solely a measure of the geometric structure. BOA is consistently correlated with the molecular optical and NLO properties, whereas BLA is strongly correlated with the NLO properties *only* when the geometries under consideration are energetic minima in the environment of

interest. This highlights the importance of carefully designing computational studies of the polymethine optical and NLO properties, particularly in complex environments or when non-equilibrium geometries are being considered.

Although polymethine symmetry-breaking can in some cases be caused directly by interactions with the environment, experimental evidence suggests that some long polymethines have inherently symmetry-broken structures. The crossover point from symmetric to symmetry-broken structures is challenging to model computationally. We have first shown that CC2 and long-range corrected DFT approaches produce streptocyanine molecular geometries and charge distributions comparable to those at high levels of theory; the long-range corrected DFT results also show good agreement with the experimental crossover point for polymethines with larger conjugated end groups. We demonstrated that solvation increases charge localization on the polymethine end groups and decreases the length at which the crossover point occurs. Analysis of the vibrational modes suggests that a vibrational mode associated with a large change in BLA and a very large IR intensity decreases in frequency when approaching the crossover point. We show that the vibrational modes that involve large changes in BLA significantly couple the first several polymethine states; further work is needed to develop a diabatic model that could describe the key states and couplings that contribute to symmetry-breaking.

Even though many of the structure-property relationships describing the NLO properties of polymethines and other linear π-conjugated systems have long been known, there has been little extension of this understanding to molecules with multidimensional π-

conjugated systems. The NLO properties of these molecules are particularly of interest because large π-conjugated counterions are currently being used to minimize polymethine symmetry-breaking. We show that molecules of the form XPh_4 ($X = B^-$, C, N^+, P^+) have a negative Re(γ), a characteristic shared by very few classes of molecules besides polymethines. However, unlike in polymethines, an essential-state model is insufficient to describe the optical and NLO properties in these systems. The negative Re(γ) values in the XPh_4 series are due to a band of excited states, several of which have significant transition dipole moments to the ground state but few large transition dipole moments to other excited states. Although |Re(γ)| is rather small in the XPh_4 series, the discovery of a new molecular structure in which Re(γ) is negative may provide new approaches for the molecular design of third-order NLO materials.

Because polymethine symmetry-breaking and interchromophore interactions dramatically change the optical and NLO properties, translating the isolated polymethine NLO properties to materials suitable for AOS applications requires preventing nearly all aggregation at very large polymethine concentrations. We have underlined that in prototypical polymethines with no bulky substituents, many close polymethine-counterion and polymethine-polymethine interactions occur in a broad distribution of geometries. The large electronic couplings within many polymethine pairs suggest that the aggregation causes significant changes in the optical and NLO properties. In contrast, strategic substitution of the polymethines with bulky substituents can substantially reduce aggregation. The electronic couplings can also be greatly reduced, suggesting that substituted polymethines can maintain solution-like optical and NLO properties in thin

films. The aggregation depends not only on the extent of substitution but also on the locations of the substituents: substituents on the center of the polymethine bridge tend to hinder H-aggregation but promote J-aggregation, whereas substituents on the ends generally reduce all forms of aggregation. Understanding the relationships between chemical structure and the aggregate geometries and electronic structures provides guidance for polymethine design in future experimental studies.

8.2. Future Directions

While our computational studies have led to improved understanding of structure-property relationships in π-conjugated systems for NLO applications, there remain a number of unanswered questions that could further aid in the development of NLO molecules and materials. First, the large contribution of double excitations to the polymethine second excited states makes it particularly challenging to compute the excited-state properties with sufficient accuracy to evaluate structure-property relationships. For streptocyanines, the CC2 methodology has recently shown promise in accurately predicting the ratio of the first and second excited-state energies. Further work is needed to evaluate whether CC2 likewise predicts accurate excited-state energies for more complex polymethines. However, preliminary results suggest that CC2 may predict overly large values of $\mu_{ee'}$ due to the perturbative treatment of double excitations. This is consistent with the key role of double excitations in determining the magnitude of $\mu_{ee'}$. Exploration of other computational methods that treat double excitations more completely may be able to provide a more accurate evaluation of both excited-state energies and transition dipole moments. Appropriate high-level methods would enable

the investigation of questions that current methods are insufficient to address, such as the relationship between polymethine structure and the energetic window between the first two electronic excited states.

In addition, vibronic effects on the polymethine optical properties are important to understand. Experimental evidence suggests that the first two-photon absorption (TPA) peak is close to the one-photon absorption (OPA) energy; this feature has been assumed to be due to vibronic TPA into the first electronic excited state but has not been confirmed computationally. Understanding which vibrational modes contribute to the vibronic TPA and how the molecular structure and environment affect the position and strength of the vibronic TPA may aid in developing polymethines with an improved energy window between the first and second TPA peaks. In addition, computing the vibronic broadening of the OPA spectrum may provide insight into polymethine symmetry-breaking. Evaluating the linear absorption spectra will enable more direct comparison of the theoretical symmetry-breaking properties to experimental results and may provide insight into the source of the broadening of the experimental absorption peaks. These calculations may also be used to evaluate how the polymethine end groups and environment affect the conjugation length at which the symmetry breaks.

Further work is also needed to achieve a deeper understanding of the relationships between polymethine aggregate geometries and the resulting optical and NLO properties. Although current MD results show that polymethine-counterion interactions occur in a broad distribution of positions, the current analysis does not reveal the extent to which

polymethines symmetry-break in thin films. As the effective electric field of the counterion is highly non-uniform across the polymethine structure, it is important to understand the dependence of symmetry-breaking on the counterion size and position and the surrounding dielectric environment. Also, as the bulk structures include many polymethines and counterions in close proximity, evaluating the interaction of each polymethine with its full local environment could be used to provide routes to minimize bulk symmetry-breaking of polymethines. Likewise, analysis to date of polymethine-polymethine interactions was focused on minimizing aggregation. Further work is needed to understand how changes in the aggregate geometries affect the linear absorption spectra and NLO properties. A clear understanding of the relationships between polymethine and counterion structure, aggregate geometries, and optical and NLO properties would provide insight into whether controlled aggregation could be used to enhance the NLO response of polymethine-based materials. Similar MD studies could aid in evaluating the efficacy of other molecular design approaches to minimize or control polymethine aggregation, such as zwitterionic polymethines with covalently tethered counterions, complementarily-charged polymethine pairs, and polyelectrolyte polymethine systems. Such computational studies could provide an understanding of the polymethine properties not easily accessible via experimental means and aid in designing new polymethine-based materials for third-order nonlinear optical applications.